Numerical Analysis of a
Waterjet Propulsion System

Norbert Willem Herman Bulten

Numerical Analysis of a
Waterjet Propulsion System

PROEFSCHRIFT

ter verkrijging van de graad van doctor aan de
Technische Universiteit Eindhoven, op gezag van de
Rector Magnificus, prof.dr.ir. C.J. van Duijn, voor een
commissie aangewezen door het College voor
Promoties in het openbaar te verdedigen
op woendag 15 november 2006 om 16.00 uur

door

Norbert Willem Herman Bulten

geboren te Winterswijk

Dit proefschrift is goedgekeurd door de promotoren:

prof.dr.ir. J.J.H. Brouwers
en
prof.dr.ir. H.W.M. Hoeijmakers

Copromotor:
dr. B.P.M. van Esch

Table of contents

Chapter 1   Introduction

The desire to travel faster and further is probably as old as mankind itself. There has been an enormous development in the way people use to travel from one place to another. At first it was only over land, and later also over sea. And since about a century is it possible to travel through air as well.

Achievements in automotive and aerospace technology are widely recognized. But probably, most readers do not realize the substantial development in high speed ship transportation. At the end of the 20th century, fast ferry catamarans sailing at 50 knots (equivalent to about 90 km/h) were in commercial service all over the world. However, this type of vessel had entered the market less than two decades before.

The considerable development in the high speed craft can be partly contributed to the application of waterjet propulsion systems. Currently used stern mounted waterjets are based on principles as applied by Riva Calzoni in 1932 [1]. However, the first type of waterjet propulsion was invented already 300 years earlier, by David Ramseye [2]. He stated in 1630 in English Patent No. 50 that he was able '*to make Boates, Shippes and Barges to goe against Stronge Winde and Tyde*'. It is supposed that he had a waterjet in mind for the propulsion, since at that time there was a great interest in using steam to raise water and to operate fountains. In 1661, English patent no. 132 was granted to Thomas Toogood and James Hayes for their invention of '*Forceing Water by Bellowes [...] together with a particular way of Forceing water through the Bottome or Sides of Shipps belowe the Surface or Toppe of the Water, which may be of siguler Use and Ease in Navagacon*'. This concept was based on a waterjet without a doubt. However, they did not

manage to develop a working prototype. This invention and the subsequent development of the waterjet until 1980 is described in much more detail by Roy [3]. From 1980 onwards the use of waterjets in commercial applications really started to grow [4].

At the start of the 21th century the sizes of installed waterjets have increased to diameters of about 3 meter. This has led to installed powers of 25 MW per installation. Luxury high speed motor yachts have achieved ship speeds well above 65 knots, which is about 120 km/h [5].

1.1   Waterjet layout

A stern-mounted waterjet installation as used in commercial applications, can be divided into four components: the inlet, the pump, the nozzle and the steering device. Figure 1.1 shows a drawing of a typical waterjet installation, with the main components labelled.

1. inlet
2. pump
3. nozzle
4. steering device
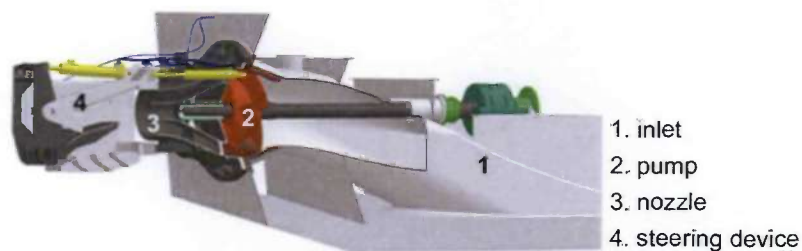
Figure 1.1   Three-dimensional view of a waterjet installation

The main component is the pump, which delivers the head to produce the jet at the nozzle exit. In general the stator bowl and the nozzle are integrated in one part. In the remainder of the thesis, the combination of the pump unit and the nozzle is regarded as the waterjet pump.

The ducting system upstream of the pump is called the inlet. The waterjet in figure 1.1 shows a flush mounted inlet duct. This is used, for example, in fast-ferries and high speed motor yachts. Kruppa *et al.* [6] have given an overview of the basic concepts of waterjet inlet ducting systems. Besides the flush mounted inlet, ram and scoop type inlets are mentioned. The latter two have an opening that is situated more or less perpendicular to the flow direction, whereas the flush mounted inlet opening is parallel to the flow. The ram and scoop intake will not be considered in this thesis.

Downstream of the nozzle there is a steering device, which can deflect the jet in order to create steering and reversing forces. There are also installations for the deflection of the jet possible, with only the reversing option. This can be useful for quick crash-stop manoeuvres. If the waterjet has no steering device at all, it is called a booster waterjet.

1.2 Relation of waterjet propulsion system to other turbo machinery

If the very early 17th century developments are neglected, waterjet propulsion is relatively new. For further development of the installation it may be useful to look at related engineering applications. Figure 1.2 shows a box with eight different types of apparatus. The three faces which are connected to the waterjet share a common property.

The front face is formed by four installations which are designed to produce thrust. This group contains, besides the waterjet, the ship propeller and the two main aeroplane propulsion systems. Any thrust production by the installations at the back face (mixed-flow pump, compressor, ventilator and mixer) is an undesirable side effect.

If history is reviewed an interesting parallel can be recognised. In aerospace the propeller has been replaced by the jet engine, which was necessary to reach higher speeds. Application of waterjets in marine industry shows a similar trend where the waterjet propelled vessels reach higher speeds.

Many relations which describe the principles of waterjet propulsion are directly derived from propeller theory, with the same nomenclature. This can lead to misunderstandings, if the same waterjet is described as a mixed-flow pump, with the accompanying pump nomenclature. For example, often Q is used for torque in propeller theory and for flow rate in pump theory.

The two side planes of the box show the difference in type of flow. The left side is formed by external flow machines and the right side by internal flow machines. Transmission of the forces in an external flow machine can only be done through the shaft. Internal flow machines can also transfer forces through the surrounding structure.

The top plane of the box shows four installations which operate in water, whereas the applications on the bottom plane operate in air. So here the fluid is the distinguishing factor. Cavitation is a typical problem for installations operating in water. Another important fluid property of water is its very low compressibility. Both phenomena can be important in the selection of numerical solution methods. Numerical methods used for the analysis of compressors and other flow machinery often require a certain amount of compressibility, what makes these methods less suitable for the analysis of a waterjet propulsion system.

The box model will be used to relate the occurring phenomena in a waterjet installation to known ones in other machines, like the ship propeller, the aeroplane jet engine and the mixed-flow pump.

A ship propeller seems to be the most logical connection to a waterjet for a description of the propulsion system. Typical parameters used in propeller
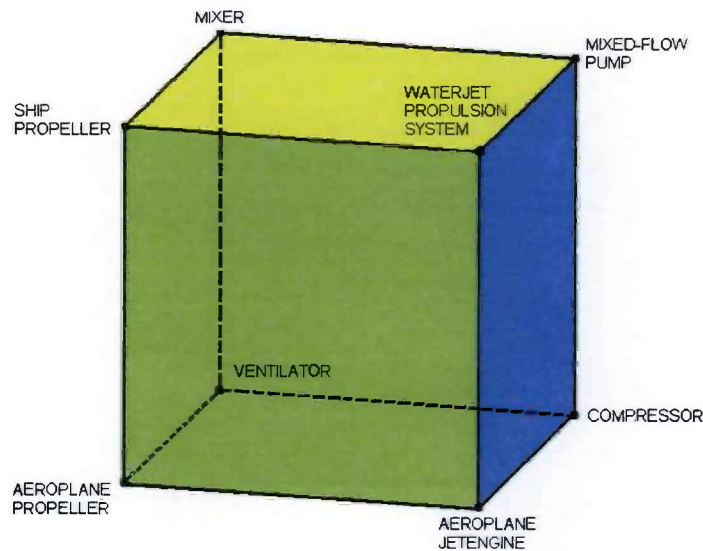
Figure 1.2   Box model of connections of waterjet to other types of turbomachinery

theory are the thrust loading coefficient and the cavitation number [7]. These parameters can be employed to describe the performance of a waterjet as well. Moreover the concept of wake fraction, which represents the difference between the free stream advance speed and actual inflow velocity, can be used to account for the effect of the hull boundary layer ingestion.

It is well-known that the inflow velocity distribution to the waterjet impeller is strongly non-uniform. This is similar to the wake field of a ship propeller. Due to this wake field the loading of a propeller blade fluctuates during a revolution. This results in fluctuations of the pressure distribution on the blades and in a radial force on the shaft. These phenomena will also be present in a waterjet. Therefore the choice of a propeller as a starting point for the analysis of a waterjet installation seems to be logical. However, there is a very important difference between a propeller and a waterjet installation. A propeller is an external flow machine whereas the waterjet installation is mainly an internal flow system. The thrust of a propeller will always be guided through the shaft into the ship. In a waterjet installation the forces can be transferred to the vessel via the shaft and via the ship structure. In fact it is possible to have a higher thrust acting on the shaft than the net thrust of the installation [8]. In that case a negative force will work on the transom stern and the inlet ducting.

Because the ship propeller operates as an external flow machine, the ship speed can be used as a governing parameter for the operating point. In non-dimensional notation it is called advance ratio (see for example [10], [10]):

$$J = \frac{v_{ship}}{nD} \tag{1.1}$$

where v_{ship} is the ship (or advance) speed, n the shaft speed and D the diameter of the propeller.

The working point of the waterjet installation is based on the volume flow rate Q through the system. In this system the pump head curve matches the system resistance curve, which is based on the required head to produce the jet velocity and the head to overcome the hydraulic losses. The influence of ship speed on the operating condition is small.

As a consequence, the available set of propeller equations cannot be used for a good description of the waterjet propulsion system.

The theory of aeroplane jet engines may provide the missing equations to describe the performance of a waterjet system. A turbojet engine is a thrust producing internal turbomachine, just like the waterjet. The turbojet engine can be divided into five major components: intake, compressor, combustion chamber, turbine and nozzle (see for example [11]). These components include the power generating part of the jet engine, i.e. the compressor is driven by the turbine. In a waterjet a separate diesel engine or gas turbine is needed to supply the required power to the shaft.

Net thrust of a turbojet engine is based on the change of momentum:

$$F = \dot{m}(v_{out} - v_{in}) \tag{1.2}$$

where $\dot{m}$ is the mass flow through the system, v_{out} the jet velocity leaving the engine and v_{in} the velocity of the air entering the intake, which is equal and opposite to the forward speed of the aircraft. Strictly spoken the mass flow in the system increases due to the addition of fuel, but this increase in mass flow is negligible. According to equation (1.2), the thrust of a waterjet system is directly related to the volume flow rate, since the flow is incompressible: $\dot{m} = \rho Q$.

The definition of the propulsive efficiency of a turbojet engine can be found in literature [11]:

$$\eta_p = \frac{F \cdot v_{in}}{P_{shaft}} = \frac{2}{1 + (v_{out}/v_{in})} \tag{1.3}$$

which is often denoted as Froude efficiency. The ratio between intake and nozzle velocity is called nozzle velocity ratio (NVR = v_{out}/v_{in}). At zero speed

the NVR becomes infinite, therefore the reciprocal value is used in literature for waterjets; this is known as jet velocity ratio μ [12].

Although the working principle of the aeroplane jet engine and the waterjet seem to be similar, it should be kept into mind that cavitation and non-uniform inflow, two important issues in waterjet propulsion, are not dealt with in jetengine research.

The third type of turbomachinery which may provide part of the basic theory to describe system performance is a mixed-flow pump. At first sight this is a bit strange, because normally the axial thrust in pump operation is not exploited. Nevertheless, the head curve of the pump and the system resistance curve provide sufficient information to determine the volume flow rate Q through the system. To get a first estimation of the thrust of the system, only the average velocity of the ingested flow and the dimension of the nozzle diameter have to be known.

1.3   Aim of the analysis

In this thesis a detailed analysis of a waterjet propulsion system is made. Results of Computational Fluid Dynamics (CFD) calculations are used to get an impression of the flow phenomena occurring in such systems and to quantify system parameters, such as flow rate, torque and thrust. With the application of a numerical method some flow features are easier to determine than in a model scale test. Typical complicating factors in the analysis of waterjets are the boundary layer ingestion and the non-uniform velocity distribution just upstream of the pump. Unfortunately, both the boundary layer ingestion as well as the non-uniformity of the velocity distribution are inevitable in commercial waterjet propulsion systems with a flush type of inlet. The major problem of the impeller inlet velocity distribution is the large variation of the velocity in circumferential direction. This will give rise to a blade loading, which varies strongly with time. This may lead to a decrease in system performance, like a reduced efficiency, a deterioration in cavitation behaviour and an increase of forces acting on the impeller. These phenomena will increase the noise and vibrations in the installation.

The aim of the analysis presented in this thesis is (i) to quantify the effects of the non-uniform inflow to the mixed-flow pump and the resulting non-stationary flow in the pump on the system performance and (ii) to quantify the forces on the complete waterjet installation in both axial and vertical direction. The currently used theory to determine system performance includes some assumptions about the influence of the pressure distribution on the streamtube of the ingested water. These assumptions will be reviewed to check their validity.

1.4   Outline of this thesis

In chapter 2 the conventional theory of waterjet propulsion systems will be discussed in detail. This will give insight in the governing parameters of the total propulsion system. Some connections will be made with standard propeller theory to show the similarities and the differences. Some of the underlying assumptions made will be discussed to enable assessment of these assumptions later on. The analysis also reveals the basic principles of waterjet selection which is suitable for most of the current applications.

Values for pump parameters in literature are based on uniform inflow. However, it is well-known that a waterjet impeller has to operate in a non-uniform inflow velocity field. The nature of the velocity distribution will be discussed in chapter 3. Results of measurements will be shown to give an impression of the level of non-uniformity. It is concluded that the typical non-uniform velocity distributions are inevitable in waterjet installations with flush mounted inlets, based on an analysis of the development of the non-uniformity in the duct upstream of the impeller.

Chapter 4 deals with the choice of a mathematical method to analyse the flow through the system. An evaluation of several methods, such as potential flow, Euler and RANS, will be presented. An important requirement is the capability to capture the effects of the non-uniform inflow to the pump.

The chosen method for the calculation of the flow through a waterjet inlet will be validated with available experimental data in chapter 5. In these calculations, the mass flow rate is prescribed as a boundary condition, since the pump is not included in the model. The results of the numerical analysis of the inlet will also be used to evaluate the shape of the streamtube upstream of the inlet duct. Determination of this streamtube enables a more detailed analysis of the momentum distribution of the ingested water.

Chapter 6 will deal with the numerical analysis of the non-stationary flow through the mixed-flow pump. Results of calculations are compared with model scale measurements of the pump performance. Transient calculations with both uniform and non-uniform velocity distributions will show the presence of fluctuating radial forces. These forces are strongly related to the level of non-uniformity in the flow.

Chapter 7 will show the results of the analysis of a complete full scale waterjet propulsion system. Overall performance indicators, like volume flow, thrust and power, will be analysed. Comparisons are made with performance prediction software of Wärtsilä Propulsion Netherlands (WPNL). A more detailed analysis of the streamtube will reveal some new insights into the forces acting on the installation in vertical direction.

Finally, the conclusions of the present research will be presented in chapter 8.

1.5 Nomenclature

D	propeller diameter	m
F	thrust	N
J	advance ratio of propeller ($= v_{ship}/nD$)	-
$\dot{m}$	mass flow rate	kg/s
n	rotational speed	1/s
NVR	nozzle velocity ratio ($NVR = v_{out}/v_{in}$)	-
P_{shaft}	shaft power	W
Q	volume flow rate	m^3/s
v_{ship}	advance velocity of propeller	m/s
v_{in}	advance velocity of jet-engine	m/s
v_{out}	jet velocity of jet-engine	m/s

Greek symbols

η_p	propulsive efficiency	-
μ	jet velocity ratio ($= 1 / NVR$)	-
ρ	fluid density	kg/m^3

1.6 References

[1] Voulon, S., 'Waterjets and Propellers, Propulsors for the future', Proceedings SATEC'96 conference, Genoa, Italy, 1995

[2] Ramseye, David, 'Manufacture of Saltpetre, Raising Water, Propelling Vessels, &c.', English patent no. 50, 1630

[3] Roy, S.M., 'The evolution of the modern waterjet marine propulsion unit', Proceedings RINA Waterjet Propulsion conference, London, 1994

[4] Warren, N.F., & Sims, N.,'Waterjet propulsion, a shipbuilder's view', Proceedings RINA Waterjet Propulsion conference, London, 1994

[5] Bulten, N. & Verbeek, R.,'Design of optimal inlet duct geometry based on operational profile', Proceedings FAST2003 conference Vol I, session A2, pp 35-40, Ischia, Italy, 2003

[6] Kruppa, C., Brandt, H., Östergaard, C., 'Wasserstrahlantriebe für Hochgeschwindigkeitsfahrzeuge', Jahrbuch der STG 62, Band 1968, Nov., pp. 228-258, 1968

[7] Terwisga, T.J.C. van,'Waterjet hull interaction', PhD thesis, Delft, 1996

[8] Verbeek, R.,'Waterjet forces and transom flange design', RINA waterjet propulsion conference, London, 1994

[9] Newman, J.N., 'Marine hydrodynamics', MIT press, 1977

[10] Lewis, E.V., 'Principles of naval architecture', Volume II, Society of Naval Architects and Marine Engineers, Jersey City, 1998

[11] Cohen, H., Rogers, G.F.C., Saravanamuttoo, H.I.H., 'Gas turbine theory', Longman Group, London, 1972

[12] Verbeek, R.,'Application of waterjets in high-speed craft', in Hydrodynamics: Computations, Model Tests and Reality, H.J.J. van den Boom (Editor) Elsevier Science Publication, 1992

Chapter 2 Waterjet propulsion theory

In this chapter the basic principles of waterjet propulsion will be discussed. The equations of the waterjet theory will be based on standard nomenclature used in the description of pump performance. Where possible, equivalent nomenclature of commonly used propeller theory will be mentioned as a reference.

In the first section some specific velocities, as used in waterjet theory, will be defined. These definitions form the basis for the remainder of the chapter. In the second section, the generally applied standard parameters are defined, which are used to describe the overall pump performance.

In the commonly used waterjet propulsion theory, equations for the derivation of thrust of a waterjet propulsion system are based on open propeller theory. The transition from open propellers to waterjets will be reviewed in detail, in order to reveal possible deficiencies in the waterjet theory.

The equations for the waterjet thrust can be coupled to the required pump head and flow rate. This will be discussed in section 2.4. It will be shown that a certain thrust can be achieved with different combinations of flow rate and pump head. Determination of the optimal combination of flow rate and pump head is obtained with the aid of the overall propulsive efficiency. This will result in the design operating point of the pump in the waterjet installation.

In some conditions, the optimal pump operating point can not be reached due to severe cavitation in the pump. This limitation in the optimization process will be discussed in section 2.5.1.

In the selection of a waterjet installation for ship propulsion the weight of the installation is an important issue. To minimize the weight of the system, the size of the waterjets is selected as small as possible. The shaft speed of the pump is then maximised. It will be shown that for a given available power the minimum required pump size depends on the ship speed. The available power is governed by the installed diesel engine or gasturbine. This dictates the selection procedure to a large extent.

2.1 Characteristic velocities in a waterjet system

In the equations for pump performance and thrust, use is made of some specific velocities. Four main velocities are distinguished and will be used throughout this thesis:

1. ship speed (v_{ship})
2. mass averaged ingested velocity at duct inlet (v_{in})
3. averaged axial inflow velocity at the pump entrance (v_{pump})
4. averaged outlet velocity at the nozzle (v_{out})

Figure 2.1 shows a sketch of a waterjet installation with the four velocities indicated. A non-uniform velocity distribution is sketched to indicate the development of the boundary layer along the hull surface, upstream of the inlet. This figure is also used to give an impression of the dividing streamline. By definition there will be no mass flow across this line. In three dimensions, this line is extended to a dividing streamtube. The curved part of the inlet, where the streamline ends, is denoted as inlet lip or cutwater.
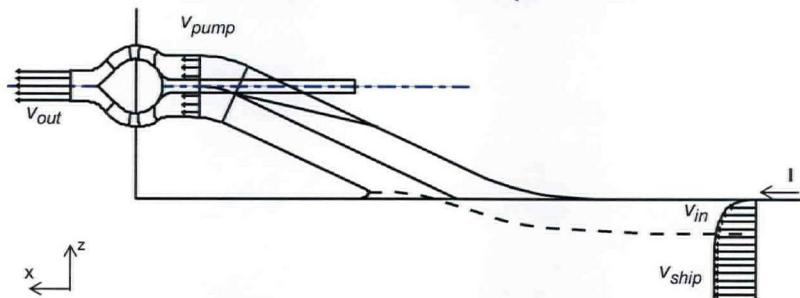
Figure 2.1   Characteristic velocities in waterjet propulsion system

The inlet velocity is determined at a cross-flow plane just upstream of the waterjet inlet, where the influence of the waterjet is not yet noticeable. The ingested velocity distribution is mass-averaged over the cross-sectional shape of the streamtube to find the actual inlet velocity v_{in}:

$$v_{in} = \frac{1}{Q} \int_A v(z) v_n dA \qquad (2.1)$$

where $v(z)$ is the velocity distribution in the boundary layer.

The four velocities are related by three parameters; wake fraction, inlet velocity ratio and jet velocity ratio. These three parameters are discussed in detail in this section.

2.1.1   Wake fraction

The water that is ingested into the waterjet inlet channel partly originates from the hull's boundary layer. The mass averaged velocity of the ingested water (v_{in}) is lower than the ship speed due to this boundary layer. The velocity deficit is expressed as the momentum wake fraction (w), which is defined as:

$$w = 1 - \frac{v_{in}}{v_{ship}}$$

(2.2)

Calculation of the wake fraction is rather complex, since the cross-sectional shape of the streamtube is not known a priori. Experiments have revealed that the cross-section of the streamtube has a semi-elliptical shape under the hull [1]. This is often simplified by a rectangular box with a width of 1.3 times the pump diameter. Some comparisons have been made with experimental results [2], [3] and it is concluded that the resulting value for the wake fraction can be determined within acceptable limits, if the rectangular box approximation is used.

For a given volume flow rate through the waterjet the height of the box can be calculated once the velocity distribution in the boundary layer is known. Standard theory for a flat plate boundary layer, as described in several textbooks ([4], [5]) can be used to get a first indication of the velocity distribution. It is convenient to use a power law velocity profile for the boundary layer velocity distribution:

$$\frac{v}{U_\infty} = \left(\frac{z}{\delta}\right)^{\frac{1}{n}}$$

(2.3)

where v denotes the local velocity in the boundary layer at a distance z normal to the wall, U_∞ the undisturbed velocity, δ the local boundary layer thickness and n the power law index.

Besides the thickness of the boundary layer δ there are also derived quantities like the displacement thickness δ_1 and momentum thickness δ_2 of the boundary layer.

The momentum thickness can be related to the wall friction coefficient $c_f(l)$ for a flat plate:

$$c_f(l) \equiv \frac{\tau_w}{\frac{1}{2}\rho U_\infty^2} = 2\frac{d\delta_2}{dl} \tag{2.4}$$

where l is the wetted length. This relation gives the frictional drag of the flat plate in terms of the development of the boundary layer.

Substitution of the power law velocity distribution in the definitions of the boundary displacement thickness δ_1, the momentum thickness δ_2 and the energy thickness δ_3 results in a set of the following relations:

$$\delta_1 = \frac{\delta}{n+1} \tag{2.5}$$

$$\delta_2 = \frac{\delta n}{(n+1)(n+2)} \tag{2.6}$$

$$\delta_3 = \frac{2\delta n}{(n+1)(n+3)} \tag{2.7}$$

Combination of equations (2.4) and (2.6) gives an expression for the friction coefficient $c_f(l)$ as function of the boundary layer thickness $\delta(l)$ and the power law exponent n. For turbulent flow a value of $n = 7$ is often used. With aid of the analysis of developed turbulent pipe flow, an expression for the flat plate boundary layer thickness is derived:

$$\delta|_{n=7} = 0.370 \cdot l \cdot Re_l^{-1/5} \tag{2.8}$$

where Re_l is the Reynolds number based on the wetted length. The wall friction coefficient for n=7 becomes:

$$c_f(l) = 0.0576 \cdot Re_l^{-1/5} \tag{2.9}$$

Comparison with experimental data shows good agreement for Reynolds numbers between 5×10^5 and 10^7 (see [4]).

In general, full scale waterjet installations operate at Reynolds numbers of about 10^9, which is 2 orders of magnitude larger. The wall friction coefficient for a flat plate cannot be based on equation (2.9) at these high Reynolds numbers. Several logaritmic equations for the flat plate wall friction coefficient are defined for high Reynolds numbers. A typical example is the ITTC'57

friction line, which is commonly used to extrapolate the viscous resistance component of a model scale ship to full scale dimensions.

The logaritmic friction line gives the wall friction coefficient as function of Reynolds number. Based on equations (2.4) and (2.6), there is a relation between friction coefficient $c_f(l)$, boundary layer thickness $\delta(l)$ and power law exponent n. The actual power law exponent n is determined from velocity profile measurements by Wieghart. Results of measurements at different Reynolds numbers are presented in Schlichting [4]. For a certain Reynolds number, the corresponding boundary layer thickness can be calculated once the wall friction coefficient $c_f(l)$ and the power law exponent n are established.

Full scale measurements of the hull boundary layer velocity distribution are presented by Svensson [7]. Velocity profiles are measured on two different vessels and at different ship speeds. This results in a large variation of Reynolds numbers. A reasonable fit of a power law profile with $n = 9$ and the measured values is found. The equation for the boundary layer thickness, as given in equation (2.8), is modified for $n = 9$:

$$\delta|_{n=9} = 0.270 \cdot l \cdot Re_l^{-1/6}$$ (2.10)

It can be noticed that both the constant as well as the power of the Reynolds number have to be changed when the value of n is changed. This is in accordance with measurements of Wieghardt (see [4]). Adjustment of these values should result in the right boundary layer thickness and in an accurate prediction of the velocity profile and the wall friction. For Reynolds numbers of order 10^9 the power law exponent becomes 10 to 11.

With known boundary layer thickness and volume flow through the pump, the average incoming velocity and thus the wake fraction can be calculated. A typical value for the wake fraction w is 0.10 to 0.14 for a fast ferry.

The accuracy of the rectangular box approximation will be reviewed in chapter 5 when CFD calculations of the flow through the waterjet inlet duct are discussed. With the numerical method it is possible to visualize the actual shape of the streamtube and determine the mass-averaged velocity by numerical integration. This numerical method is based on the computed shape of the streamtube, whereas the determination of the wake fraction in experiments is based on an approximated shape of the streamtube. Consequently, the wake fraction obtained from the numerical results is more accurate than the one obtained from experimental data.

2.1.2 Inlet velocity ratio

The averaged axial inflow velocity of the pump is denoted by v_{pump}. This velocity can be written as:

$$v_{pump} = \frac{Q}{\frac{\pi}{4}D_{inlet}^2}$$

(2.11)

where Q is the volume flow through the pump and D_{inlet} the diameter at the suction side of the pump. This velocity is an important parameter to describe the flow phenomena in the inlet, where the speed is changed from the ship speed to the pump velocity. The pump velocity is related to the ship speed through the Inlet Velocity Ratio (IVR):

$$IVR = \frac{v_{ship}}{v_{pump}}$$

(2.12)

At normal operating condition, IVR will be around 1.3 to 1.8. The reciprocal of equation (2.12) is used in literature as well ([2], [8]) and used by the ITTC; this results in values of this quantity, at operating conditions below 1 and a value of infinite for zero ship speed. Use of the definition in equation (2.12) is preferred since the operating range is bounded between 0 and about 2.5.

IVR is used to denote the flow conditions in the waterjet inlet duct. At relatively low ship speed, e.g. during manoeuvring in harbour, IVR will be smaller than 1. This means that the flow is accelerated upon entering the inlet duct. In this condition the stagnation point of the dividing streamline is located at the hull side of the inlet lip (or cutwater). This might lead to cavitation and/ or separation in the inlet at the upper side of the lip. Figure 2.2 shows a sketch of the flow phenomena at low IVR condition.

If the vessel sails at design speed, the inlet flow phenomena are quite different. As mentioned, the design IVR will be around 1.3 to 1.8. IVR values

Increased risk for
cavitation and/or separation
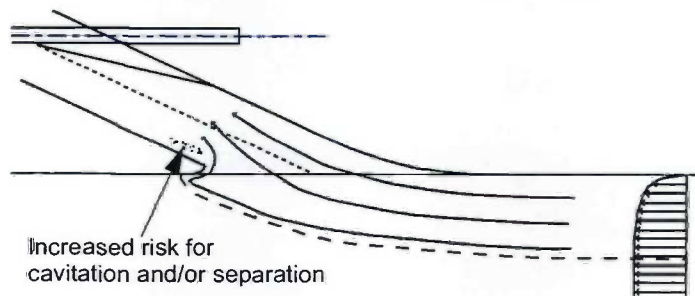
Figure 2.2   Flow phenomena at low IVR

Increased risk of separation

Increased risk of cavitation
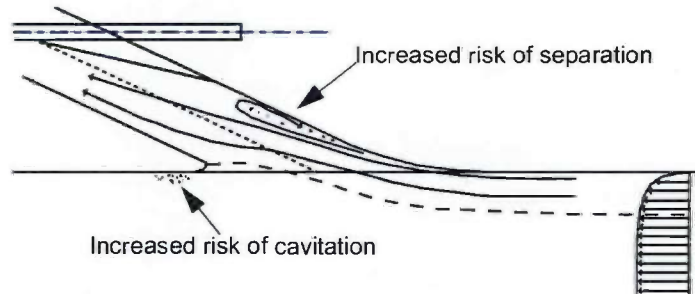
Figure 2.3   Flow phenomena at high IVR

of more than 2.0 are known for high speed motor yachts (>60 knots). This implies a significant deceleration of the flow in the inlet. In this condition the stagnation point is located at the inlet side of the cutwater. The critical location for cavitation is located at the hull side of the lip for this condition. The deceleration of the flow in the inlet duct leads to an adverse pressure gradient in the inlet. If this pressure gradient becomes too large, flow separation is likely to occur at the top side of the inlet. The possible flow phenomena at high IVR are sketched in figure 2.3.

Whether or not cavitation or separation really occurs in a practical situation, strongly depends on the actual geometry of the inlet duct. With a good inlet design cavitation and separation free operation is possible up to about 44 knots [9], which is a commonly used design speed for fast ferries.

It should be kept in mind, that an inlet has to be designed to cope with the low IVR and the design IVR condition, because each vessel has to start from zero ship speed.

2.1.3   Jet velocity ratio

The velocity v_{out} at the outlet of the waterjet nozzle, is related to the volume flow through the pump and the diameter of the nozzle as:

$$v_{out} = \frac{Q}{\frac{\pi}{4}D^2_{nozzle}}$$

(2.13)

The outlet velocity is related to the incoming velocity by the jet velocity ratio μ according to [10]:

$$\mu = \frac{v_{in}}{v_{out}}$$

(2.14)

The importance of the parameter μ will be shown in section 2.5, where the overall propulsive efficiency of the waterjet system is derived. It will be shown that typical values are in the range of 0.5 to 0.7.

2.1.4 Summary

In this section four velocities are introduced; v_{ship}, v_{in}, v_{pump} and v_{out}. The relations between these velocities are defined by three ratios: wake fraction w, inlet velocity ratio IVR and nozzle velocity ratio μ. The theory of waterjet propulsion will be based on these velocities and ratios.

2.2 General pump theory

In this section a short overview of the standard pump theory is given in order to introduce a set of parameters to describe the pump performance. This theory can be found in many textbooks about centrifugal pumps, see for example [11], [12].

2.2.1 Dimensionless performance parameters

Performance of a pump can be expressed in terms of a set of non-dimensional parameters. The performance is expressed in terms of flow rate, head and cavitation behaviour. In dimensionless form, the flow rate through the pump is given as the flow coefficient φ:

$$\varphi \equiv \frac{Q}{\Omega D^3} \tag{2.15}$$

where Q is the flow rate in m³/s, Ω the speed of the impeller in rad/s and D the impeller diameter in m. The head coefficient ψ of a pump is defined as:

$$\psi \equiv \frac{gH}{(\Omega D)^2} \tag{2.16}$$

where H is the head in m. It can be shown that geometrically similar pumps have equal values for flow and head coefficient. This forms the basis of the so-called similarity method. If the performance of a pump for a certain size and shaft speed is known, equations (2.15) and (2.16) can be used to predict the performance for different sizes and shaft speeds. Elimination of the diameter D from equations (2.15) and (2.16) results in:

$$1 = \frac{\Omega Q^{1/2}}{(gH)^{3/4}} \cdot \frac{\psi^{3/4}}{\varphi^{1/2}} \tag{2.17}$$

which leads to the definition of the specific speed of:

$$n_\omega \equiv \frac{\Omega\sqrt{Q}}{(g \cdot H)^{3/4}}$$
(2.18)

where Ω is the speed of the impeller in rad/s, Q the flow rate in m^3/s and H the head in m. It is also found that the similarity method implies that geometrically similar pumps have equal values of specific speed:

$$n_\omega = \frac{\varphi^{1/2}}{\psi^{3/4}}$$
(2.19)

The value of the specific speed of a specific pump gives a good indication of its type: typical axial flow pumps have a specific speed above 2.4, whereas radial flow pumps have low values of the specific speed (typically below 1.0). Mixed-flow pumps have intermediate values for the specific speed.

Pump efficiency η_{pump} is defined as the ratio between the hydraulic power P_{hydr} which is the product of flow rate and pressure rise, and the required shaft power P_{shaft}.

$$\eta_{pump} = \frac{P_{hydr}}{P_{shaft}} = \frac{\rho g H Q}{\Omega T_q}$$
(2.20)

where T_q is the shaft torque. The required shaft power can be expressed in a non-dimensional specific power P^*:

$$P^* = \frac{P_{shaft}}{\rho \Omega^3 D^5}$$
(2.21)

The specific power is related to the flow coefficient, head coefficient and pump efficiency. Combination of equations (2.15), (2.16) and (2.20) yields:

$$P^* = \frac{\varphi \psi}{\eta_{pump}}$$
(2.22)

Strictly speaking, similarity of performance is only valid in cases of both geometrically and dynamically similar internal flows. In this analysis viscosity is not taken into account. Since hydraulic losses do scale differently, additional empirical relations are used to predict the effect of these losses on pump efficiency and specific power.

2.2.2   Pump geometry parameters

It is shown in the preceding section, that the specific speed is found from the expressions for flow coefficient and the head coefficient, when the diameter is eliminated. In a similar way, the specific diameter δ is found, if the rotational speed Ω is eliminated:

$$1 = \frac{gHD^4}{Q^2} \cdot \frac{\varphi^2}{\psi} \tag{2.23}$$

so that:

$$\delta \equiv D \cdot \frac{(gH)^{1/4}}{\sqrt{Q}} \tag{2.24}$$

and:

$$\delta = \frac{\psi^{1/4}}{\varphi^{1/2}} \tag{2.25}$$

The specific speed and specific diameter are based on the same two parameters, namely φ and ψ. The relation between the two is represented in the so called Cordier-diagram [14], which is based on experience from actual pumps. Waterjet pump designs may deviate from this empirical rule for conventional pumps due to the difference in functionality as outlined in chapter 1.

The basic geometry of the impeller of conventional centrifugal pumps is strongly related to the specific speed of a pump, however. The large similarities in pump geometry lead to comparable efficiencies for different pumps with the same specific speed. The statistically attainable optimal pump efficiency can be derived from several published prediction formulas, based on measured performances. An example of such empirical formula is given in [15]:

$$\eta_{pump} = 0.95 - \frac{0.05}{\sqrt[3]{Q/Q_{ref}}} - 0.125[log(n_\omega)]^2 \tag{2.26}$$

where Q_{ref} is set equal to 1 m^3/s in order to maintain the non-dimensional representation. Figure 2.4 shows the expected maximum pump efficiency for three flow rates. The highest efficiency is found at a specific speed of 1.0. Decrease in efficiency is rather slow when the specific speed is increased to values above 1.0. In general, waterjet pumps have a specific speed around 2.0-3.0.
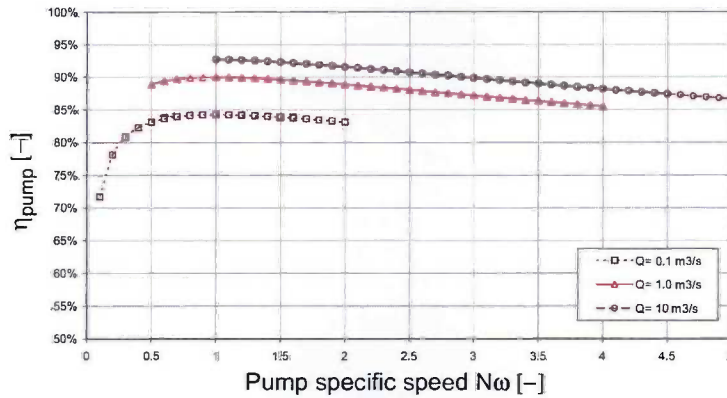
Figure 2.4   Maximum pump efficiency as function of specific speed, based on equation (2.26).

Achievable pump efficiencies around 90% for large pumps seem to be a reasonable estimate. This value will be used in the remainder of this chapter for estimates of the overall waterjet efficiency.

2.2.3   Cavitation parameters

For cavitation free operation the pump requires a certain available pressure at the inlet, or suction side. This is denoted with the inception net positive suction head (*NPSH$_i$*), which is a pressure expressed in meters water column. In general, pump operation is still possible beyond the cavitation inception level, i.e. for lower NPSH levels. Therefore the criterion for the inlet suction head is based on a certain loss of pump performance (for example 1 or 3% head loss or a certain percentage of pump efficiency decrease, see [16]). Based on the choice for the admissible head loss, a required NPSH is defined.

The required net positive suction head (*NPSH$_R$*) can be made non-dimensional in a similar way as the head to form the suction coefficient κ:

$$\kappa = \frac{gNPSH_R}{(\Omega D)^2} \tag{2.27}$$

Another, well-known method to present the NPSH in dimensionless representation is the Thoma number, defined as:

$$\sigma = \frac{NPSH_R}{H} \tag{2.28}$$

The non-dimensional parameters are related by the head coefficient.

The required NPSH can also be related to the flow rate and the rotational speed of the impeller, similar to the pump specific speed. This gives the suction specific speed of the pump $n_{\omega s}$, defined as:

$$n_{\omega s} = \frac{\Omega \sqrt{Q}}{(g \cdot NPSH_R)^{3/4}} \qquad (2.29)$$

The suction specific speed of a pump is more or less constant for all pump types. Values of about 4.0 are common in commercial pumps [14-17]. In order to create some extra margin to accommodate cavitation, a design value of 3.5 for a waterjet impeller is adopted.

2.2.4 Correlation with propeller performance parameters

The flow coefficient φ of a pump can be related to the propeller advance ratio J (as given in eqn. (1.1)) with substitution of equations (2.11) and (2.12):

$$\varphi = \frac{\pi v_{pump}}{4\Omega D} = \frac{J}{8IVR} \qquad (2.30)$$

This relation shows the fundamental difference between an open propeller and a waterjet installation, where in the waterjet IVR is introduced as an additional parameter. This parameter is needed because of the principle of internal flow of the pump compared to the external flow of the propeller.

In a similar way, the non-dimensional head can be related to the thrust coefficient of an open propeller. For a propeller the thrust coefficient is defined as [18]:

$$K_T = \frac{T}{\rho n^2 D^4} \qquad (2.31)$$

The head H of a pump is related to the total pressure increase generated by the impeller according to:

$$\Delta p_{tot} = \rho g H \qquad (2.32)$$

In actuator disk theory the production of thrust of an open propeller equals the product of the pressure rise and the cross-sectional area of the propeller:

$$T = \Delta p \cdot A_{prop} \qquad (2.33)$$

It is assumed that the static pressure rise is equal to the total pressure rise, due to the infinitesimal thickness of the actuator disk. This results in a relation

between the head coefficient ψ of a pump and the thrust coefficient K_T of a propeller:

$$\psi = \frac{(\Delta p)/\rho}{4\pi^2 n^2 D^2} = \frac{K_T}{\pi^3} \tag{2.34}$$

It is concluded that the Q-H curves of a pump are equivalent to the J-K_T curves of an open propeller. The main difference is caused by the used inflow velocity.

2.3   Thrust

2.3.1   General thrust equation

The purpose of a propulsion installation is to produce thrust to propel a vessel. Water is accelerated in the installation, which results in a reaction force on the ship structure. The thrust can be derived from the momentum balance for an incompressible fluid [5]:

$$\underline{F} = \underline{F}_s + \underline{F}_b = \frac{\partial}{\partial t} \int_V \underline{v} \rho \, dV + \int_A \underline{v} \rho \underline{v} \cdot d\underline{A} \tag{2.35}$$

The momentum balance states that the sum of all surface forces F_s and all body forces F_b acting on the spatially fixed control volume V equals the rate of change of momentum in the control volume with surface A. The surface force is defined as:

$$\underline{F}_s = \int_A (-p\underline{I} + \underline{\sigma}) \cdot d\underline{A} \tag{2.36}$$

where p is the static pressure, $\underline{I}$ the unit tensor and $\underline{\sigma}$ the viscous stress tensor.

In the remainder of this section the steady flow situation will be analysed. As a consequence, the first term on the right hand side of equation (2.35) vanishes. Moreover, the body forces, like gravity, acting on the fluid will be neglected.

In the following subsections the momentum balance will be derived for both an open propeller and a waterjet.

2.3.2 Open propeller thrust

An expression for the thrust of an open propeller is determined with equation (2.35) [6]. The propeller is treated as an actuator disk, which is a singularity modelled by a body force acting over an infinitesimal thin disk. The control volume consists of the streamtube of fluid which passes through the propeller plane area. Figure 2.5 shows a sketch of the control volume of an open propeller with the nomenclature of the velocities.

Evaluation of the momentum balance is split in two parts; the contribution of the momentum fluxes and the contribution of the surface forces. The contributions of the momentum fluxes in x-direction result in a net momentum flux component in x-direction of:

$$\phi_{mx} = \rho v_{out}^2 A_{out} - \rho v_{in}^2 A_{in} \tag{2.37}$$

This can be rewritten, with aid of the continuity condition, as:

$$\phi_{mx} = \rho v_{prop} A_{prop}(v_{out} - v_{in}) \tag{2.38}$$

The contributions of the surface forces in x-direction are defined as:

$$F_x = -T_{prop} - \int_{A_{in}} (p - p_\infty)dA + \int_{A_{out}} (p - p_\infty)dA + \int_{A_{tube}} (p - p_\infty)\underline{x} \cdot d\underline{A} \tag{2.39}$$

It is assumed that the pressure at the inlet (far upstream) and at the outlet (far downstream) is equal to the ambient pressure p_∞. Moreover, the contribution of the viscous forces is neglected on the inlet and outlet area as well as on
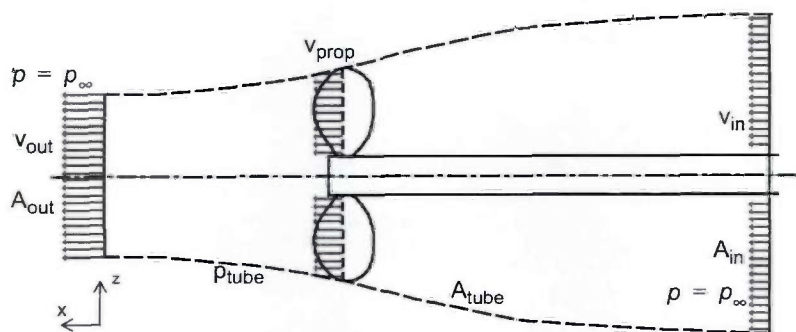
Figure 2.5   *Control volume for the momentum balance applied to an propeller within a streamtube*

the streamtube surface. Combination of equations (2.38) and (2.39) gives the final thrust equation for an open propeller, based on the momentum balance:

$$T_{prop} = \rho A_{prop} v_{prop}(v_{out} - v_{in}) - \int_{A_{tube}} (p - p_\infty) \underline{x} \cdot d\underline{A} \qquad (2.40)$$

where A_{prop} is the cross-sectional area of the propeller plane, $\underline{x}$ the unit vector in x-direction and A_{tube} the streamtube surface. The contribution of the pressure acting on the streamtube to the thrust vanishes, based on the paradox of d'Alembert, if the streamlines are aligned in x-direction far upstream and downstream.

If Bernoulli's theorem is applied along the streamlines in the part of the control volume upstream and downstream of the propeller, a second relation for the propeller thrust is found:

$$T_{prop} = \Delta p \cdot A_{prop} = \rho A_{prop} \cdot \frac{1}{2}(v_{out}^2 - v_{in}^2) \qquad (2.41)$$

Combination of the momentum balance and Bernoulli's law, leads to a simple relation between the inlet and outlet velocity and the volume flow through the propeller disk (see [18]):

$$v_{prop} = \frac{1}{2}(v_{in} + v_{out}) = v_{in} + v_{ind} \qquad (2.42)$$

It can be seen that the velocity through the disk is the average of the upstream and downstream velocities. The difference between the velocity through the disk and the incoming velocity is called the induced velocity v_{ind}.

Thrust loading coefficient

Loading of an open propeller is often expressed by the propeller loading coefficient, defined as [18]:

$$C_{Tprop} = \frac{T_{prop}}{\frac{1}{2}\rho v_{ship}^2 A_{prop}} \qquad (2.43)$$

where A_{prop} is the cross-sectional area of the propeller disk, based on the propeller diameter. The propeller loading coefficient can be expressed in terms of the ratios as defined in section 2.1. Substitution of equation (2.41), with the inflow velocity equal to the ship speed, i.e. $v_{in} = v_{ship}$, yields:

$$C_{Tprop} = \frac{\frac{1}{2}\rho(v_{out}^2 - v_{in}^2)A_{prop}}{\frac{1}{2}\rho v_{in}^2 A_{prop}} = \left(\frac{v_{out}}{v_{in}}\right)^2 - 1 = \frac{1 - \mu^2}{\mu^2} \qquad (2.44)$$

With $\mu < 1$ the propeller loading coefficient is thus directly related to the jet velocity ratio.

The jet velocity ratio can be related to the IVR, if equation (2.42) is substituted into equation (2.12):

$$IVR = \frac{v_{in}}{v_{prop}} = \frac{2v_{in}}{v_{in} + v_{out}} = \frac{2\mu}{\mu + 1} \qquad (2.45a)$$

It can be seen that open propellers always operate at IVR values below 1. After rearranging this equation, it is shown that the IVR is equal to Froude efficiency as given in equation (1.3):

$$IVR = \frac{2}{1 + \frac{1}{\mu}} = \frac{2}{1 + (v_{out}/v_{in})} = \eta_p \qquad (2.45b)$$

Although the term IVR is not used in the theory for open propellers, it is already present as the Froude efficiency.

2.3.3   Waterjet thrust

For the determination of the thrust of a waterjet installation in general the same approach as for the open propeller is used. The control volume will be bounded by the streamtube surface on one side and the solid wall on the other side. It is assumed that the inlet and exit planes are perpendicular to the x-direction and the hull is parallel to the x-axis. Figure 2.6 shows the control volume and the contributing terms to the momentum balance. The forces acting on the waterjet structure, which are included in this control volume, are denoted as $T_{wj,tube}$.

It is noted that the control volume based on the streamtube of the ingested water does not take into account the part of the waterjet inlet structure at the hull side near the cutwater lip, which is excluded from the streamtube control volume. The thrust or drag on that part of the waterjet structure will be denoted will $T_{wj,hull}$. At high IVR conditions a significant part of the cutwater geometry belongs to the excluded cutwater region. The subdivision of the complete waterjet inlet structure into the part, which is included in the streamtube approach, and the part which is excluded is shown in figure 2.7.
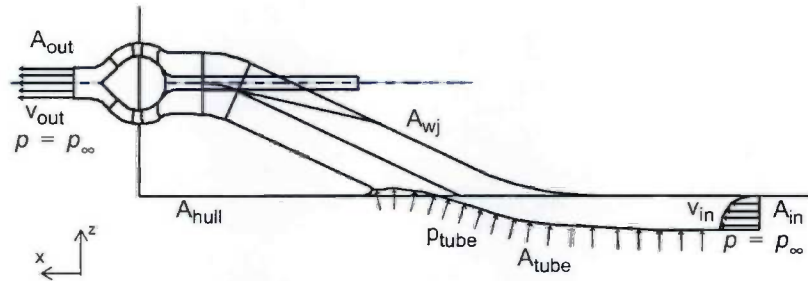
Figure 2.6   *Control volume for a momentum balance on the streamtube of*
the ingested water of a waterjet installation
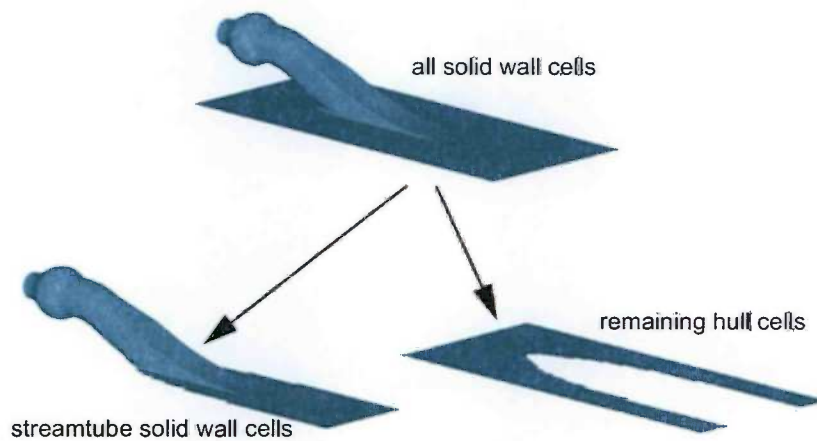
Figure 2.7   *Subdivision of all solid wall cells of the waterjet installation into*
group belonging to streamtube control volume (left) and group
of remaining cells on hull (right)

The total thrust $T_{wj,all}$ of a waterjet is therefore:

$$T_{wj,all} = T_{wj,tube} + T_{wj,hull}$$

(2.46)

Application of the momentum balance for a waterjet learns that there are two
momentum flux terms that contribute to the force in x-direction; these are the
fluxes at the nozzle exit surface A_{out} and at the plane A_{in} upstream of the
inlet:

$$\phi_{mx} = \rho v_{out}^2 A_{out} - \rho v_{in}^2 A_{in} \tag{2.47}$$

where v_{in} is the mass averaged inflow velocity. With aid of the continuity condition, this becomes:

$$\phi_{mx} = \rho Q(v_{out} - v_{in}) \tag{2.48}$$

where Q is the flow rate through the waterjet installation. The contributions of the surface forces in x-direction are defined as:

$$F_x = -T_{wj,tube} - \int_{A_{in}} (p - p_\infty) dA + \int_{A_{out}} (p - p_\infty) dA + \int_{A_{tube}} (p - p_\infty)\underline{x} \cdot d\underline{A} \tag{2.49}$$

Similar to the open propeller, it is assumed that volumetric forces and viscous forces can be neglected, while the pressure levels at the inlet (far upstream) and at the outlet (far downstream) are equal to the ambient pressure p_∞.

Effect of the viscous forces is neglected also on these two planes, though there is a non-uniform velocity distribution present at the inlet plane A_{in}. Contribution of this shear stress force is assumed to be negligible. With equations (2.48) and (2.49) can be combined to get the expression for the waterjet thrust in x-direction based on the streamtube momentum balance:

$$T_{wj,tube} = \rho Q(v_{out} - v_{in}) - \int_{A_{tube}} (p - p_\infty)\underline{x} \cdot d\underline{A} \tag{2.50}$$

The contribution of the streamtube pressure can not be quantified analytically, since the shape of the streamtube and the pressure distribution are unknown. Even with numerical methods it is a very complex task to determine this value, due to the three-dimensional shape of the streamtube surface and the dependency of the shape on IVR. In chapter 7 the contribution of the streamtube pressure term will be reviewed in more detail.

The thrust of the complete waterjet installation is found, when equation (2.50) is substituted in equation (2.46), which yields:

$$T_{wj,all} = \rho Q(v_{out} - v_{in}) - \int_{A_{tube}} p\underline{x} \cdot d\underline{A} + T_{wj,hull} \tag{2.51}$$

The last two terms on the right-hand-side are assumed to be small compared to the first term, and often neglected in waterjet propulsion literature. The

influence of this simplification will be addressed in more detail in chapter 7. The resulting simplified thrust equation for a waterjet becomes [10]:

$$T_{wj} = \rho Q(v_{out} - v_{in}) = \frac{\rho Q^2}{A_{nozzle}}(1-\mu) \tag{2.52}$$

Despite neglecting the streamtube and hull surface forces, this simplified equation can be used to explain the main theory on waterjet propulsion. This equation shows the three main parameters of a waterjet propulsion system: the volume flow rate Q through the system, the nozzle exit area A_{nozzle} and the jet velocity ratio μ.

Thrust loading coefficients

The thrust loading coefficient of a waterjet installation can be based on the nozzle outlet area or the pump inlet area. The thrust loading coefficient based on nozzle exit area is discussed in [13]. With the nozzle area as reference area, the relation between jet velocity ratio and the thrust loading coefficient becomes:

$$C_{Tnozzle} = \frac{T}{\frac{1}{2}\rho v_{ship}^2 A_{nozzle}} = \frac{2(1-\mu)(1-w)^2}{\mu^2} \tag{2.53}$$

where w is the wake fraction according to equation (2.2). The wake fraction becomes zero, when the inflow velocity is equal to the ship speed, i.e. $v_{in}=v_{ship}$. This is equivalent with an open water test of a propeller with uniform inflow. The resulting loading coefficient for a waterjet with undisturbed inflow yields:

$$C_{Tnozzle}\Big|_{w=0} = \frac{2(1-\mu)}{\mu^2} \tag{2.54}$$

Comparison with the open propeller thrust loading coefficient (equation (2.44)) reveals a difference between the waterjet and the open propeller. This is due to the fact that a waterjet is an internal flow machine. For a waterjet the ratio between the inlet and nozzle area is fixed, whereas it is related to the thrust for an open propeller.

The waterjet thrust loading coefficient can also be based on the pump inlet diameter. In this way the dimensions of the complete installation are recognised more clearly. This approach is more in agreement with the open propeller thrust loading coefficient, where the propeller diameter is used.

$$C_{Tpump} = \frac{T}{\frac{1}{2}\rho v_{ship}^2 A_{pump}} = \frac{2(1-\mu)(1-w)^2}{IVR \cdot \mu} \qquad (2.55)$$

The thrust loading coefficient based on the pump inlet diameter shows that the *IVR* is introduced to describe the system performance. This gives the designer of waterjets another optimization option, compared to open propellers.

2.3.4   Concluding remarks

In a waterjet there is no direct relation between the IVR and μ like there is for an open propeller. Since it is an internal flow machine, part of the thrust can be transferred to the hull structure via the transom stern and the inlet ducting. On the other hand, it can also appear that the thrust acting on the shaft will exceed the total thrust of the installation [19]. In such condition a negative thrust acts on the transom stern or the inlet ducting. For conventional pumps the axial thrust is to be kept as low as possible. Thrust production is not regarded as an important performance indicator, like efficiency and head as function of the mass flow.

In case of a waterjet, the thrust can be calculated, if the values for the velocities v_{in}, v_{pump} and v_{out} are known. These can be related to the mass flow for a given geometry of the waterjet installation. This mass flow through the system is related to the pump head. In this way the standard pump performance characteristics, like head curve, efficiency and cavitation behaviour, can be used to evaluate the performance of a waterjet installation.

2.4   Pump head

The required head of a waterjet installation will be discussed in this section. The head H of a pump represents the increase of total pressure in a pump measured in meters liquid water column as given in equation (2.32).

The volume flow rate through the system follows from the intersection of the required system head curve and the pump head curve. The pump head curve depends on the type of pump used in the waterjet system. In general, mixed-flow pumps have a head-curve with a negative slope in the design point to ensure a stable operating point. For lower volume flow rates the slope may become zero or even negative. For the sake of simplicity, the pump head curve, as used in the examples in this section, is assumed to be a linear function of flow rate.

The required system head curve can be regarded as a pipe resistance curve of the waterjet installation. The acceleration of the fluid in the nozzle requires a certain pressure difference. Additional head is required to overcome the hydraulic losses in the inlet and the nozzle. However, the energy of the ingested fluid can be used partly, which is beneficial for the head requirement. Finally, the waterjet nozzle may be positioned above the waterline, which will require some more pump head. All contributions together give the equation for the required system head H_R:

$$H_R = \frac{v_{out}^2}{2g}(1 + \phi) - \frac{v_{in}^2}{2g}(1 - \varepsilon) + h_j \qquad (2.56)$$

where ϕ is the nozzle loss coefficient, ε the inlet loss coefficient and h_j the nozzle elevation above the waterline. The elevation of the nozzle is limited by the self-priming requirement of the waterjet installation. In general, the elevation h_j can be neglected relative to the other contributions in equation (2.56).

Equation (2.56) shows a positive contribution from the incoming velocity, therefore the system performance is coupled to the ship speed. Strictly speaking, the average ingested velocity v_{in} should be based on a mass averaged dynamic pressure term:

$$\tilde{v}_{in} = \left[\frac{1}{Q} \int_A v(z)^2 v_n dA \right]^{1/2} \qquad (2.57)$$

whereas v_{in} in equation (2.56) is based on the mass averaged velocity as given in equation (2.1). The difference between the two methods can be expressed in the power-law exponent, assumed that the water is ingested completely out of the boundary layer:

$$\frac{\tilde{v}_{in}^2}{v_{in}^2} = \frac{(n+2)^2}{(n+3)(n+1)} \qquad (2.58)$$

The difference between the two methods of averaging is less than 1% for a power-law exponent of n=9. The error will be even smaller if the water is ingested from the undisturbed fluid. In general, the introduced deviation is compensated for in the determination of the loss coefficient.

At constant ship speed, the required system head H_R can be approximated as a quadratic function of the flow rate Q. The slope of this quadratic curve depends on the nozzle diameter. Figure 2.8 shows an example of a pump head diagram with a pump head and efficiency curve and two system lines for a constant ship speed and different nozzle sizes. The assumption of constant

ship speed is a hypothetical condition, since in actual situations, the ship speed will depend on the delivered thrust, which is in turn related to the flow rate.

The system lines are based on different nozzle diameters. An increase of the nozzle diameter, results in a lower nozzle velocity for constant volume flow. This leads to a lower required head. The work point of the pump can be controlled by the size of the nozzle exit area.

The effect of the ship speed on the volume flow through the installation is shown in figure 2.9. In this pump head diagram, the system lines of ship speeds of 20, 30 and 40 knots are plotted. The nozzle size is kept constant in this figure.

It can be observed from this diagram, that the increase in volume flow between 20 and 40 knots is only 6%. This increase in velocity through the impeller results in a small change of the pump operating point. It is concluded that a waterjet installation can operate in a relatively small range of flow rates.
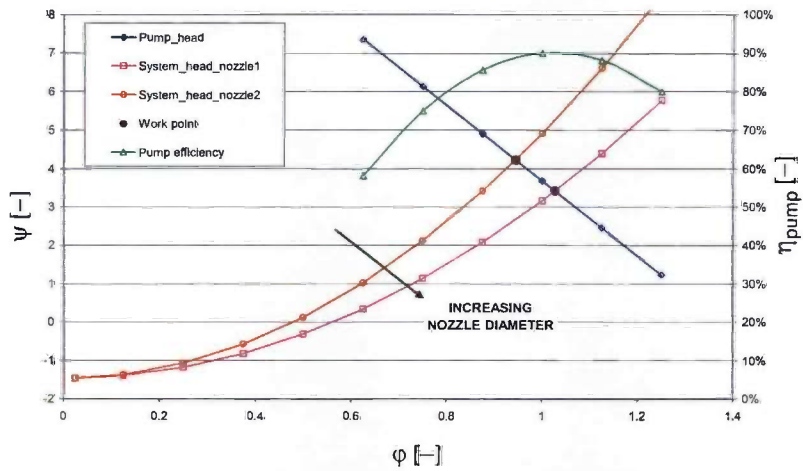
Figure 2.8   Pump head diagram for different nozzle sizes and constant ship speed
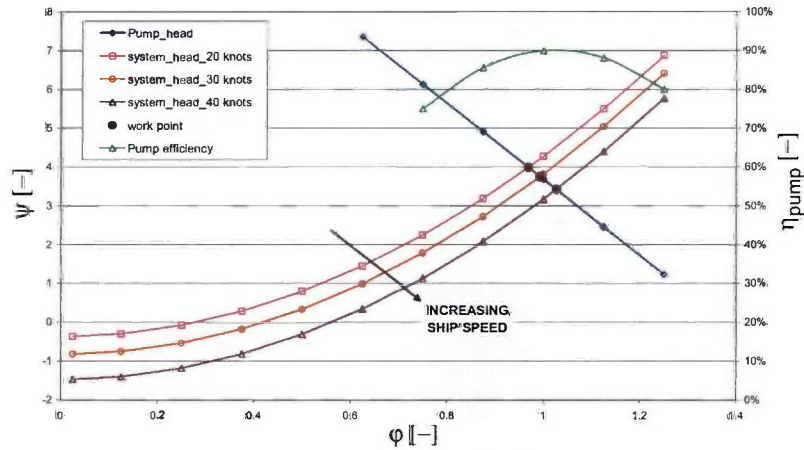
Figure 2.9. Pump head diagram for different ship speeds

2.5 Overall propulsive efficiency

This section deals with the influence of the parameter μ on the overall propulsive efficiency. If the propulsion system is regarded as a black box, then engine power P_{shaft} is input and thrust T at a certain ship speed is output. The overall propulsive efficiency η_d of this black box is then based on the bare hull resistance R_{bh} of a vessel [18]:

$$\eta_d = \frac{R_{bh} \cdot v_{ship}}{P_{shaft}} \tag{2.59}$$

where R_{bh} is the bare hull ship resistance and P_{shaft} the power at the waterjet shaft.

In conventional naval architecture theory, the resistance of a ship with an active propeller is found to be different from the bare hull resistance. Due to the action of the propeller, a low pressure region at the rear of the vessel is created, which results in an increased drag of the vessel. The difference between the bare hull resistance R_{bh} and the required thrust T at a certain ship speed is expressed in terms of the thrust deduction factor t according to:

$$R_{bh} = (1-t) \cdot T \tag{2.60}$$

For a propeller the thrust deduction factor is always positive, which leads to a higher ship resistance due to the action of the propeller and therefore a higher required thrust.

In waterjet propulsion theory, the thrust deduction factor t can be used to account for the effects of (i) the neglected surface forces such as the force on the streamtube and the force on the region aft of the waterjet inlet and (ii) a change in the pressure distribution along the hull. This approach is used by Van Terwisga [2], where a jet thrust deduction factor t_j and a resistance increment factor $1+r$ are introduced.

Substitution of equations (2.2), (2.20) and (2.60) in equation (2.59) gives:

$$\eta_d = \frac{(1-t)}{(1-w)}\eta_{pump}\frac{T \cdot v_{in}}{\rho g H Q} \tag{2.61}$$

In the next step, equations (2.14), (2.52) and (2.56) are substituted into equation (2.61). After rearranging of all variables, the equation for overall propulsive efficiency becomes:

$$\eta_d = \frac{(1-t)}{(1-w)} \cdot \eta_{pump} \cdot \frac{2\mu(1-\mu)}{(1+\phi)-\mu^2(1-\varepsilon)} \tag{2.62}$$

where the first term is denoted as hull efficiency:

$$\eta_{hull} = \frac{(1-t)}{(1-w)} \tag{2.63}$$

Eqn (2.62) shows that the overall propulsive efficiency is mainly a function of the jet velocity ratio μ, since the hull efficiency η_{hull} and the pump efficiency η_{pump} as well as the inlet and nozzle loss coefficients may be regarded as constant values in a first approximation.

Figure 2.10 shows the overall propulsive efficiency for three inlet loss coefficients. Thrust deduction is set to t=-0.02, wake fraction to w=0.12, pump efficiency is 90% (η_{pump} = 0.90) and outlet loss coefficient is ϕ=0.02. Also plotted is the ideal efficiency, where all losses are neglected. This efficiency is defined already as Froude efficiency in equation (2.45) for an open propeller.

It is obvious that the optimum propulsive efficiency can be obtained, if the jet velocity ratio is in the range of 0.65 to 0.75 depending on the inlet loss coefficient ε. In general the design point is chosen at a jet velocity ratio, which is slightly below the best efficiency point. This part of the curve is relatively flat, which results in a stable working point, when the inflow conditions show some variation.
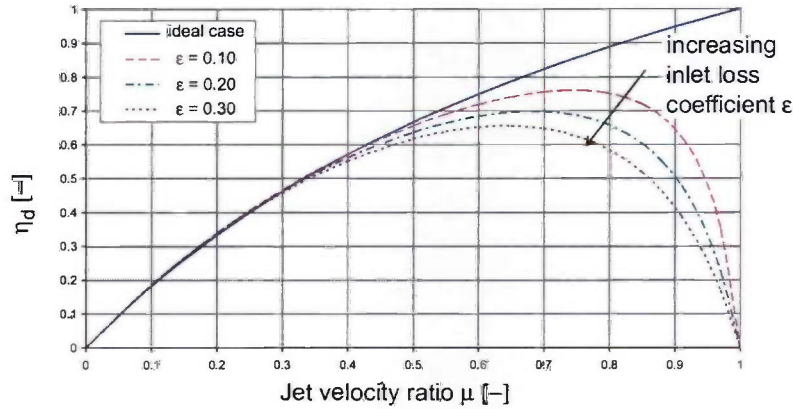
Figure 2.10 *Overall propulsive efficiency η_d as function of jet velocity ratio μ. Thrust deduction factor t=-0.02, wake fraction w=0.12, pump efficiency η_{pump}=90%, nozzle loss coefficient ϕ=0.02*

2.5.1 Cavitation margins

The waterjet pump needs a certain level of the pressure at the suction side of the pump in order to prevent cavitation. This required pressure is expressed in the required net positive suction head (NPSH$_R$), which is introduced in section 2.2.3. Pump operation is allowed as long as the available NPSH exceeds the required NPSH. The available suction head is the total head at the inlet of the pump minus the vapour pressure of the liquid. For a waterjet installation the available suction head is determined by the waterjet operating point. The $NPSH_A$ can be expressed as function of the ship speed:

$$NPSH_A = \frac{p_\infty - p_v}{\rho g} + \frac{v_{in}^2}{2g}(1 - \varepsilon) = \frac{p_\infty - p_v}{\rho g} + \frac{v_{ship}^2}{2g}(1 - \varepsilon)(1 - w)^2 - h_j \quad (2.64)$$

where h_j represents the elevation of the pump above the waterline. Due to self-priming constrains of the pump, this elevation is negligible in most cases. The pump will perform well as long as the required inlet suction head ($NPSH_R$) is below the available inlet suction head ($NPSH_A$):

$$NPSH_R \leq NPSH_A \quad (2.65)$$

Combination of equations (2.18) and (2.29), with the requirement of equation (2.65) yields:

$$n_\omega = n_{\omega s}\left(\frac{NPSH_R}{H}\right)^{3/4} \leq n_{\omega s}\left(\frac{NPSH_A}{H}\right)^{3/4} \tag{2.66}$$

2.5.2 Limitations in specific speed

The expressions for pump head (2.56) and available suction head (2.64), with negligible pump elevation, can be substituted into equation (2.66). Given values for the suction specific speed $n_{\omega s}$, the wake fraction w and the inlet and outlet loss coefficients ε and ϕ, a function of the ship speed and the jet velocity ratio is found for the maximum allowable specific speed:

$$n_\omega \leq n_{\omega s} \cdot \left[\frac{\dfrac{2(p_\infty - p_v)}{\rho v_{ship}^2(1-w)^2} + (1-\varepsilon)}{\left(\dfrac{1+\phi}{\mu^2}\right) - (1-\varepsilon)}\right]^{3/4} \tag{2.67}$$

This equation shows that the allowable specific speed of the pump will be limited for constant jet velocity ratio μ, when the ship speed increases. This phenomenon is illustrated in figure 2.11 for different values of the jet velocity ratio.
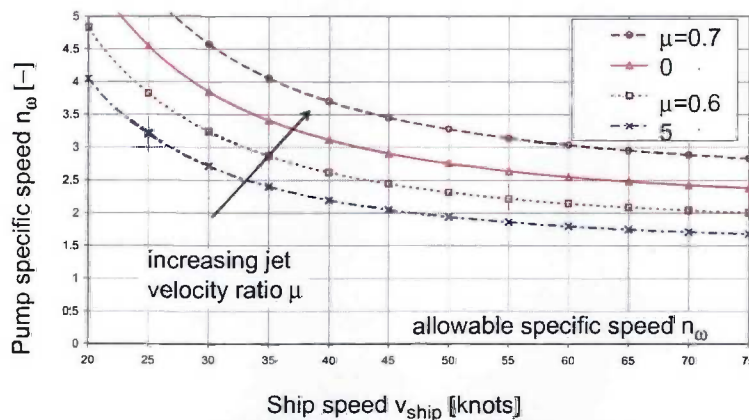
Figure 2.11   *Maximum allowable pump specific speed as a function of ship speed for various jet velocity ratios. Inlet loss $\varepsilon = 0.20$, outlet loss $\phi = 0.02$, wake fraction $w = 0.12$ and suction specific speed $n_{\omega s} = 3.5$.*

For a given design speed and a chosen jet velocity ratio the maximum allowable pump specific speed can be determined. On the other hand, for a certain available pump type, with a known specific speed, the range of possible jet velocity ratios can be determined for a given design ship speed.

2.5.3 Limitations in jet velocity ratio

In practice, to cover the complete speed range waterjet manufacturers use a set of standard pumps with different specific speeds. The allowable jet velocity ratio for given specific speed can be determined after rearranging equation (2.67). Figure 2.12 shows the minimum allowable jet velocity ratio μ for a number of specific pump speeds n_ω. This diagram shows that the optimal jet velocity ratio μ can be selected over a large range of ship speeds with a limited number of different pumps.

A jet velocity ratio of 0.7 is possible up to 35 knots for a pump with a specific speed of 4.0. A pump with a specific speed of 3.0 can be used at 65 knots for this jet velocity ratio, however. It is also shown that the range of allowable jet velocity ratios at very high ship speeds (>60 knots) increases significantly for a radial-flow type pump (n_ω=2.0) compared to an axial flow type pump. A pump with a specific speed of 4.0 requires a minimum jet velocity ratio of 0.78 at 65 knots. This condition may be at the right side of the optimum propulsive efficiency curve, as shown in figure 2.10. Since this is undesirable, a pump with lower specific speed is to be used.
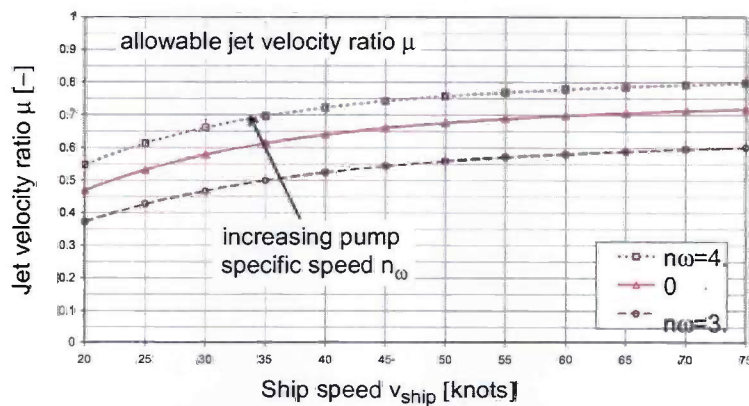
Figure 2.12 Minimum allowable jet velocity ratio as a function of ship speed for various pump specific speeds. Inlet loss ε = 0.20, outlet loss ϕ = 0.02, wake fraction w = 0.12 and suction specific speed $n_{\omega s}$ = 3.5.

2.5.4 Limitation of power density

Weight reduction of a waterjet installation is an important issue. This can be achieved with highly loaded, small installations. This criterion can be expressed in terms of the power density P/D^2 given in terms of the specific power P^* (according to equation (2.22)):

$$\frac{P_{shaft}}{D^2} = \rho P^*(\Omega D)^3 \tag{2.68}$$

with (ΩD) twice the tip speed of the impeller:

$$v_{tip} = \pi n D = \frac{1}{2}\Omega D \tag{2.69}$$

Cavitation behaviour of different pump sizes with the same specific speed can be compared with the net positive suction head coefficient κ, as defined in equation (2.27). This gives a relation between the required NPSH and the tip speed. Since the available NPSH is a function of the ship speed, it is found that the allowable tip speed increases with ship speed. Consequently, the allowable power density P/D^2 increases also with increasing ship speed.

Effect of the ship speed on the allowable power density is shown in figure 2.13. It should be obvious that an increase of the impeller diameter reduces the power density for given engine power. Consequently, the minimum allowable impeller diameter as function of the ship speed can be determined
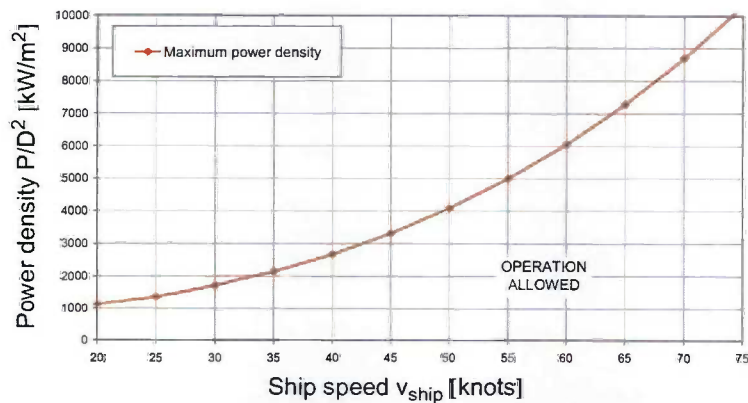
Figure 2.13   Maximum allowable power density as function of ship speed. Inlet loss $\varepsilon = 0.20$, wake fraction $w = 0.12$, non-dimensional flow coefficient $\varphi = 0.2$, specific speed $n_s = 3.0$ and suction specific speed $n_{\omega s} = 3.5$.

from the power density. It is found that the minimum allowable size depends on the cavitation behaviour of the pump, the ship speed and the power applied to the pump.

2.6   Waterjet selection

Up to this point, the entire analysis has been based on optimal performance at one single design operating condition. In many cases waterjet installations have multiple operating points. If the waterjets are applied for example in large fast ferries or planing hulls, the resistance line is quite different from the one of a regular displacement vessel. There is an additional resistance at a speed range between about 20 and 30 knots. The speed, at which the local maximum resistance occurs, is denoted as hump speed. The waterjet installation has to provide sufficient thrust to exceed the resistance at the hump speed. This requirement may lead to a larger waterjet than necessary for the design operating point.

In all shown examples, values for the wake fraction μ, pump efficiency η_{pump}, inlet losses, etc., have been considered as constants. In actual installations all these parameters depend on the ship speed and/or the flow rate Q through the installation. Implementation of all of these dependencies will result in a complex waterjet performance prediction program.

For a realistic comparison of various installations with different sizes over the complete range of ship speeds, such program should be used in order to take the actual values for the loss coefficients and the efficiencies into account.

Figure 2.14 shows the output of a waterjet performance prediction program as used at the authors' company for three different sized waterjets. The thrust is kept constant and the size is changed to show the effect of power density on the cavitation margins. The hatched area represents the non-continuous operational region. In this region severe cavitation in the waterjet will be present. The upper line represents the thrust breakdown line and the lower line of this area is denoted as the 1% cavitation line. Thrust breakdown occurs when the mass flow through the system collapses due to extreme cavitation.

In the same figure an indication of a typical resistance curve of a fast ferry is plotted. The increased resistance at the hump speed of 25 knots can be noticed. The effect of waterjet size is obvious from this figure. The resistance at the hump speed is about equal to the maximum thrust of the small waterjet. This means that the vessel has no extra thrust available to accelerate. The maximum speed will not exceed 25 knots in this case, which is only 55% of the design speed. The larger waterjets, with lower power densities, have sufficient margin up to the design speed. To get a good balance between cavitation performance and weight of the installation, the mid-size jet will be selected for this application.
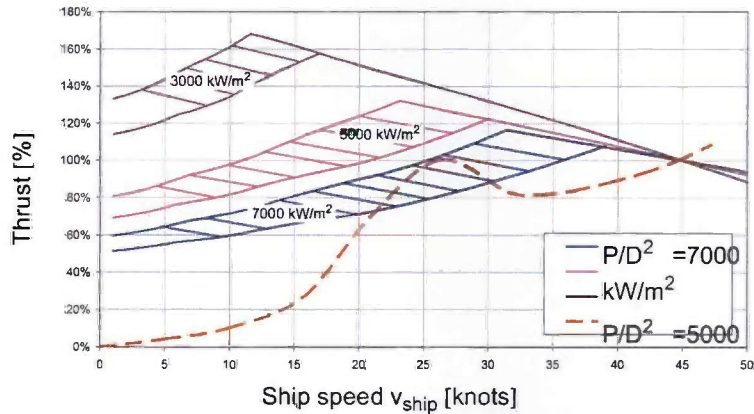
Figure 2.14   Maximum thrust curves for three different waterjet sizes and resistance curves for fast ferry.

2.7   Closing remark

All equations and empirical values in this chapter are based on a uniform inflow to the pump. However, the inflow velocity field of a waterjet shows a strong non-uniform distribution, with variations in radial and tangential direction. This inflow might have an influence on the empirical values or the pump performance itself. Effects of the non-uniformity on pump performance will be reviewed in more detail in chapter 7, where the complete waterjet installation is analysed numerically.

2.8   Nomenclature

A	area	m^2
$c_f(l)$	local wall friction coefficient	-
D	diameter	m
F	force	N
g	gravitational acceleration	m/s^2
H	pump head	m
h_j	nozzle elevation	m
IVR	inlet velocity ratio (v_{ship}/v_{pump})	-
l	wetted length	m
$NPSH$	Nett positive suction head	m

n_ω	pump specific speed	-
$n_{\omega s}$	suction specific speed	-
n	propeller/pump shaft speed	1/s
n	boundary layer power law exponent	-
P	power	W
P^*	specific power	-
p	pressure	N/m^2
Q	volume flow rate	m^3/s
R	resistance	N
Re_l	Reynolds number based on length	-
T	thrust	N
t	thrust deduction factor	-
U_∞	undisturbed free stream velocity	m/s
v	velocity	m/s
w	momentum wake fraction	-
z	distance normal to the wall	m

Greek symbols

δ	specific pump diameter	-
δ	boundary layer thickness	m
δ_1	boundary layer displacement thickness	m
δ_2	boundary layer momentum thickness	m
δ_3	boundary layer energy thickness	m
ε	inlet loss coefficient	-
ϕ	momentum flux	N
ϕ	nozzle loss coefficient	-
η	efficiency	-
φ	flow coefficient	-
κ	net positive suction head coefficient	-
μ	jet velocity ratio	-
ρ	fluid density	kg/m^3
σ	Thoma number	-
τ_w	wall shear stress	N/m^2
Ω	angular velocity	rad/s
ψ	head coefficient	-

Subscripts

1	inflow plane	

A	available
in	inflow
ind	induced
out	ouflet / nozzle
prop	propeller
R	required
tube	streamtube
wj,all	complete waterjet structure
wj,hull	excluded part of waterjet streamtube control volume
wj,tube	included part of waterjet streamtube control volume

2.9   References

[1] Roberts, J.L. & Walker, G.J.,'Boundary layer ingestion in flush waterjet intakes', Proceedings RINA Waterjet Propulsion II conference, Amsterdam, 1998

[2] Terwisga, T.J.C. van,'Waterjet hull interaction', PhD thesis, Delft University,1996

[3] Wilson, M.B., Chesnakas, C., Gowing, S., Becnel, A.J., Purnell, J.G., Stricker, J.G., 'Analysis of hull boundary layer velocity distributions with and without active waterjet inlets', RINA Waterjet IV conference, London, 2004

[4] Schlichting, H., 'Boundary layer theory', McGraw-Hill, New York, 1968

[5] Fox, R.W., & McDonald, A.T.,'Introduction to fluid mechanics', Third Edition, John Wiley & Sons, New York, 1985

[6] Newman, J.N., 'Marine hydrodynamics', MIT press, Cambridge, 1977

[7] Svensson, R. & Grossi, L.,'Trial result including wake measurements from the world's largest waterjet installation', Proceedings RINA Waterjet Propulsion II conference, Amsterdam, 1998

[8] Seil, G.J., 'Development of waterjet inlets for 100 knots', Proceedings FAST'99 conference, pp. 853-868, Seattle, 1999

[9] Bulten, N. & Verbeek, R.,'Design of optimal inlet duct geometry based on operational profile', Proceedings FAST2003 conference Vol I, session A2, pp 35-40, Ischia, Italy, 2003

[10] Verbeek, R.,'Application of waterjets in high-speed craft', in Hydrodynamics: Computations, Model Tests and Reality, H.J.J. van den Boom (Editor) Elsevier Science Publication, 1992

[11] Stepanoff, A.J., 'Centrifugal and axial pumps; theory, design and application', John Wiley & Sons, New York, 1957

[12] Wislicenus, G.F., 'Fluid mechanics of turbomachinery', Dover, New York, 1965

[13] MacPherson, D.M., 'A universal parametric model for waterjet performance', Proceedings FAST'99 conference, pp. 879-882, Seattle, 1999

[14] Bohl, W.,'Strömungsmachinen (Aufbau und Wirkungsweise)', Vogel verlag, Würzburg, 1977

[15] Arnold, J., Nijhuis, G.J., 'Selection, design and operation of rotodynamic pumps', Published by Nijhuis Pompen, first edition, 2005

[16] Gülich, J.F., 'Kreiselpumpen', Springer Verlag, Berlin, 1999

[17] Os, M.J. van,'On the flow and cavitation inception of mixed-flow impellers', PhD thesis, Twente University, 1997

[18] Lewis, E.V., 'Principles of naval architecture', Volume II, Society of Naval Architects and Marine Engineers, Jersey City, 1998

[19] Verbeek, R.,'Waterjet forces and transom flange design', RINA waterjet propulsion conference, London, 1994

Chapter 3 Non-uniform distribution of pump entrance velocity field

The theory as presented in chapter 2 is based on experience with pumps with uniform inflow. It is known that in normal operating conditions the inflow velocity in waterjet pumps is far from uniform. The first developers of waterjets have accepted this phenomenon; most probably since it has clear similarities with a ship-propeller wake field.

In the following subsection some methods will be presented to represent the non-uniform pump inflow velocity distribution. With such representation it is possible to derive an estimation of the flow rate fluctuations through an impeller channel and the variations of the inflow angle at the leading edge of the blade.

Obviously, the non-uniformity should be kept minimal from a hydrodynamic point of view. Therefore, a thorough analysis of the contributing factors to the non-uniformity is made. In section 3.4 it will be shown that the major contributions are unavoidable in waterjet applications with flush type inlets.

3.1   Representation of non-uniform velocity distribution

In order to get an impression of the type of non-uniform velocity distributions discussed here, typical distributions will be shown in this section. The distributions are derived from experimental results. The distributions can be expressed as non-dimensional parameters or with a two-dimensional representation. Both methods will be discussed in this section as well.

3.1.1   Experimental set-up

Measurements have been carried out on a model scale inlet, which is mounted on the Tom Fink cavitation tunnel [1]. A sketch of the test set-up is shown in figure 3.1. The model scale inlet has an inlet diameter of 150 mm. In the model scale test-rig the actual waterjet pump is not included. Though, the impeller drive shaft, with a diameter of 22 mm, is included in the test set-up. The tunnel has a square cross-section of 600 x 600 mm.

At a cross-sectional plane just upstream of the pump, which will be denoted as impeller plane, the velocity distribution is measured with a 3 hole Pitot-tube.

Experiments have been carried out with a constant tunnel speed v_{tunnel} of 8 m/s. Upstream of the inlet an serrated edge is applied to thicken the natural tunnel wall boundary layer. The shape of the edge is selected after an extensive test procedure. During the tests the growth of the boundary layer thickness and the smoothness of the profiles was evaluated.

The mass flow through the inlet is adjusted to get the desired IVR values, as defined in equation (2.12). The tunnel v_{tunnel} is used to represent the ship speed v_{ship}. The measured conditions are listed in the table below. Reynolds number for these conditions is based on the diameter of the inlet D and the averaged pump velocity v_{pump}.

Figure 3.2 shows the axial velocity distributions for two inlet velocity ratios, derived from the measurements. The condition with an IVR of 1.68 represents a normal cruising speed of a fast ferry. The figure on the right shows the distribution at very high IVR. This condition can occur in high speed motor yacht applications (> 60 knots). It should be noted that the shaft
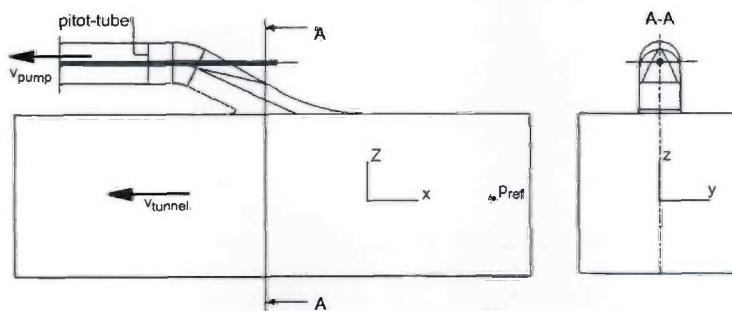
Figure 3.1   Sketch of test setup with inlet mounted on top of cavitation tunnel

Table 3.1   Parameters of conditions of the measured velocity distributions

IVR [-]	V_{tunnel} [m/s]	V_{pump} [m/s]	Re_{inl} [-]
1.68	8.00	4.76	7.14×10^5
1.87	8.00	4.28	6.42×10^5
2.03	8.00	3.94	5.91×10^5
2.19	8.00	3.65	5.48×10^5

diameter (d=22 mm) is about half the diameter of the non measured (blank) region. Moreover, it should be taken into account that the shaft was not rotating during experiments, which results in a symmetric velocity profile.

Similar velocity distributions are found for another inlet geometry in this test-rig. The measurements in the cavitation tunnel indicate that the level of non-uniformity is almost independent of the actual inlet geometry. Measurements in a windtunnel with systematic changes of the geometry confirm this behaviour [2]. It is concluded that the non-uniformity is strongly related to the inlet velocity ratio and only weakly related to the precise shape of the inlet.

Based on a survey of the available (confidential) experimental and numerical data at the authors' company, it is concluded that within the design space for commercial applications all possible inlet geometries show more or less the same type of velocity distribution.
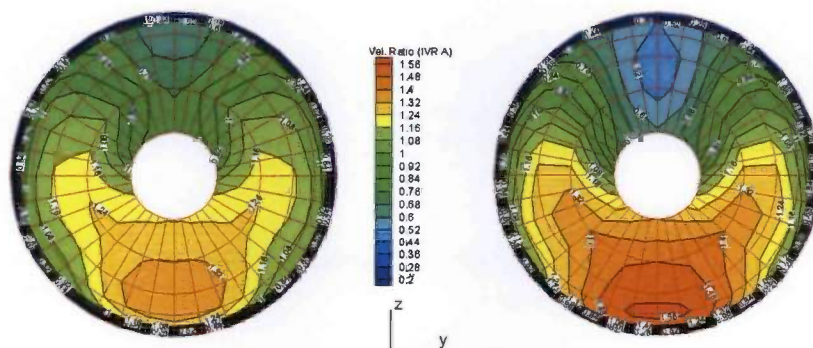
Figure 3.2   Experimentally determined non-uniform velocity distributions for 2 IVR conditions. Left: medium IVR of 1.68, right high IVR of 2.19.

3.1.2 Non-dimensional representation

For easy comparison of different inlet geometries and operating conditions, the level of non-uniformity is expressed as a single value ζ [3]:

$$\zeta \equiv \frac{1}{Q} \int \sqrt{(v - v_{pump})^2} \, dA \tag{3.1}$$

where v is the local axial velocity and v_{pump} the average axial velocity. The relation between non-uniformity and IVR can be assessed with this parameter.

3.1.3 Two-dimensional representation

Hu&Zangeneh [4] use a circumferentially averaged velocity distribution to investigate the effects of the non-uniform velocity distribution on the waterjet pump performance. However, for a detailed analysis of the time-dependent effects of non-uniformity on pump performance, this quantification is not sufficient. At least a two dimensional description, based on the radius r and the angle θ, of the inflow field in front of the impeller is required to capture the time varying phenomena.

Such a description of the axial velocity distribution can be obtained if the velocity field is approximated as a Fourier series:

$$v_x(r, \theta) = a_0(r) + \sum_{n=1}^{m} (a_n(r)\cos(n\theta)) \tag{3.2}$$

where the coefficients $a_n(r)$ are taken as quadratic functions of the radius and m is the number of harmonics. For the present Fourier approximation 4 harmonics have been used. The quadratic functions $a_n(r)$ are based on coefficients at five different radii. Results of the two dimensional velocity field description are shown in figure 3.3 for the condition IVR=2.19 together with the measured values.

Agreement between measurements and the numerical approximation is satisfactory for all radii along the complete circumference. A similar agreement is found at lower IVR.
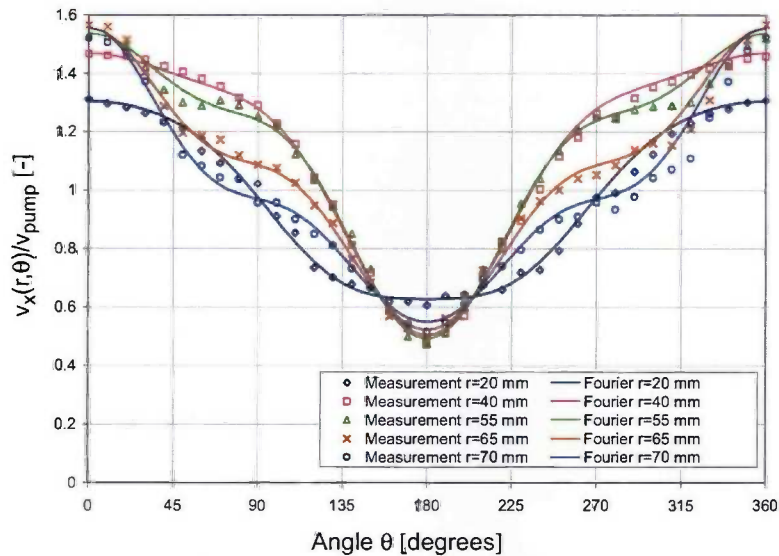
Figure 3.3   *Comparison of axial velocity derived from measurements with the velocities based on Fourier series for velocity distribution at IVR = 2.19*

3.2   Local flow rate fluctuations

It is expected that the non-uniform inflow velocity distribution will result in a varying flow rate through the channels between the impeller blades during a revolution. The amplitude of the fluctuation is not only dependent on the level of non-uniformity of the velocity distribution but also on the number of impeller blades. An estimation of the channel flow rate as function of the rotor position can be calculated with:

$$Q_{bb} = \int_{\theta - \frac{\pi}{N}}^{\theta + \frac{\pi}{N}} \int_{r_1}^{r_2} v_x(r, \theta) \cdot r \, dr \, d\theta \qquad (3.3)$$

where the axial velocity v_x is integrated over the impeller passage inlet area, with N the number of impeller blades, Q_{bb} the volume flow rate in an impeller channel, r_1 the hub radius and r_2 the tip radius at the impeller inlet.
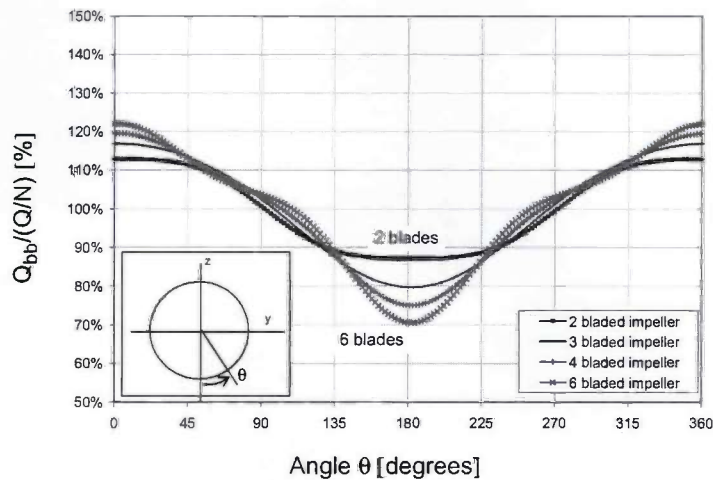
Figure 3.4   *Local flow rate estimate as a function of impeller channel position for medium IVR of 1.68, using data of figure 3.3.*

In figures 3.4 and 3.5 the normalised local flow rate estimate is presented for medium and high IVR and for impellers with different number of blades. In these figures the channel flow rate Q_{bb} is normalised with the averaged flow rate per channel (Q/N).

As expected, the amplitude increases with increasing IVR. The six bladed impeller shows a flow rate deficit of 30% for the medium IVR in figure 3.4, which increases to 46% for the high IVR condition, as shown in figure 3.5.

For impellers with only three blades the amplitude of the variation is smaller. The flow rate deficit is 20% at medium IVR and 35% at high IVR.

The actual local flow rate through an impeller channel for different IVR conditions will be determined in chapter 6.
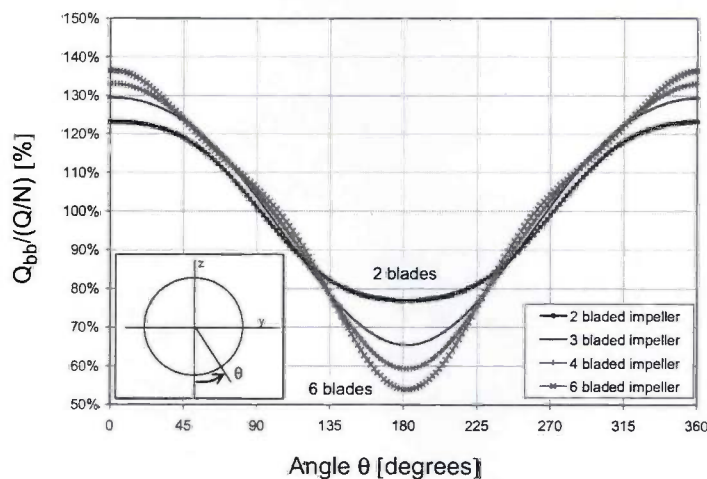
Figure 3.5 *Local flow rate estimate as a function of impeller channel position for high IVR of 2.19, using data of figure 3.3.*

3.3 Impeller velocity triangles

The axial velocity distribution can be used to derive the fluctuations in inlet flow angles. This angle determines for a great deal the loading of the impeller blade. A lower inlet flow angle will lead to higher blade loading in general. Moreover the cavitation behaviour of the impeller will depend on the fluctuations of the inflow angle.

The design inlet blade angle is based on the inlet velocity triangle with uniform flow and without pre-rotation, as shown in figure 3.6:

$$\beta_{design} = atan\left(\frac{v_x}{\Omega r}\right) \tag{3.4}$$
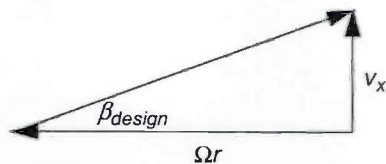
Figure 3.6 *Velocity triangle of inlet flow angle.*

The actual inflow angle will vary due to the axial velocity variations:

$$\beta_{actual} = atan\left(\frac{v_x(r, \theta)}{\Omega r}\right) \qquad (3.5)$$

where $v_x(r,\theta)$ is the local axial velocity. The incidence angle is the difference between the design angle and the actual inflow angle. Note that cross-flow plane velocity components are neglected in this approach. This simplification is allowed, since the tangential velocities are small compared to the tangential velocity component Ωr of the impeller. Typical cross-flow plane velocities are about 5% of the tip speed of the impeller.

Figure 3.7 shows the estimation of the incidence angle for high IVR. The deviations vary from +10 degrees to -10 degrees at the outer radii. It is to be expected that such amplitude of inflow angles will result in significant variation of the impeller blade loading during a revolution of the blade.
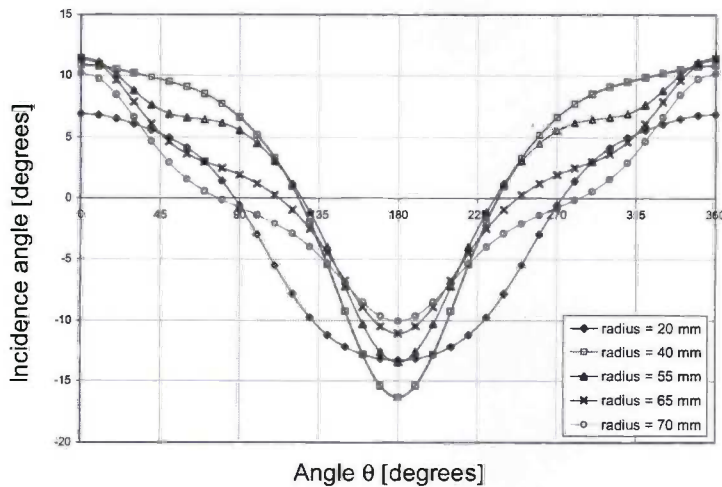
Figure 3.7   Estimation of the incidence angle as function of impeller channel position for the velocity distribution at IVR = 2.19

3.4   Origin of the non-uniform velocity distribution

The development of the non-uniform velocity distribution can be explained with basic fluid dynamics theory. There are four phenomena which contribute to the non-uniformity of the velocity distribution:

1. boundary layer ingestion
2. deceleration of the flow
3. obstruction of the flow due to the shaft
4. bend in the inlet duct

A sketch of the phenomena is presented in figure 3.8. The above items are discussed in more detail in the remainder of this section.
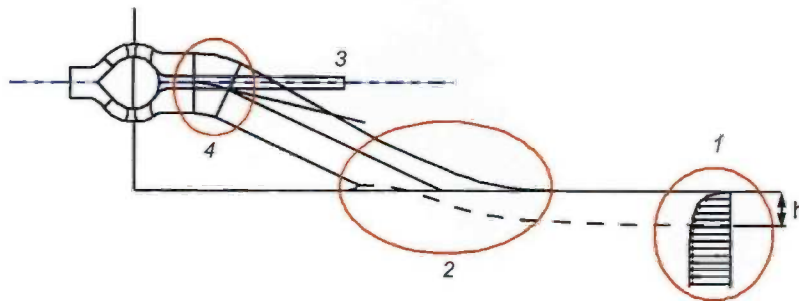
Figure 3.8   *Phenomena which contribute to development of a non-uniform inflow velocity distribution to the pump. 1. boundary layer ingestion. 2. deceleration of the flow. 3. obstruction of the flow by shaft. 4. bend in duct.*

3.4.1   Boundary layer ingestion

Waterjets with flush mounted inlet ducts ingest water from the boundary layer below the hull. A typical ship speed for a waterjet propelled vessel is 40 knots (about 20 m/s). With a wetted length of 80 m, the Reynolds number becomes 1.6×10^9. At these high Reynolds numbers the boundary layer thickness can be approximated with a power law velocity distribution, as shown in equation (2.3), with a power n of about 10.

The contribution of the boundary layer ingestion to the non-uniformity depends on the amount of water that is ingested from the boundary layer. The ingestion of boundary layer water can be expressed with the ratio between the suction depth h and the boundary layer thickness δ. If this ratio (h/δ) is smaller than 1, then all the water is taken from the hull boundary layer.

The suction depth h depends on the total ingested volume flow rate and the assumed shape of the streamtube. As mentioned before, waterjet manufacturers and ship model basins use a simplified method, in which the shape of the streamtube is approximated as a rectangular box with a width of 1.3 times the inlet diameter.

When the suction depth h is smaller than the boundary layer thickness, the suction depth h is calculated with:

$$h = \left(\frac{Q}{v_{ship}\lambda D} \cdot \frac{n+1}{n} \cdot \delta^{1/n} \right)^{n/(n+1)} \qquad (h < \delta) \qquad (3.6)$$

where Q is the volume flow, v_{ship} the undisturbed velocity and λD the assumed width of the rectangular box with λ equal to 1.3.

If the suction depth h exceeds the boundary layer thickness, then the displacement thickness can be used to calculate the suction depth h:

$$h = \frac{Q}{v_{ship}\lambda D} + \delta_1 = \frac{Q}{v_{ship}\lambda D} + \frac{\delta}{n+1} \qquad (h > \delta) \qquad (3.7)$$

The relations for the boundary layer thickness (for example equation (2.10) for n=9) show that the length of the vessel has a major influence on the development of the boundary layer. This effect is shown more clearly in figure 3.9, where the boundary layer ingestion ratio h/δ is shown for three different vessel lengths. The flow rate Q is adjusted for each ship speed, to take the effect of increasing flow rate with increasing ship speed into account.

The ratio h/δ decreases with ship speed for all ship lengths. With higher incoming velocity and constant suction box width, the suction height h will reduce.

It can be seen that the boundary layer ingestion ratio h/δ is about 0.90 at 45 knots for the short vessel. The ratio is reduced to 0.50 when the length is doubled. Since the velocity profile has the largest gradients near the wall, this results in increased non-uniformity, for longer vessels. Decrease of the boundary layer ingestion ratio h/δ is coupled to an increase of IVR. As a consequence, the non-uniformity will increase with increasing IVR as well.

3.4.2 Deceleration of the flow

Waterjets operate in IVR conditions of 1.3 to 1.8 in general. The averaged velocity of the water just in front of the pump is thus smaller than the ship speed. Even if the velocity in front of the pump is compared with the mass averaged incoming velocity, which is smaller due to boundary layer development, there is still a significant retardation of the flow in the inlet duct. The retardation of the flow can be regarded as a (subsonic) diffuser flow
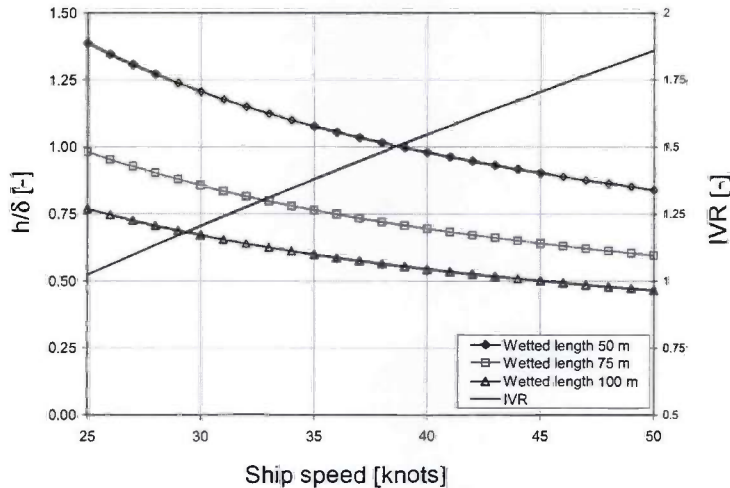
Figure 3.9   *Boundary layer ingestion ratio h/δ for three different vessel lengths l as function of ship speed v_{ship} with corresponding IVR.*

phenomenon. According to the theory of standard diffusors, the velocity profile in a conventional diffusor depends on the diffusor angle. Nikuradse measured the velocity profiles in convergent and divergent channels with diffusor angles between -4° and +8° (shown in Schlichting [5]). The velocity profiles in convergent channels, which have negative diffusor angles, become more uniform. In contrast, the velocity profile becomes less uniform in divergent channels (or in other words, it corresponds to a lower *n* value in a power law profile). Therefore, retardation of the flow increases the level of non-uniformity in the velocity distribution. Consequently, the increase of non-uniformity is related to the value of IVR.

The standard diffusor theory assumes a uniform inflow at the entrance of the diffusor. However in a waterjet the boundary layer creates a non-uniform distribution at the beginning of the diffusor. When a velocity profile is non-uniform at the entrance a diffusor, the level of non-uniformity will even increase. This phenomenon is explained by Betz [6] with a simple example.

3.4.3   Obstruction of the flow due to the shaft

The impeller shaft forms an obstruction of the flow in the inlet, comparable to a propeller shaft in a ship. A narrow wake region with low velocity is found near the shaft. If the pump shaft is equipped with a stationary sleeve, then it can lead to unstable vortex shedding. Hu & Zangeneh [7] and Seil [8]

investigated the effect of the rotation of the shaft. They show that the flow stabilizes due to rotation of the shaft. In general a waterjet installation does not have a stationary sleeve around the shaft, so a stable flow is found in the vicinity of the shaft.

3.4.4   Bend in the inlet duct

The fourth contributing factor to the non-uniform velocity distribution is the bend in the inlet duct. Inside the bend a variation in velocity is found between the inner and outer part of the bend. This non-uniformity will restore to a certain extent downstream of the bend. In a waterjet however, the length of the cylindrical pipe between the bend and the pump is in general smaller than the inlet diameter. As a result part of the created non-uniformity due to the bend remains in the velocity distribution.

The convex shape of the first part of the roof of the inlet may be regarded as a bend as well, which might have a positive influence on the velocity distribution. The radius of curvature is about six times larger than the radius of curvature of the bend, so the effect of this curvature can be neglected in the analysis and is therefore not marked in figure 3.8.

3.4.5   Closing remark

The major contributions to the non-uniformity are caused by the IVR related phenomena of boundary layer ingestion and retardation of the flow. As long as waterjets are operated at IVR values above 1.5, a substantial non-uniform flow will exist.

3.5   Non-uniform inflow velocity distributions in other turbo machinery

In the literature relatively little attention has been paid so far to the effects of non-uniform inflow to the waterjet pump. This may be attributed to its close relation to the conventional ship propeller, which also operates in a non-uniform wake field in general. This wake field is determined by the shape of the vessel, so the propulsion system designer has to cope with it. A lot of research has been done on the effects of non-uniform inflow to a ship propeller already. For example the work of Van Manen [9] in the 1950s can be mentioned. Variations in effective inflow angle for the tested propeller were between -1° and +4°. This range is significantly smaller than the expected variations for the waterjet pump, as shown in figure 3.7.

Non-uniform inflow to mixed-flow or centrifugal pumps may occur if the pump is mounted close to an upstream disturbance, like a pipe bend. For an acceptable inflow to the pump, most manufacturers prescribe a minimum

required length of straight pipe on the suction side of the pump, typically several pipe diameters long. Examples can be found in a pump handbook of Sulzer [10]. The use of an acceleration nozzle just upstream of the pump is also recommended to enhance the uniformity of the inflow for certain types of pumps.

The requirement of long straight suction pipes can not always be met, like the flow into the first stage of a boiler feed pump. Cooper [11] shows the calculated flow pattern at the exit of a radial inlet passageway for such a pump. A maximum velocity of 1.75 times the average inflow velocity is found for this example. This level of non-uniformity seems to be more in line with that found in waterjet applications. Similar flow phenomena will occur in double suction pumps and inline pumps.

Another typical inflow is found for pumps with a sump, as used in cooling water pump applications in power stations. Here a suitable design of the inflow and inlet chamber is to obtain an acceptable inflow pattern. Additional acceleration can be applied for further improvement.

3.6 Nomenclature

A	area	m^2
D	diameter	m
h	suction depth	m
IVR	inlet velocity ratio (v_{ship}/v_{pump})	-
N	number of impeller blades	-
n	boundary layer power law value	-
Q	flow rate	m^3/s
Q_{bb}	channel flow rate	-
r	radius	m
v	velocity	m/s

Greek symbols

β	blade angle	rad
δ	boundary layer thickness	m
δ_l	boundary layer displacement thickness	m
θ	angle	rad
λ	suction tube width factor	-
ζ	non-uniformity	-
Ω	angular velocity	rad/s

Subscripts

x   axial direction

3.7   References

[1] Brandner, P. & Walker, G.J., 'A waterjet test loop for the Tom Fink cavitation tunnel', Proceedings Waterjet Propulsion III conference, Gothenburg, 2001

[2] Bulten, N.W.H.,'Influence of boundary layer ingestion on waterjet performance parameters at high ship speeds', Proceedings of the 5th international conference on Fast Sea Transportation, pp 883-892, Seattle, 1999

[3] Verbeek, R. & Bulten, N.W.H.,'Recent developments in waterjet design', Proceedings RINA Waterjet Propulsion II conference, Amsterdam, 1998

[4] Hu, P. & Zangeneh, M.,'CFD calculation of the flow through a water-jet pump', Proceedings Waterjet Propulsion III conference, Gothenburg, 2001

[5] Schlichting, H.,'Boundary layer theory', Mc Graw-Hill, New York, 1968

[6] Betz, A, 'Introduction to the theory of flow machines', Pergamon Press, Oxford, 1966

[7] Hu, P., Zangeneh, M., 'Investigations of 3D turbulent flow inside and around a water-jet intake duct under different operating conditions', ASME Journal of Fluids Engineering, Vol 121, pp. 396-404, 1999

[8] Seil, G.J.,'The effect of the shaft, shaft rotation and scale on the flow in waterjet inlets', Proceedings Waterjet Propulsion III conference, Gothenburg, 2001

[9] Manen, J.D. van, 'Invloed van de ongelijkmatigheid van het snelheidsveld op het ontwerp van scheepsschroeven', PhD thesis, Wageningen, 1951

[10] Sulzer Brothers Ltd, 'Sulzer centrifugal pump handbook', Elsevier Applied Science, London, 1989

[11] Cooper, P.,'Perspective: the new face of R&D - A case study of the pump industry', ASME Journal of Fluids Engineering, Vol 118, pp. 654-664, 1996

Chapter 4   Mathematical treatment

To get more insight in the behaviour of the flow through a waterjet installation, experiments can be done and calculations can be made. With an experimental set-up of a waterjet inlet velocity, pressure and forces can be measured. In this thesis, however these quantities will be determined by numerical simulations.

A numerical method is based on a mathematical model of the physics of the flow. It constitutes a set of governing equations derived from first principles, often complemented with empirical relations. The numerical method is obtained by discretisation of the governing equations. The present type of flow can be described by the Navier-Stokes equations. Before these equation can be solved numerically for the application of interest, it is necessary to make some simplifications. A review of the important flow features is given in section 4.1 to get an impression of the feasible simplifications without major loss of accuracy. This analysis will result in a selection of the best suitable mathematical method. The chosen method will be described in more detail in section 4.3. Some known weaknesses of the mathematical method will be discussed in more detail to get an indication of the obtainable accuracy.

4.1   Requirements of mathematical method

In this section the requirements for the mathematical method will be formulated. The goal of the mathematical analysis is the prediction of the flow through a waterjet installation. Based on the different requirements for the prediction three different mathematical methods will be evaluated: the

potential flow model, the model based on the Euler flow and the model based on the Reynolds averaged Navier-Stokes (RANS) equations. RANS methods are also denoted as viscous methods, whereas the other two methods do not include terms due to viscosity and heat conduction. They require, for example effects of viscosity, such as flow separation, to be modelled. In potential flow methods, the flow is irrotational, i.e. the vorticity equals zero everywhere, except in infinitesimal regions such as vortex sheets and vortex filaments.

4.1.1   Incompressibility

The first requirement for the mathematical method is the capability of handling incompressible flow. The maximum velocity in a full scale waterjet installation is about 50 m/s, which is much smaller than the speed of sound in water, which is about 1450 m/s. The resulting Mach number is thus sufficiently small to treat the flow as incompressible. It is noted that the speed of sound is based on a non-cavitating flow. In a cavitating flow, the speed of sound reduces significantly, which results in a compressible flow behaviour.

All three mentioned mathematical methods can satisfy this requirement. Nevertheless it can be mentioned that this requirement represents one of the major differences between pumps and compressors, as discussed in section 1.2. mathematical methods for compressor analysis cannot be used directly for incompressible flow. For compressible flow the Euler equations are hyperbolic in time for any Mach number. This gives the opportunity to use a single numerical technique for subsonic, supersonic or mixed subsonic-supersonic (transonic) flow problems [1]. These methods are commonly called time marching methods. In these methods compressibility is employed, which results in amongst others travelling pressure waves through the domain. In an incompressible flow, pressure fluctuations are instantaneous in the whole domain. Reconditioning, i.e. some form of artificial compressibility has to be introduced in the compressible flow solver in order to analyse an incompressible flow.

4.1.2   High Reynolds number

For full scale waterjet installations the typical Reynolds numbers for the inlet and the impeller are both very large. For the impeller the Reynolds number is defined as:

$$Re_{imp} = \frac{\rho v_{tip} D_{inl}}{\mu} \qquad (4.1)$$

where ρ is the density, μ the dynamic viscosity, v_{tip} is the tip speed of the impeller blade and D_{inl} the diameter of the inlet at the pump suction side. For

typical waterjet applications the tip speed can be about 50 m/s. For an inlet diameter of 1.2 m this gives a Reynolds number Re_{imp} of 6×10^7.

Calculation of the Reynolds number that characterises the flow in the inlet requires another typical velocity. This can be either the ship speed or the pump speed (as defined in equation (2.11)). The actual choice is not so critical, since both values do not differ by more than a factor of two. In order to represent the flow phenomena inside the inlet best, the Reynolds number for the inlet is defined as:

$$Re_{inl} = \frac{\rho v_{pump} D_{inl}}{\mu} \tag{4.2}$$

For the same typical configuration as above, the Reynolds number Re_{inl} will be about 10^7, which is 6 times smaller than the impeller Reynolds number. Model scale experiments are performed at lower Reynolds numbers, as shown in table 3.1 on page 51. These values still exceed 5×10^5, which can be regarded as high Reynolds number flow. It is to be expected that, at least at design conditions, viscous effects play a limited role.

4.1.3 Time dependency

There are two different reasons for the flow to be time-dependent in a waterjet installation: (i) the non-uniformity of the flow at the impeller entrance results in a time varying onset flow of the rotating blades and (ii) the interaction between moving rotor and stationary stator blades at the impeller outlet is unsteady. In the rotating frame of reference, phenomena associated with the first reason have a frequency related to the shaft frequency. The frequency of the interaction phenomena between the rotor and stator blades depends on the number of stator blades and the shaft frequency.

In the stationary frame of reference the frequency of the fluctuations due to rotor-stator interaction is related to the number of impeller blades. The effect of the non-uniform inflow will give a steady component with superposed fluctuations with the blade passing frequencies.

4.1.4 Non-uniformity of impeller inflow

In chapter 3 the velocity distribution upstream of the impeller is discussed. It is shown that the velocity field is strongly non-uniform even at normal waterjet operating conditions. This velocity distribution has to be reproduced by the mathematical method in order to obtain a correct prediction of the inlet flow phenomena. For an analysis of the isolated pump, the non-uniform inflow to the impeller has to be implemented as an inflow boundary condition.

The development of the velocity distribution in the inlet is attributed to the ingestion of the boundary layer and to the deceleration of the flow. Generation of vorticity plays an important role in these flow phenomena. Application of a mathematical method based on the potential flow assumption or an inviscid flow model is therefore not suitable for the analysis of inlet flow phenomena.

Potential flow analyses of mixed-flow pumps have been made by Van Esch [2] and Van Os [3]. These calculations are based on a uniform inflow velocity distribution. Implementation of a non-uniform velocity distribution introduces velocity gradients for the axial velocity component. The constraint of irrotational flow results in additional velocity gradients in the directions perpendicular to the axial inflow direction. The cross components of the inflow velocity distribution have such a dominating influence on the overall development of the non-uniformity, that the velocity distribution is almost uniform within about one diameter pipe length. The analysis of the stability of the non-uniform velocity distribution is discussed in more detail in appendix A.

It is concluded that for the analysis of both a waterjet inlet as well as a pump with non-uniform inflow a suitable mathematical method should take the presence of vorticity into account.

4.1.5   Tip clearance flow

In general, waterjets are equipped with unshrouded mixed-flow or axial impellers. Unshrouded impellers have a small clearance between the blade tips and the stationary housing. This housing is called the seatring. The pressure difference between the pressure and suction side of the blade causes some leakage flow through the clearance. This leakage flow should be kept as low as possible to maintain a high efficiency of the pump. The distance between the impeller tip and the seatring is therefore very small, about 1-2% of the diameter. On the other hand, the velocity difference between the rotating blade tip and the stationary seatring can be about 50 m/s, which leads to large velocity gradients in the clearance.

As a result of the available pressure difference between pressure and suction side of the blade and the occurring viscous losses in the clearance a certain flow will establish. Effects of viscosity can not be neglected, if this flow is to be determined. Second effect of the viscosity is the development of boundary layers on the blade tip and the seatring. This is confirmed by Kunz et al. [4] in the investigation of tip clearance phenomena in an axial compressor cascade with an Euler and a Navier-Stokes method. It is found that the Navier-Stokes method shows better agreement with experimental data than the Euler method. Prediction of the tip clearance mass flow rate is presumed to be more accurate with the Navier-Stokes method.

The flow in a mixed-flow pump with various tip clearances has been analysed by Goto [5]. For this analysis he uses the unsteady Reynolds-averaged Navier-Stokes equations in a rotational frame of reference. Results of the calculations show reasonably good agreement with the experimental data. Moreover a variety of jet-wake flow patterns at the exit of the impeller are predicted well.

4.1.6   Final remarks

Based on the listed requirements and the capabilities of the different models, the choice for a viscous flow model is justified. In the next two chapters, results of a detailed validation study of numerical simulations for the waterjet inlet and the mixed-flow pump are presented. It is acknowledged that a viscous (i.e. RANS) flow method requires significantly more computational resources than an Euler method and certainly much more than a potential flow method.

Cavitation will not be taken into account in the analyses. Since cavitation models are presently developed for most commercial RANS codes, is it to be expected that application of methods with some form of cavitation model will be feasible in the near future.

The calculations presented in this study are carried out with the commercial CFD method Star-CD. This method is based on a finite volume numerical method. Both tetrahedral and hexahedral cell types can be used for the mesh. In this study all meshes are generated with hexahedral cells only.

4.2   Conservation laws

To describe the flow phenomena in a waterjet installation, two conservation laws are used. These are the laws for conservation of mass and that of momentum. Conservation of mass is also denoted as the continuity equation (see for example [6]):

$$\frac{\partial \rho}{\partial t} + \nabla \cdot \rho \underline{v} = 0 \tag{4.3}$$

where ρ is the density of the fluid and $\underline{v}$ the velocity.

In many cases the flow can be assumed to be incompressible. This is allowed, whenever variations in density are small. These variations in density are caused by variations in the pressure. Since in the present applications the velocities are much smaller than the speed of sound in the water, which is about 1450 m/s, the variation in density will be negligible. For an incompressible flow the continuity equation (4.3) reduces to:

$$\nabla \cdot \underline{v} = 0 \tag{4.4}$$

Conservation of momentum is given by (see also [6]):

$$\rho\frac{\partial}{\partial t}\underline{v} + \rho(\underline{v}\cdot\nabla)\underline{v} = -\nabla p + \mu\nabla^2\underline{v} + \frac{1}{3}\mu\nabla(\nabla\cdot\underline{v}) + \rho\underline{g} \tag{4.5}$$

where p is the pressure, μ is the dynamic viscosity, which is assumed to be constant in the derivation of equation (4.5) and $\underline{g}$ is the acceleration of gravity. This set of equations is known as the Navier-Stokes equation. For an incompressible flow, equation (4.4) can be substituted into equation (4.5). This results in the Navier-Stokes equation for incompressible flow:

$$\rho\frac{\partial}{\partial t}\underline{v} + \rho(\underline{v}\cdot\nabla)\underline{v} = -\nabla p + \mu\nabla^2\underline{v} + \rho\underline{g} \tag{4.6}$$

The Navier-Stokes equation can be solved numerically directly without further assumptions. This requires direct numerical simulations (DNS) to obtain the time-accurate solution of equations (4.4) and (4.6) on a grid that is sufficiently fine to resolve all flow details. Such a method is not suitable for practical engineering analyses, however. In the following section an approach will be discussed, which enables numerical solution of the flow field, within a practical context.

4.3   Reynolds Averaged Navier-Stokes (RANS) flow

In order to convert the Navier-Stokes equations into a set of equations, that can be solved numerically for general engineering applications, the concept of splitting the flow variables in a mean and a fluctuating part is employed. Substitution of this decomposition in the Navier-Stokes equation and time averaging the continuity and the Navier-Stokes equations, results in a set of equations for the mean-flow field variables. The concept of time averaging was introduced by Reynolds in 1895. The resulting equation is therefore called the Reynolds-averaged Navier-Stokes (RANS) equation.

4.3.1   Reynolds averaging

The principle of Reynolds averaging is based on a decomposition of the variables in a time averaged value and a fluctuating part:

$$v_i = \overline{v}_i + v_i' \tag{4.7}$$

The time averaged variable is defined as:

$$\bar{v}_i = \lim_{T \to t_1} \frac{1}{T} \int_t^{t+T} v_i dt \tag{4.8}$$

where t_1 has to be larger than the time scale of the smallest fluctuations. Therefore,

$$\bar{v}_i^* = \lim_{T \to t_1} \frac{1}{T} \int_t^{t+T} [v_i - \bar{v}_i] dt = 0 \tag{4.9}$$

The average of the fluctuating part is zero by definition. Nevertheless, if the product of two variables is considered, not all fluctuating terms vanish when they are correlated, thus:

$$\overline{v_i v_j} = \bar{v}_i \bar{v}_j + \overline{v_i' v_j'} \tag{4.10}$$

Substitution of the decomposed terms in the Navier-Stokes equation for the velocity and pressure and application of the method of Reynolds averaging gives:

$$\rho \frac{\partial}{\partial t} \underline{\bar{v}} + \rho (\underline{\bar{v}} \cdot \nabla) \underline{\bar{v}} = -\nabla p + \mu \nabla^2 \underline{\bar{v}} + \rho \underline{g} - \nabla \cdot \rho \overline{(\underline{v'} \underline{v'})} \tag{4.11}$$

The term $\rho \overline{(\underline{v'} \underline{v'})}$ is called the Reynolds stress term, where $\overline{(\underline{v'} \underline{v'})}$ is a diadic product defined by $\overline{(v'v')}_{ij} = \overline{v_i' v_j'}$. This tensor contains the correlations of the fluctuating terms of the velocity components. The term with the Reynolds stress can be treated in several ways. Boussinesq proposed a closure hypothesis for the Reynolds stress term. In index notation the closure is defined as:

$$-\rho \overline{v_i' v_j'} = \mu_T \left(\frac{\partial \bar{v}_i}{\partial x_j} + \frac{\partial \bar{v}_j}{\partial x_i} \right) - \frac{2}{3} \rho k \delta_{ij} \tag{4.12}$$

which is referred to as an eddy viscosity model with μ_T the turbulent or eddy viscosity and k the turbulent kinetic energy defined as:

$$k = \frac{1}{2} \overline{(v_i' v_i')} = \frac{1}{2} (\overline{v_x' v_x'} + \overline{v_y' v_y'} + \overline{v_z' v_z'}) \tag{4.13}$$

Turbulence models are used to obtain a value for the eddy viscosity. An alternative approach is to derive from the original time-dependent Navier-

Stokes equations a transport equation for each of the Reynolds stress components, however. These equations require another group of closure relations before the equations can be solved numerically. Such a model is called a Reynolds stress turbulence model.

Substitution of equation (4.12) into the Reynolds averaged Navier-Stokes equation (4.11) gives:

$$\rho\frac{\partial}{\partial t}\bar{\underline{v}} + \rho(\bar{\underline{v}}\cdot\nabla)\bar{\underline{v}} = -\nabla p + \nabla\cdot(\mu+\mu_T)(\nabla\bar{\underline{v}} + (\nabla\bar{\underline{v}})^T) + \rho\underline{g} - \nabla\frac{2}{3}\rho k \qquad (4.14)$$

The next step is the combination of the pressure term, the turbulent kinetic energy term and the gravitational term. The modified pressure is defined as:

$$p^* = p + \frac{2}{3}\rho k - \rho g z \qquad (4.15)$$

where it is assumed that gravity is directed in the z-direction. The resulting Navier-Stokes equation with the Reynolds stress terms included, becomes:

$$\rho\frac{\partial}{\partial t}\bar{\underline{v}} + \rho(\bar{\underline{v}}\cdot\nabla)\bar{\underline{v}} = -\nabla p^* + \nabla\cdot\mu_{eff}(\nabla\bar{\underline{v}} + (\nabla\bar{\underline{v}})^T) \qquad (4.16)$$

where the molecular viscosity μ and turbulent viscosity μ_T have been combined into the effective viscosity μ_{eff}.

4.3.2   Eddy viscosity turbulence models

Eddy viscosity turbulence models are used to determine a value for the eddy viscosity μ_T. Once this eddy viscosity is known, the Reynolds stresses are known and consequently the Reynolds-averaged Navier-Stokes equations can be solved. The available eddy viscosity turbulence models can be divided into 3 groups:

1. mixing length or algebraic models or zero-equation models
2. one-equation models
3. two-equation models

In a zero-equation model, the eddy viscosity μ_T is based on the mixing length concept. This mixing length is based on algebraic relations. The eddy viscosity for an algebraic model is defined as:

$$\mu_T = \rho l_{mix}^2\left|\frac{d\bar{v}}{dy}\right| \qquad (4.17)$$

where l_{mix} is Prandtl's mixing length.

The one-equation model uses a transport equation for the turbulent kinetic energy k and an algebraic relation for the mixing length scale. This model is thus an extension of the mixing length model. The eddy viscosity for a one-equation model is defined as:

$$\mu_T = \rho k^{1/2} l_{mix} \tag{4.18}$$

which uses a transport equation for k and an algebraic relation for the mixing length l_{mix}.

Two-equation models use a transport equation for both the turbulent energy k as well as the turbulent length scale or an equivalent. Two well-known examples are the dissipation ε for the k-ε model and the dissipation per unit turbulence kinetic energy ω for the k-ω model.

k-ε turbulence model

The eddy viscosity in the k-ε turbulence model is defined as:

$$\mu_T = \rho C_\mu \frac{k^2}{\varepsilon} \tag{4.19}$$

with C_μ a dimensionless constant. The standard k-ε turbulence model will be discussed in more detail. This model was first presented by Jones and Launder in 1972. The exact transport equation for the turbulent kinetic energy can be derived from the Navier-Stokes equation. The transport equation is given for example by Wilcox [7]:

$$\rho \frac{\partial k}{\partial t} + \rho v_j \frac{\partial k}{\partial x_j} = -\rho \overline{v_i' v_j'} \frac{\partial \bar{v}_i}{\partial x_j} + \frac{\partial}{\partial x_j} \left[\mu \frac{\partial k}{\partial x_j} - \frac{1}{2} \rho \overline{v_i' v_i' v_j'} - \overline{p' v_j'} \right] - \rho \varepsilon \tag{4.20}$$

where the terms on the right hand side represent production, diffusion and dissipation respectively. The diffusion term has three components; diffusion by viscosity, turbulent velocity fluctuations and pressure fluctuations. The latter two require a closure term in order to enable the transport equation to be solved. The turbulent transport and pressure diffusion terms are modelled by:

$$\frac{1}{2} \rho \overline{v_i' v_i' v_j'} + \overline{p' v_j'} = -\frac{\mu_T}{\sigma_k} \frac{\partial k}{\partial x_j} \tag{4.21}$$

where σ_k is a dimensionless closure coefficient.

The final transport equation for k becomes:

$$\rho\frac{\partial k}{\partial t} + \rho\bar{v}_j\frac{\partial k}{\partial x_j} = P_k + \frac{\partial}{\partial x_j}\left[\left(\mu + \frac{\mu_T}{\sigma_k}\right)\frac{\partial k}{\partial x_j}\right] - \rho\varepsilon \tag{4.22}$$

where the production term of the turbulent kinetic energy P_k is defined as:

$$P_k = -\rho\overline{v_i'v_j'}\frac{\partial\bar{v}_i}{\partial x_j} \tag{4.23}$$

The exact equation for the dissipation ε can be derived from the Navier-Stokes equation, but it requires a considerable amount of algebra to arrive at the final equation as given by Wilcox [7]. The exact equation for ε has a number of unknown double and triple products, so a number of closure terms are still required. The entire equation for ε can also be regarded as a model in a similar form as the transport equation for k (see [8]). The final equation becomes:

$$\rho\frac{\partial\varepsilon}{\partial t} + \rho\bar{v}_j\frac{\partial\varepsilon}{\partial x_j} = C_{\varepsilon1}P_k\frac{\varepsilon}{k} + \frac{\partial}{\partial x_j}\left[\left(\mu + \frac{\mu_T}{\sigma_\varepsilon}\right)\frac{\partial\varepsilon}{\partial x_j}\right] - C_{\varepsilon2}\rho\frac{\varepsilon^2}{k} \tag{4.24}$$

with dimensionless closure coefficients $C_{\varepsilon1}$, $C_{\varepsilon2}$ and σ_ε. Similar to equation (4.22) a production, diffusion and dissipation term can be recognized on the right-hand-side.

The k-ε turbulence model contains five closure coefficients. The values for the coefficients of the k-ε turbulence model, as used in the CFD method employed in the present study, are listed in the table below. These values are found in the manual [9].

Table 4.1   Values for k-ε turbulence model closure coefficients

C_μ	$C_{\varepsilon1}$	$C_{\varepsilon2}$	σ_k	σ_ε
0.09	1.44	1.92	1.0	1.22

A value of 1.3 for the constant σ_ε can be found in literature as well ([7], [10]).

k-ω turbulence model

The k-ω turbulence model has a similar set of equations as the k-ε turbulence model. The k-ω model uses the dissipation per unit turbulence kinetic energy ω, whereas the dissipation ε is used in the latter. The basis of the k-ω model was postulated by Kolmogorov. Further development of this model has led to

the following set of equations. The eddy viscosity hypothesis for the k-ω turbulence model is defined as:

$$\mu_T = \rho \frac{k}{\omega} \tag{4.25}$$

The equation for the turbulent kinetic energy is similar to equation (4.22) except for the dissipation term and the closure coefficients:

$$\rho \frac{\partial k}{\partial t} + \rho \bar{v}_j \frac{\partial k}{\partial x_j} = P_k + \frac{\partial}{\partial x_j} \left[(\mu + \sigma^* \mu_T) \frac{\partial k}{\partial x_j} \right] - \beta^* \rho k \omega \tag{4.26}$$

with the production term P_k according to equation (4.23) and the closure coefficients β^* and σ^*. The transport equation for the dissipation per unit turbulence kinetic energy ω is also adapted in a similar way, as shown by Wilcox [7]:

$$\rho \frac{\partial \omega}{\partial t} + \rho \bar{v}_j \frac{\partial \omega}{\partial x_j} = \alpha P_k \frac{\omega}{k} + \frac{\partial}{\partial x_j} \left[(\mu + \sigma \mu_T) \frac{\partial \omega}{\partial x_j} \right] - \beta \rho \omega^2 \tag{4.27}$$

where α, β and σ are three more closure coefficients. The values for all five closure coefficients of the k-ω turbulence model are shown in table 4.2

Table 4.2   Values for k-ω turbulence model closure coefficients

α	β	β^*	σ	σ^*
5/9	3/40	9/100	1/2	1/2

Wall functions

Use of one of the many available high Reynolds turbulence models implies the application of wall functions to replace the no-slip boundary condition. The wall functions employ special algebraic formulas for the representation of the distribution of the velocity and turbulence within the part of the boundary layer closest to the wall. This is necessary to relax the requirement of grid resolution in the boundary layer. The dimensionless distance from the wall to the cell centre of the first cell is generally denoted as y^+ and is, according to [10], defined as:

$$y^+ = \frac{\Delta y_p}{\nu} \cdot \sqrt{\frac{\tau_w}{\rho}} = \frac{\Delta y_p u_\tau}{\nu} \tag{4.28}$$

where $u_\tau = \sqrt{\tau_w / \rho}$ and Δy_p is the distance from the wall to the near wall cell centre. Note that the dimensionless distance y^+ is a kind of Reynolds number,

based on the distance from the wall and the velocity near to the wall to the power 1/2. For accurate application of the wall function the y^+ value should be in the range of 30 to 100, according to the manual [9]. For y^+ values smaller than y_m^+ the dimensionless velocity u^+ is calculated from:

$$u^+ = y^+ \tag{4.29}$$

For y^+ values larger than y_m^+, the u^+ is calculated from:

$$u^+ = \frac{1}{\kappa} ln(Ey^+) \tag{4.30}$$

where y_m^+ satisfies the equation:

$$y_m^+ - \frac{1}{\kappa} ln(Ey_m^+) = 0 \tag{4.31}$$

with κ the von Kármán constant and an empirical constant E.

The dimensionless velocity u^+ is defined as:

$$u^+ = \frac{(u - u_w)}{u_\tau} = \frac{(u - u_w)}{\sqrt{\frac{\tau_w}{\rho}}} \tag{4.32}$$

where u is the tangential fluid velocity and u_w the velocity of the wall. The empirical constants of equation (4.30) can be coupled to the universal logarithmic velocity distribution, known also as log-law [11]:

$$u^+ = \frac{1}{\kappa} ln(y^+) + C \tag{4.33}$$

with κ the von Kármán constant equal to 0.4187 and C a constant with a value between 4.9 and 5.5 ([12]). The default value for the empirical constant E in the CFD method used is 9.0. This results in a value for C of 5.25.

The definition of y^+ according to equation (4.28) will lead to numerical problems at points where the flow is about to separate. At such locations the wall shear stress τ_w becomes zero, which results in an y^+ of zero. This is solved with the modified definition for y^+ based on the turbulent kinetic energy k:

$$y^+ = \frac{\rho \Delta y_p}{\mu} \cdot C_\mu^{1/4} \sqrt{k} \tag{4.34}$$

It is assumed that there will always be turbulent fluctuations at a flow separation point, which eliminates the problem.

4.4   Two-dimensional test cases

In order to get an indication of the obtainable accuracy of both the mathematical and the numerical methods, the flow around a number of well known NACA profiles has been analysed. The flow along isolated profiles as well as profiles in a cascade have been calculated. For all configurations experimental data for the lift and drag is available.

4.4.1   Isolated NACA 0012 profile

The mesh for the numerical analysis of the flow along the NACA 0012 profile is shown in figure 4.1. The chord length of the profile is 600 mm. The domain is divided in three subregions. The first region is meshed with an O-grid around the profile. This gives good control of the quality of the boundary layer cells along the surface. A rectangular box is placed around the first region to make a transition from the O-grid to an H-grid. In this second region also an O-grid type of mesh is applied.

The third domain extends the numerical domain to either the tunnel walls in the experiments or to a distance to impose the far-field boundary conditions. At the interface between the second and third domain an arbitrary coupling method is employed, which allows non-matching cells at both sides of the interface.

The O-grid region closest to the profile surface can not be recognised well in the mesh plot due to the large number of mesh lines. The other two regions can be distinguished more clearly. In this approach the mesh around the profiles is identical for all calculated conditions. Regions 1 and 2 can be rotated to obtain the desired angle of attack for the profile.

Mesh dependency studies have been carried out to evaluate the variation in lift and drag prediction for an angle of attack of 4 degrees. The number of cells around the profile and in the direction perpendicular to the profile have been varied. The number of cells in the O-grid around the profile has been varied from 150 to 330 cells. In the normal direction the number of cells is increased from 32 to 48. The number of cell in normal direction in the first region is kept constant to keep a constant y^+ value of about 110. This is in accordance with the requirements for the use of the wall functions.

At the upper and lower boundary of the domain two types of boundary conditions can be applied: (i) wall boundary conditions or (ii) constant pressure boundary conditions. The first type can be used if the experimental data is obtained from wind tunnel tests. The second type is suitable for an unbounded region. For sufficiently large numerical domains both types will
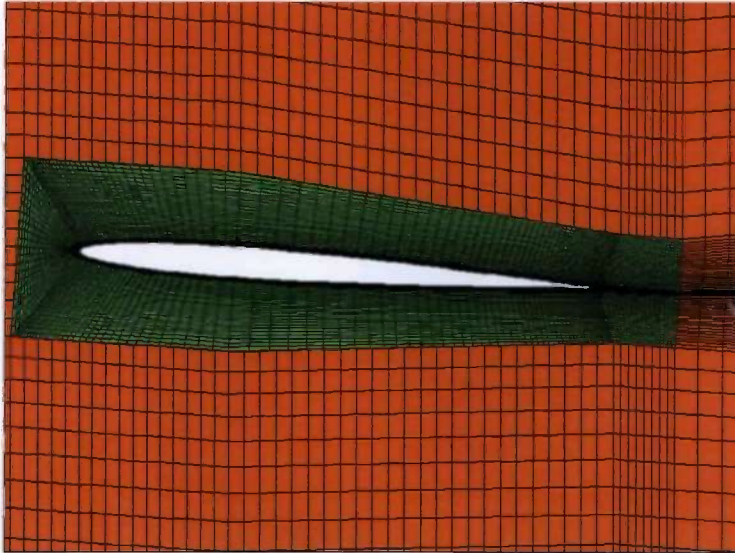
Figure 4.1   Plot of a part of the mesh as used in calculations of isolated NACA 0012 profile.

give comparable results. At the inlet boundary a uniform velocity distribution of 10 m/s is prescribed and the constant density of water is used. The

Reynolds number for the calculations becomes $6 \cdot 10^6$. Turbulence intensity is set to 0.01% and the length scale is set to a small fraction of the tunnel height. All calculations have been carried out with the standard k-ε turbulence model and employing wall functions. Solution is based on a second order MARS (= Monotone Advection and Reconstruction Scheme) discretisation scheme for the momentum equations. This second order method is least sensitive to the mesh structure and skewness [9]. The k-ε model turbulence equations are discretised with a first order upwind differencing scheme.

Convergence behaviour of one of the calculated conditions is shown in figure 4.2. The convergence criterion for all calculations is set to 10^{-4} for the momentum, mass and turbulent kinetic energy equations.
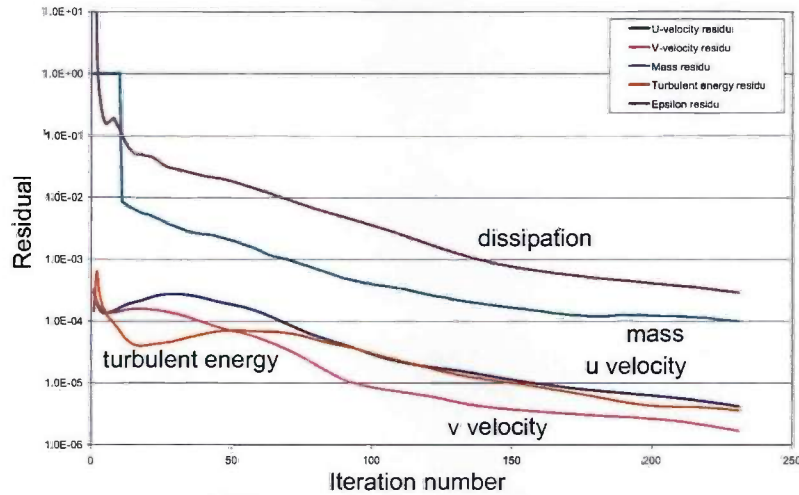
Figure 4.2   *Plot of convergence of a calculation of NACA 0012 profile at angle of attack of 4 degrees for mesh with 222 cells around profile and 40 cells in normal direction.*

Figure 4.3 shows a comparison of the calculated and measured lift and drag for the isolated NACA 0012 profiles. The experimental data is taken from Abbott & von Doenhoff [13], where the results of the measurements with smooth profiles at a Reynolds number of $6 \cdot 10^6$ are used. Compressibility has been negligible for the tested conditions.

The numerical values for lift and drag are based on the integrated pressure and shear forces acting on the profile surface. The dimensionless lift and drag coefficients are defined as:

$$c_l = \frac{L}{\frac{1}{2}\rho v^2 A} \tag{4.35}$$

$$c_d = \frac{D}{\frac{1}{2}\rho v^2 A} \tag{4.36}$$

where ρ is the density, v the free-stream velocity and A the surface area of the wing, i.e. here the chord length times the width in span wise direction. L is the lift force and D the drag force.

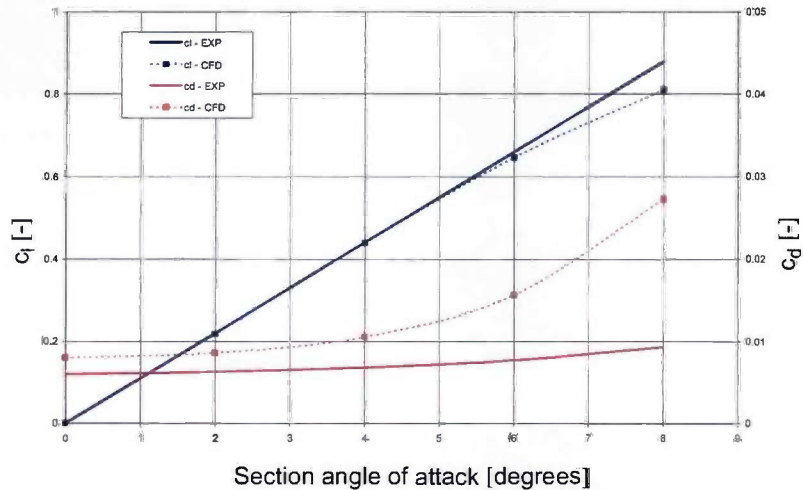Section angle of attack [degrees]

Figure 4.3   *Comparison of measured and calculated lift an drag for NACA 0012 profile. Reynolds number of experiments and calculations is $6.0x10^6$. Mesh is based on 222 cells around profile and 32 in normal direction*

Agreement is good for the lift up to an angle of attack of about 6 degrees. The comparison of calculated and measured drag shows a clear over-prediction. The relative error increases from 33% at 0 degrees angle of attack to 55% at an angle of attack of 4 degrees. The deviation between the measurements and the calculations continuously increases with larger angles of attack.

The results of the mesh sensitivity study are shown in table 4.3 for the lift prediction and in table 4.4 for the drag prediction at an angle of attack of 4 degrees. The relative difference in lift coefficient between the minimum and maximum lift is about 3%. For the drag coefficient a variation of about 9% is found. The results of the finer meshes do not show a reduction of the deviation with the experimental data. The error in prediction of drag might be related to an error in the production term of the turbulence model at the stagnation point, as described by Moore & Moore [14].

Table 4.3   Lift coefficient for mesh convergence study. Columns
             show number of cells in normal direction and rows show
             cells in O-grid around the profile

c_l [-]	32 cells	40 cells	48 cells
150 cells	0.4418	0.4386	0.4407
222 cells	0.4384	0.4375	0.4366
330 cells	0.4291	0.4289	0.4302

Table 4.4   Drag coefficient for mesh convergence study. Columns
             show number of cells in normal direction and rows show
             cells in O-grid around the profile

c_d [-]	32 cells	40 cells	48 cells
150 cells	0.010754	0.011324	0.011493
222 cells	0.010522	0.010988	0.011332
330 cells	0.010784	0.011243	0.011495

The sensitivity of the turbulence model is evaluated by a variation of the
turbulence intensity of the free stream flow at the inlet boundary condition.
Calculations are carried out with a mesh with 222 cells around the profile and
32 in normal direction. The level of the turbulence intensity at the inlet
boundary condition is increased from 0.01% to 1.0%. The results for the
prediction of lift and drag coefficient are presented in table 4.5. Variation in lift
coefficient is 4%, whereas the change in drag is about 42%.

Table 4.5   Lift and drag coefficients for calculations with variation of
             input values for turbulence intensity

Turbulence intensity [%]	c_l [-]	c_d [-]
0.01 %	0.4384	0.010522
0.10 %	0.4287	0.012713
0.50 %	0.4242	0.014147
1.00 %	0.4206	0.014980

The test calculations with the NACA 0012 profile show that the error in
prediction of profile drag remains after some mesh refinement steps.
Moreover the deviation between experimental data and calculations
increases significantly when the level of turbulence intensity at the inlet
boundary increases. It should be noted that the low turbulence levels as used
in the experiments are not representative for the inflow to the waterjet pump.

It is concluded that with the currently used cell sizes, which is comparable with the sizes to be used in the three dimensional pump mesh, a significant deviation between calculated and measured profile drag will remain.

4.4.2   Cascades with NACA 65-410 profiles

Apart from calculations on isolated profiles, also the flow around profiles in a cascade have been analysed. Extensive experimental data is available on tests with NACA 65 compressor blade profiles [15]. Data were reported for NACA 65 profiles with various camber lines and a maximum thickness of 10% of the chord. Cascades of profiles can be described with two additional parameters. These are the solidity and the blade angle. The solidity is a measure for the distance between two profiles in relation to the chord length. The blade angle is defined as the angle between the profile base line and the line connecting all leading edges. An example of the cascade is shown in figure 4.4.Calculations have been carried out for a NACA 65 410 profile with a blade angle of 20 degrees and a solidity of 1.0 and 1.5. The designation of the profile is based on a design lift coefficient of 0.4 and a maximum thickness of 10%. The basic camber line used is the a =1.0 mean line (see for example [13]).

The mesh is created in a similar way as for the isolated NACA 0012 profile. Periodic boundaries are applied to simulate a cascade with an infinite number of profiles. Turbulence model, discretisation scheme and convergence criteria are identical to the calculations for the NACA 0012 profile.
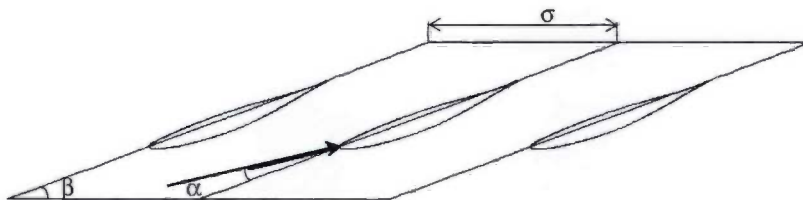

Figure 4.4   Geometry of NACA 65-410 cascade. Cascade solidity σ = 1.0, blade angle β = 20 degrees.

Figure 4.5 shows the non-dimensional pressure distribution C_p for the cascade with a solidity of 1.0 and a blade angle of 20 degree. The dimensionless pressure C_p coefficient is defined as:

$$C_p = \frac{p - p_\infty}{\frac{1}{2}\rho v_\infty^2} \tag{4.37}$$

where p is the static pressure, p_∞ the reference pressure, ρ the density and v_∞ the free-stream velocity.

The angle of attack varies from 0.5 to 12.5 degrees. Agreement between calculations and measurements is acceptable for most pressure taps for the different conditions.

Lift and drag are derived from the CFD results in the same manner as for the NACA 0012 profile. These results are compared with the experimental data in figure 4.6. The lift is predicted quite well for most conditions. The deviations
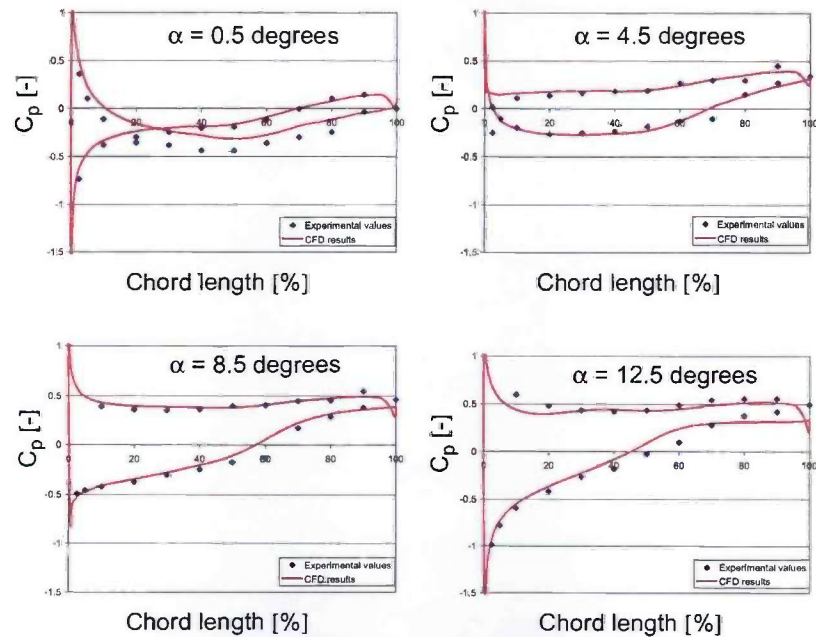
Figure 4.5   Pressure coefficient distribution along surface of NACA 65_410 profile for different angles of attack. Cascade solidity = 1.0, blade angle = 20 degrees.
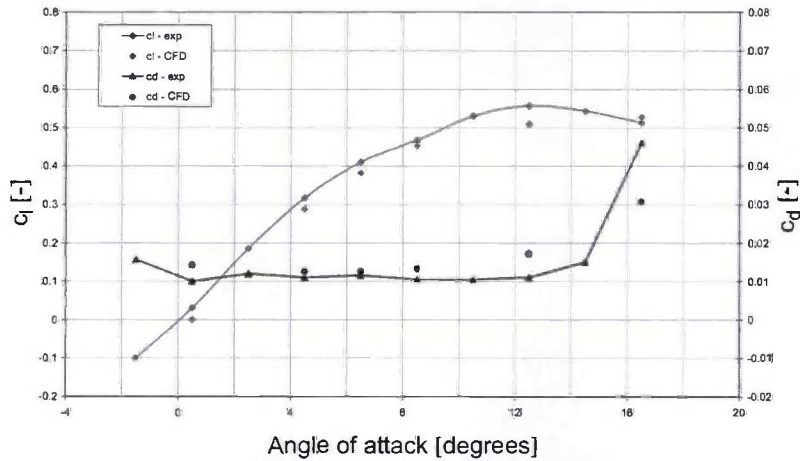
Figure 4.6   *Comparison of measured and calculated lift and drag for NACA 65_410 profiles in cascade with solidity of 1.0 and blade angle of 20 degrees.*

between the measured and calculated drag vary between about 10% and 50%. This is in agreement with the results of the isolated NACA 0012 profile.

It can be concluded that the trend of over-prediction of drag occurs for both isolated profiles as well as for profiles in a cascade. In both cases the lift is predicted much better. In the next subsection the consequences of an error in lift or drag on the prediction of thrust and torque are discussed.

4.4.3   Sensitivity of errors in drag on thrust and torque

Torque and thrust of a waterjet impeller are related to the tangential and axial force experienced by the blade sections. These forces can be derived from the lift and drag of these profiles. Consequently, if the blade profile drag is over-predicted, there will be an effect on the prediction of the torque and the thrust. Lift and drag are transformed into axial and tangential forces with:

$$F_{ax} = \cos\phi \cdot L - \sin\phi \cdot D$$
$$F_{tan} = \sin\phi \cdot L + \cos\phi \cdot D$$

$$\text{(4.38)}$$

where ϕ is the inflow angle, L the lift force and D the drag force. The inflow angle ϕ is related to the blade angle β and the angle of attack α of the flow with respect to the chord line:

$$\phi = \beta - \alpha$$

$$\text{(4.39)}$$

The drag prediction based on CFD calculations can be expressed as:

$$D_{CFD} = D_{exact}(1 + \varepsilon) \tag{4.40}$$

where ε represents the relative over-prediction of the profile drag. It is assumed that:

$$L_{CFD} = L_{exact} \tag{4.41}$$

This can be up to about 50%. Figure 4.7 shows a sketch of the forces acting on a profile. From this sketch the effect of a higher drag can already be recognised.
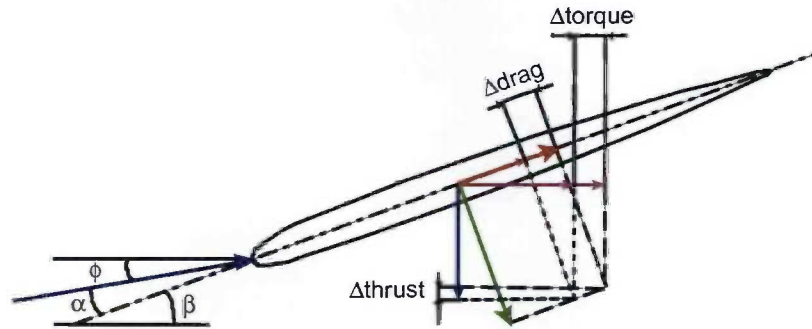

Figure 4.7   Sketch of forces acting on profile

Substitution of equation (4.40) in equation (4.38) gives an expression for the axial and tangential force prediction based on CFD results. These forces can be related to the exact solutions to determine the resulting relative error in axial and tangential direction. The relative error for the axial force can be calculated with:

$$\frac{F_{ax\_CFD}}{F_{ax\_exact}} = 1 - \frac{\varepsilon}{\dfrac{1}{\tan\phi} \cdot \dfrac{L_{exact}}{D_{exact}} - 1} \tag{4.42}$$

where ϕ is the inflow angle, L/D is the lift over drag ratio. The relative error in tangential direction yields:

$$\frac{F_{tan\_CFD}}{F_{tan\_exact}} = 1 + \frac{\varepsilon}{\tan\phi \cdot \dfrac{L_{exact}}{D_{exact}} + 1} \tag{4.43}$$

To get an indication of the influence of the error in drag prediction on the axial and tangential force, the data for the NACA 65-410 cascade will be used. The lift over drag ratio as function of the angle of attack is derived from figure 4.6. The relative errors in axial and tangential force are plotted as function of the angle of attack in figure 4.8. The drag over-prediction is set to 20%, 40% and 60%.

From this diagram is becomes clear that the effect on axial force is very small even for large over-prediction of drag. The estimated error on thrust will be less than 1% for most cases. On the other hand the error in tangential force remains significant for realistic values of the angle of attack α and drag error factor ε. The error in tangential force can be about 2.0 to 8.0%. For cascades with smaller blade angles β, the error in tangential force will increase even more.

It is to be expected that this effect will be noticeable in both impeller and propeller torque calculations. Calculation of thrust seems to be insensitive to an error in drag. It is expected that the calculation of pump head shows the same behaviour, based on the similarity between propeller thrust and pump head as shown in equation (2.34).
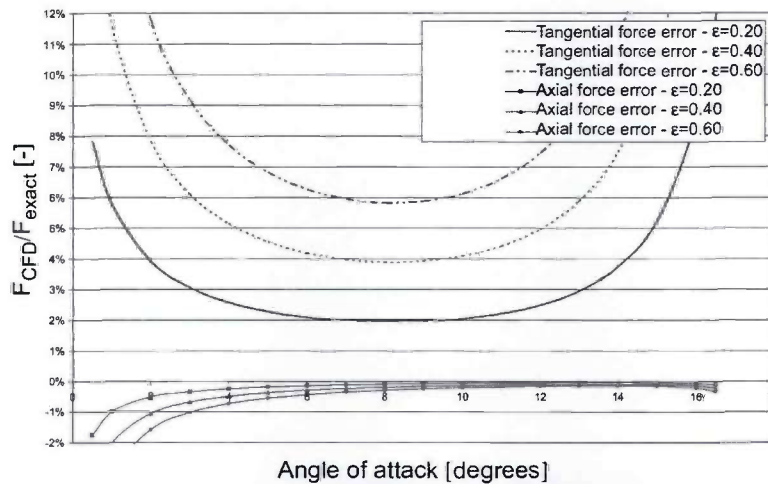

Angle of attack [degrees]

Figure 4.8   Relative errors in tangential and axial forces due to over-prediction of profile drag. Data is based on NACA 65-410 cascade with solidity of 1.0 and blade angle of 20 degrees.

4.5 Nomenclature

A	area	m^2
c_d	drag coefficient	-
c_l	lift coefficient	-
C_p	pressure coefficient	-
D	drag	N
F	force	N
g	gravitational acceleration	m/s^2
k	turbulent kinetic energy	m^2/s^2
L	lift force	N
l_{mix}	Prandtl's mixing length	m
P	production term of turbulence	m^3/s^2
p	pressure	N/m^2
Re	Reynolds number	-
t	time	s
u^+	dimensionless velocity	-
v	velocity	m/s
Δy_p	distance from wall	m
y^+	dimensionless wall distance	-
z	coordinate in vertical direction	m

Greek symbols

α	angle of attack	degrees
β	blade angle	degrees
ε	dissipation	m^2/s^3
ε	relative error in drag prediction	-
ϕ	inflow angle	degrees
κ	Von Kármán constant	-
μ	dynamic viscosity	kg/ms
ρ	fluid density	kg/m^3
τ_w	wall shear stress	N/m^2
ω	vorticity, dissipation rate	1/s

Subscripts

ax	axial direction

CFD	based on CFD results
eff	effective (=laminar + turbulent)
exact	based on exact formulations
i,j	directions
imp	impeller
inl	inlet
T	turbulent
tan	tangential direction
tip	impeller blade tip
w	wall
x,y,z	carthesian coordinate system directions

Superscripts

| v' | fluctuating part |
| $\bar{v}$ | time averaged value |

4.6   References

[1] Aungier, R.H.,'Centrifugal compressors', ASME Press, New York, 2000

[2] Van Esch, B.P.M.,'Simulation of three-dimensional unsteady flow in hydraulic pumps', PhD thesis, University of Twente, 1997

[3] Van Os, M.J.,'On the flow and cavitation inception of mixed-flow impellers', PhD thesis, University of Twente, 1998

[4] Kunz, R.F., Lakshminarayana, B., Basson, A.H., 'Investigation of tip clearance phenomena in an axial compressor cascade using Euler and Navier-Stokes procedures', Journal of Turbomachinery, Vol 115, pp 453-467, 1993

[5] Goto, A.,'Study of internal flows in a mixed-flow pump impeller at various tip clearances using three-dimensional viscous flow computations', Journal of Turbomachinery, Vol 114, pp 373-382, 1992

[6] Fox, R.W., McDonald, A.T.,'Introduction to fluid mechanics', Third Edition, John Wiley & Sons, New York, 1985

[7] Wilcox, D.C.,'Turbulence modeling for CFD', Griffin Printing, Glendale, 1993

[8] Ferziger, J.H., Peric, M., 'Computational methods for fluid dynamics', Second edition, Springer, Berlin, 1999

[9] Computational Dynamics Limited, 'Star-CD methodology, version 3.150", 2001

[10] Versteeg, H.K., Malalasekera, W., 'An introduction to Computational Fluid Dynamics', Longman Scientific & Technical, Essex, 1995

[11] Schlichting, H., 'Boundary layer theory', McGraw-Hill, New York, 1968

[12] Cebeci, T., Smith, A.M.O., 'Analysis of turbulent boundary layers', Academic press, New York, 1974

[13] Abbott, I.H., Von Doenhoff, A.E. ,'Theory of wing sections', Dover Publications, Inc., New York, 1958

[14] Moore, J.G., Moore, J., 'Controlling over-production of turbulence in two-equation models by limiting the anisotropy of the Reynolds normal stresses', 1997 ASME Fluids Engineering Division Summer Meeting, 1997

[15] Emery, J.C., Herrig, L.J., Erwin, J.R., Felix, A.R., 'Systematic two-dimensional cascade tests of NACA 65-series compressor blades at low speeds', NACA report 1368, Langley Aeronautical Laboratory, Langley Field, 1958

Chapter 5   Numerical analysis of waterjet inlet flow

In this chapter the flow through the waterjet inlet will be analysed in more detail. First a critical review of several published analyses of the flow through waterjet inlets will be given, which provides additional information about the suitable numerical approach for the inlet flow CFD analysis. Discussion of the application of the numerical method is divided into two parts: (i) the mesh generation for the three dimensional inlet geometry based on the experimental set-up for the finite volume analysis and (ii) the selection of boundary conditions. In order to validate the computational method the CFD results are compared with experimental data for a model scale waterjet inlet duct. During the validation process, the effects of the confinement of the flow due to the cavitation tunnel walls are also addressed.

The CFD results can be used to visualise the flow behaviour in more detail. Besides pressure and velocity distribution, it is also interesting to quantify wall friction and to determine the shape of the dividing streamtube.

5.1   Review of CFD analyses on waterjet inlets

Calculations for a three dimensional waterjet inlet have been reported by Førde et al. [1]. For the calculations an Euler method was employed, but computed results were not validated with measurements. The presented velocity distribution at the impeller plane is not in agreement with a typical flush type waterjet inlet. This is caused by the neglect of the boundary layer velocity profile at the inlet and absence of viscous effects in the method,

necessary for describing the development of the boundary layer in the inlet duct.

A potential flow method has been applied by Van Terwisga [2]. Comparison of the calculated pressure distribution along the ramp and the cutwater (or inlet lip) with experimental data shows large deviations. This is due to the neglect of viscous losses and due to small deviations in the calculated velocity field near the stagnation point at the cutwater. A small deviation of the angle of attack at the cutwater can lead to relatively large differences in the prediction of the static pressure distribution.

Pylkkänen ([3], [4]) presented results of CFD calculations obtained from a RANS code. A two-dimensional model of a waterjet inlet is used for these analyses. Differences between calculations and measurements of pressure are about 11 to 15%. The experimental data is based on measurements of a three-dimensional inlet on a windtunnel. It is known that an actual three-dimensional waterjet inlet ingests water from a region that is wider than the inlet itself. In a two-dimensional situation this phenomenon cannot be reproduced, and therefore the pressure distribution at the lip section will be different. In the second part of the inlet, the rectangular cross-section transitions to a circular cross-section in general. This transition is not taken into account in a two-dimensional analysis either. Therefore it is expected that the pressure distribution in this part of the inlet will show a deviation from the three-dimensional case as well.

The necessity of considering the three-dimensional geometry is shown by Van der Vorst et al. [5]. Calculations were made for a two and for a three-dimensional case. Results of both calculations were compared with experimental data. The calculated pressure distribution along the inlet ramp centre line shows agreement with the measurements for the three-dimensional analysis, whereas large deviations are found for the results of the calculations of the two-dimensional geometry. The pressure measurements were performed for a model scale waterjet inlet, mounted on top of a windtunnel.

Another example of the use of viscous methods for the calculation of three-dimensional inlet flows was reported by Seil et al. [6]. In these calculations, the geometry of the pump is included. The effect of the impeller is modelled with an actuator disk, however. Calculated results show that the location of the stagnation point at the cutwater depends on the IVR value. It is also found that the level of non-uniformity of the velocity profile at the bend increases with increasing IVR. This non-uniformity vanishes towards the impeller plane, where the actuator disk is located. This behaviour may be a result of the implementation of the actuator disk. Yang et al. [7] have also calculated the flow around a waterjet inlet with a viscous flow method. A complete hull is included in the computational domain. Agreement between measurements and CFD results is poor for the pressure distribution along the ramp and lip centre lines.

Experimental data from windtunnel tests has been used for comparison with calculations of the viscous flow through a three-dimensional inlet geometry [8]. Agreement between measurements and calculations is good for the static pressure distribution along the ramp for a range of IVR values. Moreover, the typical non-uniform velocity distribution in the impeller plane is reproduced well for the conditions considered. A comparison between the calculated and measured velocity distribution is shown for an IVR of 1.59.

Hu and Zangeneh [9], [10] have presented an optimization algorithm for waterjet inlet geometries. This method optimizes the two-dimensional symmetry-plane geometry of the inlet, which is then extended in the third direction. Both the two-dimensional as well as the three-dimensional geometries are analysed using a viscous flow method.

The development described above has resulted in a widespread use of three-dimensional viscous flow calculations for the analysis of the flow phenomena in waterjet inlets. However, these calculations are not always validated with measurements of static pressure and velocity.

Validation of the CFD method requires an accurate set of experimental data. This data can be obtained from cavitation tunnel experiments, for example. In a test set-up with an inlet mounted on top of a cavitation tunnel, all governing parameters of the operating condition can be measured accurately. If a wind tunnel is used for measurements instead of a cavitation tunnel, the air density has to be monitored simultaneously in order to be able to determine the flow rate accurately. Relatively small variations in flow rate will result in a deviation of the IVR. Another important aspect in the experimental set-up is the capability to create an incoming hull boundary layer of sufficient thickness, in accordance with normal waterjet applications. Accurate measurements of the static pressure at the ramp and the velocity distribution at the impeller plane were obtained in the Tom Fink cavitation tunnel [11]. These measurements are used for validation purposes in this chapter.

Measurements on actual waterjet installations can provide validation data as well. Some typical problems of model scale testing, like Reynolds scaling effects, artificial boundary layer thickening and confinement of the flow by tunnel walls are eliminated in these measurements. On the other hand, it is very difficult to determine the exact operating conditions of the waterjet installation. This limits the use of measurement data obtained from full scale waterjet installations.

5.2   Geometry and mesh generation

The analysis presented in this chapter is based on the geometry of the inlet as used in the experimental set-up, as described in subsection 3.1.1. The calculations are carried out to reproduce the flow phenomena of the measured conditions.
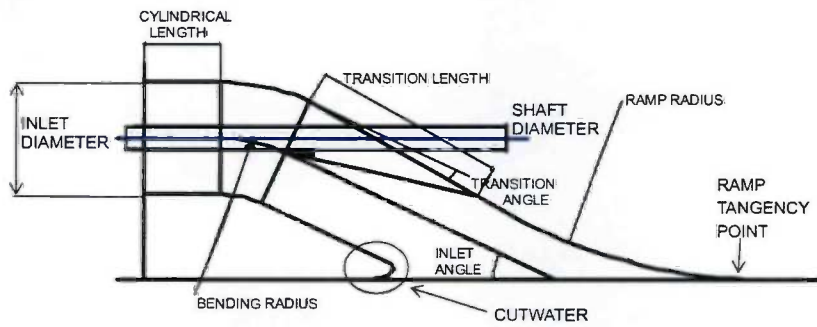
Figure 5.1   Inlet geometry with main parameters and specific nomenclature listed

The geometry of a waterjet inlet duct can be described by a number of parameters, e.g. the pump inlet diameter, the inlet angle, the radius of curvature of the bend and the shape of the cutwater. It is therefore convenient to develop a fully parametric three-dimensional geometry and mesh generator, based on a list of geometric parameters. Figure 5.1 shows a sketch of a two-dimensional inlet geometry with the main parameters. Based on the geometric parameters the three-dimensional shape of the inlet is calculated. This geometrical data is used in the CFD pre-processor. From this input data the block definitions are created. The topology of the blocks is kept identical for all waterjet inlets. Figure 5.2 shows a typical output of the used block structure. A thin layer of cells is created at the walls of the inlet, in order
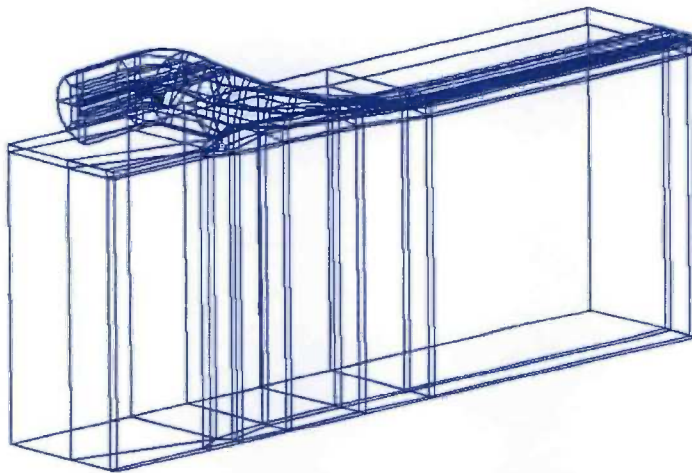
Figure 5.2   Wire frame plot of block structure of the inlet mesh
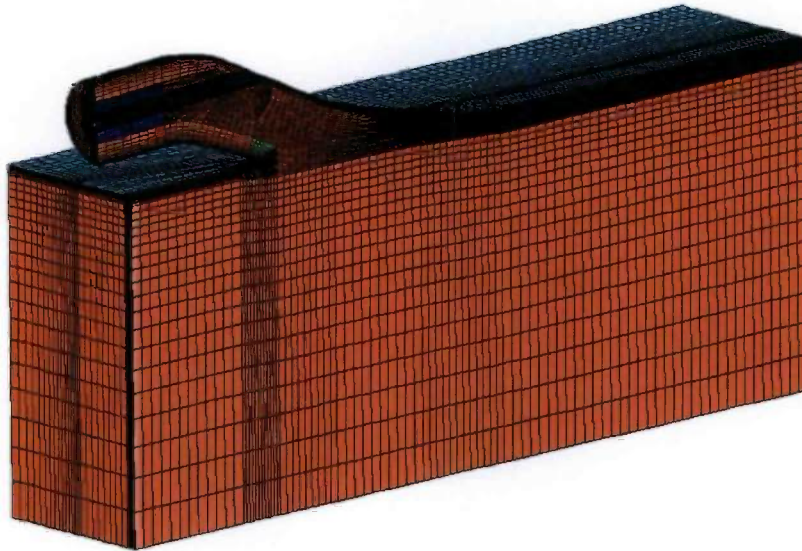
Figure 5.3a   Final mesh of waterjet inlet (half of the complete domain)
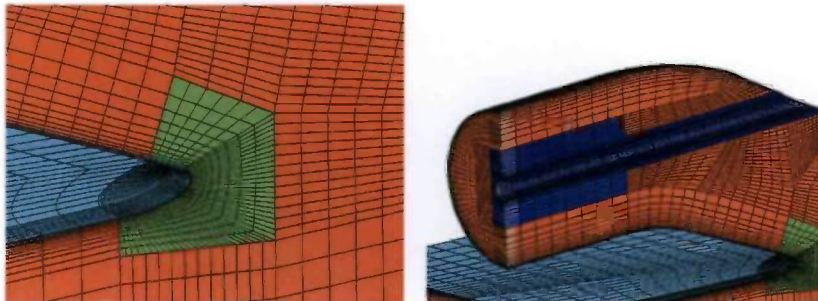
*Figure 5.3b   Detail of cutwater mesh with local refinement and regular mesh
coupling on the block boundaries (left) and mesh around the
(stationary) shaft*

to get high quality cells in the boundary layer. The averaged y^+ value of the cells near the wall is about 60 for this mesh.

Near the so-called cutwater (or inlet lip), a local refinement of the mesh is applied to capture the gradients of the flow field better. The final mesh is shown in figure 5.3a and in figure 5.3b a detail of the cutwater with local refinement and the region around the shaft is shown. In case of computations

with a stationary shaft or without a shaft, the computational domain is restricted to half the geometry for reasons of symmetry with respect to the vertical plane through the centreline of the pump.

5.3 Numerical approach

5.3.1 Boundary conditions

All cell faces at the boundary of the computational domain require some type of boundary condition.

At the inlet of the computational domain an inlet type boundary condition is applied. This type of boundary condition requires a prescription of the velocities in all three directions and values for the turbulence intensity and the length scale, if a turbulence model is used. The velocity profile, which represents the hull boundary layer, is input through a user-routine. In this routine a power-law velocity profile is calculated for all cells that are located in the boundary layer. The presented calculations are based on a boundary layer profile with a power-law value n=7 and a thickness δ of $0.3D$, with D the diameter of the inlet. An undisturbed uniform velocity is prescribed in the remainder of the cells. The turbulence intensity is set to 2.0% and the length scale to 0.05 m, which is equivalent to about 8% of the tunnel inlet hydraulic diameter.

At the impeller plane the total mass flow leaving the domain through the inlet duct is imposed. This is established with a fixed flow outlet boundary condition. This type of condition allows for a non-uniform velocity distribution over the surface. The pressure distribution in the outflow plane is part of the solution as well.

For the outflow plane of the cavitation tunnel a constant pressure boundary condition is used. It is assumed that the static pressure is uniform at large enough distance from the waterjet inlet. The resulting velocity distribution will be non-uniform, however.

The side plane and the bottom plane of the domain are placed at the location of the cavitation tunnel walls. For these walls, the slip condition is applied as the wall boundary condition. The mesh near these walls can be made relatively coarse, since the boundary layer is not resolved. With this boundary condition the normal velocity is set to zero, which simulates the effect of the wall on the flow. The effects of the development of the natural tunnel wall boundary layer, characterised by the displacement and momentum thickness, are neglected. The effects of the actual boundary layer in the cavitation tunnel are analysed during the tests and it is concluded that the effect of blockage was less than 0.2%.

For conventional waterjet inlet CFD analyses the tunnel walls are not taken into account. The side and bottom planes of the domain are modelled as

constant pressure planes. Using pressure boundary conditions, additional inflow of water is allowed. The difference between wall boundary conditions and constant pressure boundary conditions is investigated later on in this thesis.

Calculations for a half model geometry require symmetry conditions at the symmetry plane. If the complete model is analysed with shaft rotation, an additional wall boundary condition is applied to the shaft surface in order to model the rotation.

5.3.2   Fluid properties

Selection of the fluid properties for the waterjet inlet analysis is straightforward. As discussed in the previous chapter, the flow can be considered as incompressible, which results in a constant density. All model scale calculations have been carried out with a density ρ of 1000 kg/m^3. The dynamic fluid viscosity μ is set to 0.001 kg/ms.

Turbulent flow behaviour is modelled with a turbulence model. Though the CFD method provides several different turbulence models with different levels of complexity, the well established high-Reynolds number flow k-ε turbulence model is applied for all calculations. This also implies the use of wall functions to impose the no-slip boundary condition. It is acknowledged that the standard k-ε turbulence model has a moderate performance for some types of flow. These are (i) some external unconfined flows, (ii) flows with large extra strains (e.g. the flow in curved boundary layers, swirling flows), (iii) rotating flows and (iv) fully developed flows in non-circular ducts, see [12]. Results from the validation process will show whether the choice of this turbulence model for the present flow is acceptable.

The effect of gravity is accounted for in the analyses, but it should be mentioned that this is only an additional post-processing feature, since the density is constant.

5.3.3   Discretisation and solution algorithm

Solution of the partial differential equations requires a discretisation scheme. As for the turbulence models, several methods are provided within the CFD method used. Here all calculations have been performed employing the second order MARS scheme (short for Monotone Advection and Reconstruction Scheme) for the momentum equations. This second order method is least sensitive to the mesh structure and skewness [13]. The k-ε model turbulence equations are discretised with a first order upwind differencing (UD) scheme.

The coupling between the velocity and pressure field is resolved with an iterative solution strategy based on the SIMPLE pressure-correction method.

In this algorithm, originally put forward by Patankar and Spalding [14], the convective fluxes are evaluated from an estimated velocity field. Furthermore, an estimation for the pressure distribution is used to solve the momentum equations. The continuity equation then yields a pressure correction equation, which yields a pressure correction field. This pressure correction term is used in turn to update the estimated velocity and pressure field. This process is iterated until the velocity and pressure fields are converged.

The system of discretised partial differential equations is solved with an Algebraic MultiGrid (AMG) algorithm.

Figure 5.4 shows the convergence behaviour of a calculation for an IVR of 1.87. In order to accelerate the convergence, first 125 iterations are carried out with the first order UD scheme for the velocity components. The restart with MARS discretisation causes the step in the residuals of the momentum and the mass. The convergence criterion is set to 10^{-4} for the momentum, mass and turbulent kinetic energy equations.
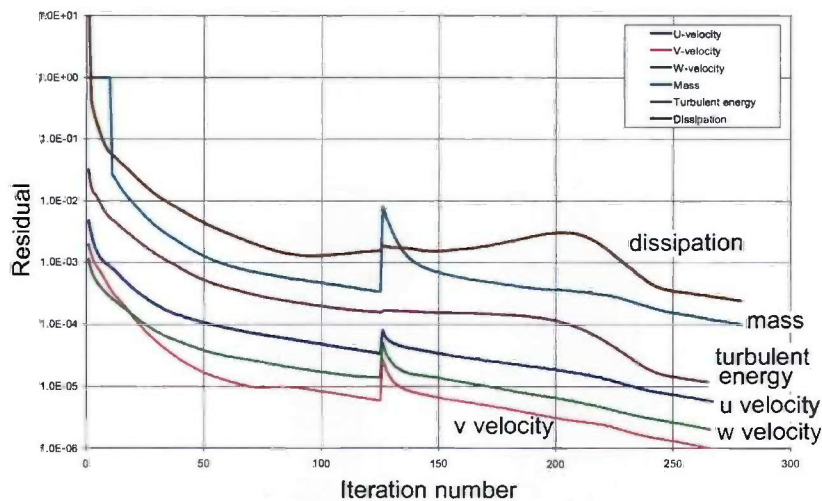
Figure 5.4   Plot of convergence of a calculation of waterjet inlet flow phenomena for IVR = 1.87.

5.4   Validation with experimental data

The experimental data used in this chapter is measured at the Tom Fink cavitation tunnel [11] as described in subsection 3.1.1. In this test program measurements are made on two different inlet geometries. The experimental program consists among others of static pressure measurements along the

ramp centre line, total pressure measurements at the plane just upstream of the impeller, cavitation inception observations at the cutwater and visualisation of streamlines. In the following sections, measured data will be used for comparisons with CFD results.

5.4.1 Comparison of static pressure along the ramp centre line

The static pressure is measured at the ramp centre line at 12 different locations. The locations are determined by the distance along the ramp centre line from the impeller plane towards the entrance of the inlet. The entrance of the inlet, sometimes denoted as ramp tangency point, is located at a distance of 1000 mm for this model scale inlet.

The static pressure is made non-dimensional using the density ρ and the tunnel speed v_{tunnel}:

$$C_p = \frac{p - p_{ref}}{\frac{1}{2}\rho v_{tunnel}^2} \tag{5.1}$$

The reference static pressure p_{ref} and the tunnel speed are taken at a location upstream of the inlet, since the velocity, and the pressure downstream of the inlet vary with the value of IVR value (see equation (2.12)).

The static pressure is measured for eight different IVR values. Table 5.1 shows the conditions, used for the measurements. The Reynolds number Re_{inl} is defined in equation (4.2).

Table 5.1   Parameters of measured conditions for the static pressure distributions. D_{inlet} = 150 mm.

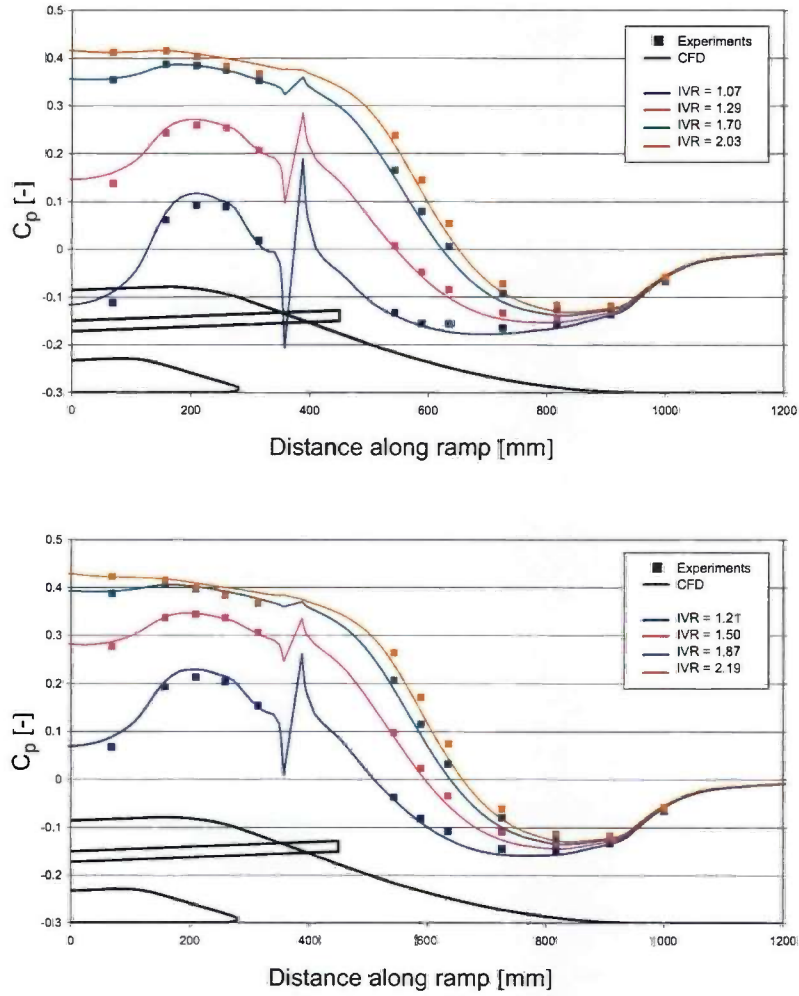| IVR [-] $(=v_{tunnel}/v_{pump})$	v_{tunnel} [m/s]	v_{pump} [m/s]	Re_{inl} [-]
1.07	8.00	7.48	11.21×10^5
1.21	8.00	6.61	9.92×10^5
1.29	8.00	6.20	9.30×10^5
1.50	8.00	5.33	8.00×10^5
1.70	8.00	4.71	7.06×10^5
1.87	8.00	4.28	6.42×10^5
2.03	8.00	3.94	5.91×10^5
2.19	8.00	3.65	5.48×10^5

Figure 5.5   *Comparison of measured and calculated pressure coefficient*
                 Cp along the ramp centre line. Values are given as a function
                 of the distance from the impeller plane. The data for different
                 values of IVR are divided in 2 groups for improved visibility.

The comparison with CFD results is shown in figure 5.5. Values of pressure coefficient Cp along the ramp centre line are given as function of the distance from the impeller plane. The two diagrams present the data for alternate values of IVR.

Both figures show a good agreement between measurements and CFD calculations along the entire ramp section. The discontinuity in calculated pressure between 350 mm and 400 mm is due to the presence of the shaft. This influence is strongest at low IVR since the velocity in the inlet duct is then highest. The static pressure at the impeller plane increases with increasing IVR (due to decreasing v_{pump}) according to the expectations. However, at high IVR values the static pressure is more or less constant. This is due to increased non-uniformity and hydraulic losses.

Figure 5.6 shows the pressure distribution in the symmetry plane of the configuration for an IVR of 1.07 (top) and 2.03 (bottom). It can be observed that the effect of IVR on the pressure distribution is not restricted to the ramp. Clear differences in pressure can be recognized at the cutwater and in the bend of the inlet.

From the pressure distributions can be seen that the location of the stagnation point at the cutwater changes with variation of IVR. As a consequence, the location of minimum value of the pressure also changes. This phenomenon is reported before by Seil [6]. It is shown in more detail in figure 5.7, where the pressure distribution along the cutwater is presented for all calculated IVR conditions. On the left part of the diagram the negative s coordinates represent the lower part of the cutwater, whereas the positive s coordinates represent the upper part of the cutwater. The influence of IVR on the results can be recognised clearly. The stagnation point moves from a negative s coordinate in the positive direction for increasing IVR. The locations of the minimum pressure can be divided in two groups. For IVR conditions up to 1.29 the minimum pressure is found at a location with positive s coordinate. For higher IVR, the location of minimum pressure is found at a negative s coordinate.

The movement of the stagnation point, and consequently the location of the minimum pressure, is related to the change in the shape of the dividing streamtube with varying IVR. The streamtube analysis will be given in section 5.5.

Analysis of the pressure in 5.7 learns that the static pressure at the tunnel outlet plane is not equal to the reference pressure at the inlet plane and moreover, this variation is dependent on IVR. This deviation in static pressure might influence the experimental determination of the cavitation inception pressure, when the location of the minimum pressure is at the lower side (or hull side) of the inlet for high IVR conditions. The cavitation inception results will be compared with CFD results in the next section.
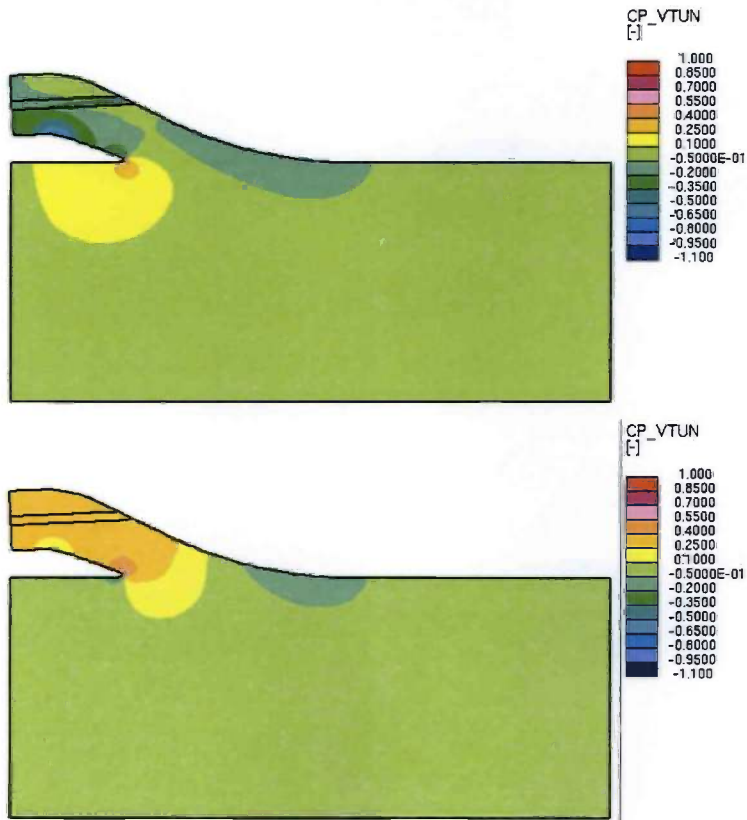
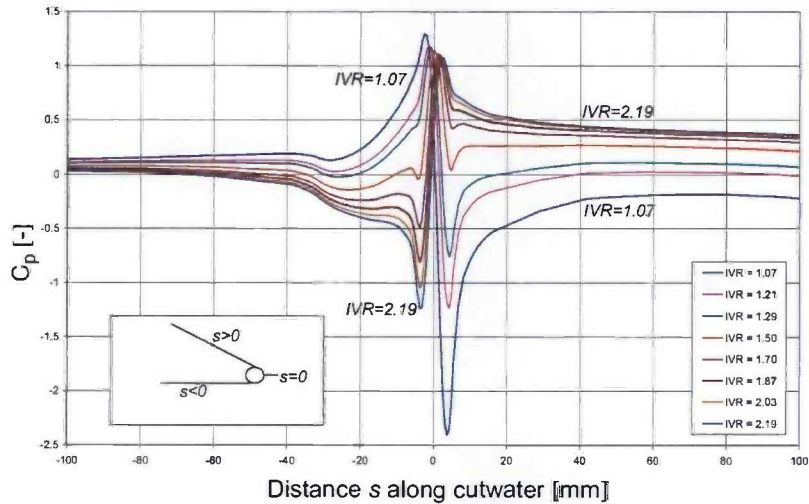Figure 5.6   Pressure coefficient Cp at symmetry plane for IVR of 1.07 (top) and IVR of 2.03 (bottom).

Figure 5.7   *Calculated pressure coefficient Cp along the cutwater for different IVR values. Negative s coordinate represents lower side of cutwater and positive coordinate represents upper side.*

5.4.2   Comparison of cavitation inception pressure at cutwater

Cavitation below the cutwater occurs at high IVR conditions. For four IVR values the inception pressure is determined by visual observation. During the tests the reference pressure p_{ref} in the tunnel is gradually reduced until a small cavity is observed. With this procedure only cavities at the lower side of the cutwater could be observed. These are typical for high IVR conditions. The measuring point for the reference pressure p_{ref} is located upstream of the inlet at half the tunnel height, as shown in figure 3.1 on page 50.

The cavitation inception pressure is presented in non-dimensional form, according to:

$$\sigma_{v\_pump} = \frac{p_{ref} - p_v - \rho g h}{\frac{1}{2}\rho v_{pump}^2} \tag{5.2}$$

where p_v is the vapour pressure of the fluid, h the height correction between the cutwater and the centre plane of the cavitation tunnel and v_{pump} the average axial inflow velocity of the pump. The comparison of the experimental results and the CFD results is shown in figure 5.8.

It should be noted that the pump inflow velocity is used in the definition of σ_{v_pump}, whereas the ship speed is used for C_p. With the current σ definition the inception behaviour of different inlet geometries at high IVR can be evaluated better.

Agreement between experiments and CFD calculations is good for all four tested conditions. The calculated conditions at lower IVR values show the expected behaviour. At a certain IVR the dividing streamline is optimally aligned with the cutwater geometry, which results in a minimum value for σ_{v_pump}. Further decrease of IVR results in the point of minimum pressure, i.e. the cavitation inception point, moving to the inner side of the inlet.
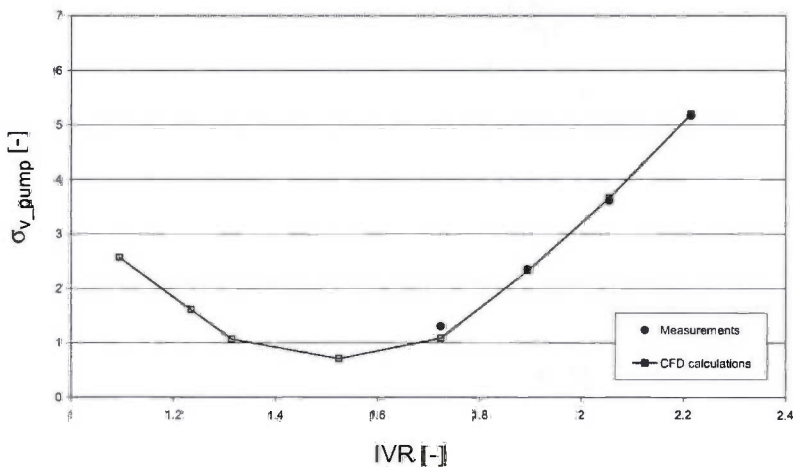
Figure 5.8   Comparison of measured and calculated cavitation inception at cutwater

Effect of tunnel walls

At normal waterjet operating conditions cavitation inception occurs below the cutwater in general. Figure 5.7 shows that the pressure in this region is not constant and depends on IVR. This is due to the effect of tunnel walls and conservation of mass in the complete system. The mass flow which enters the tunnel is split into a part which leaves the domain through the waterjet inlet and a part which leaves through the tunnel exit section. As long as the pump exit is open the mass flow rate at the exit of the tunnel section is lower than at the inlet. Because the tunnel cross-section is constant, this results in

lower velocities and consequently a higher static pressure. The pressure increase as a function of IVR can be estimated as:

$$\Delta C_p = \frac{2A_{pump}}{IVR \cdot A_{tunnel}} - \left(\frac{A_{pump}}{IVR \cdot A_{tunnel}}\right)^2 \qquad (5.3)$$

where A_{pump} is the cross-sectional area at the impeller plane and A_{tunnel} the cross-sectional area of the tunnel. The effect of viscous losses is neglected in this estimation.

The diameter of the cross-sectional area at the impeller plane is 150 mm and the cavitation tunnel has a square section of 600 x 600 mm. The velocity at the outlet of the tunnel shows a drop of about 5% for an IVR = 1.0 to 2% for IVR = 2.0. Figure 5.9 shows the pressure difference ΔCp based on the CFD results and the theoretical value. Agreement between the analytical value and the numerical result is good over the complete IVR range.

Equation (5.3) neglects the effect of the displacement thickness of the boundary layer on the tunnel walls in the calculation of the mass fluxes. Inclusion of this displacement thickness will result in a slightly lower mass flow entering the tunnel section, which is equivalent to a lower IVR. The analytical pressure difference estimate will increase with less than one percent in this case. This simplification is assumed to be justified. Moreover, hydraulic losses in the tunnel are not taken into account in the estimation. These hydraulic losses will reduce the actual pressure increase in the tunnel. However, for a first indication of the effect of the confinement of the tunnel
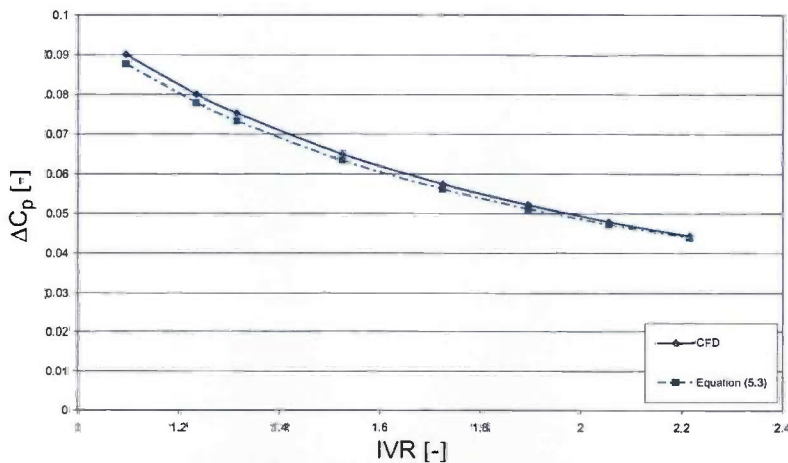
Figure 5.9   Dimensionless pressure increase in tunnel section based on CFD results and analytical formula
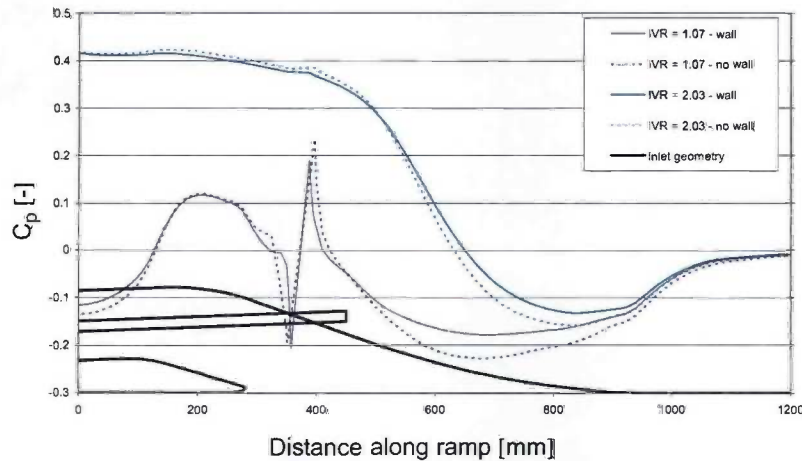
Figure 5.10   Comparison of calculations of static pressure distribution along
              ramp for configuration with and without tunnel walls

walls on the pressure distribution, equation (5.3) can be used as a first
estimate.

In actual conditions at open sea the equivalent cross sectional area goes to
infinity and consequently the pressure difference tends to zero. This is in
accordance with the expectations.

Effect of the tunnel walls on static pressure distribution along the ramp is
shown in figure 5.10 for two IVR values. These are the same conditions as
shown in the symmetry plane pressure distributions of figure 5.6. Clear
deviations between the calculation with and without the walls can be seen in
the first part of the inlet. In this region the pressure is influenced most by the
local tunnel pressure. Moreover, the deviations are larger for the low IVR
condition. This is in line with equation (5.3). Further downstream in the inlet
duct the pressure distribution is similar for both configurations.

It is to be expected that the largest influence of the tunnel pressure increase,
due to the wall confinement, is found in the tunnel downstream of the
cutwater. This is the location where the cavitation inception occurs at medium
and at high IVR. The effect of the tunnel walls on cavitation inception
pressure is shown in figure 5.11. The deviations between the two series of
calculations are large. For a cavitation free design, the cavitation inception
diagram of the inlet is matched with the available ambient pressure. The
cavitation inception diagram represents the required pressure to avoid
cavitation. As long as the required pressure is lower than the available
ambient pressure, cavitation free operation is possible. Figure 5.11 shows
that the required pressure, based on experiments or calculations with tunnel
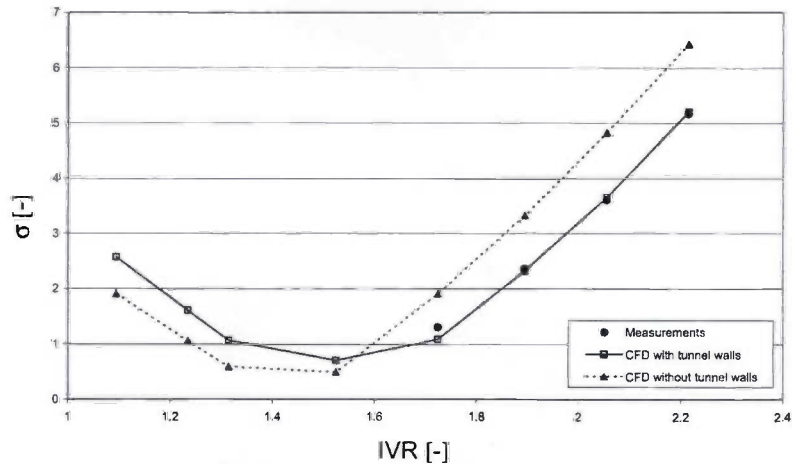
*Figure 5.11   Comparison of calculations of cavitation inception pressure for
configuration with and without tunnel walls*

walls is too optimistic for medium and high IVR. The actual required pressure
is higher, as can be seen from the calculations without tunnel walls. This
effect should always be taken into consideration when interpreting cavitation
inception results in a test set-up with finite dimensions.

5.4.3   Comparison of total pressure at impeller plane

Good agreement between measurements and calculations is shown in the
previous subsections for the static pressure along the ramp and the cavitation
inception that occurs at the cutwater. In this subsection the total pressure
distribution in the impeller plane is evaluated. The impeller plane is defined as
the cross-sectional area at the end of the inlet, just upstream of the impeller,
as shown in figure 3.1.

Total pressure measurements have been made with a pitot-rake positioned at
different radii. In the tangential direction steps of 10 degrees are made
between the measurement locations.

Figures 5.12a to 5.12d show the comparison between the measured and the
calculated total pressure distribution for four different IVR conditions. The
lowest IVR is a normal operating condition of 1.68 and the highest IVR is a
very high speed condition of 2.19. The other two IVR conditions are in
between with values of 1.87 and 2.03. The results are made non-dimensional
with the tunnel speed in a similar way as the static pressure, i.e.:

$$C_{ptot} = \frac{p_{tot} - p_{ref}}{\frac{1}{2}\rho v_{tunnel}^2} \tag{5.4}$$

The experimental data shows total-pressure losses up to 65% at the highest pump speeds (low IVR) in the wall boundary layer. In the region around 12 o'clock, i.e. the region affected by the flow around the stationary shaft losses are found up to 50%.
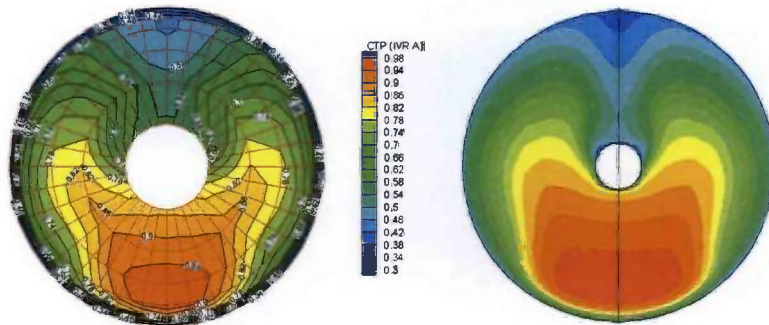

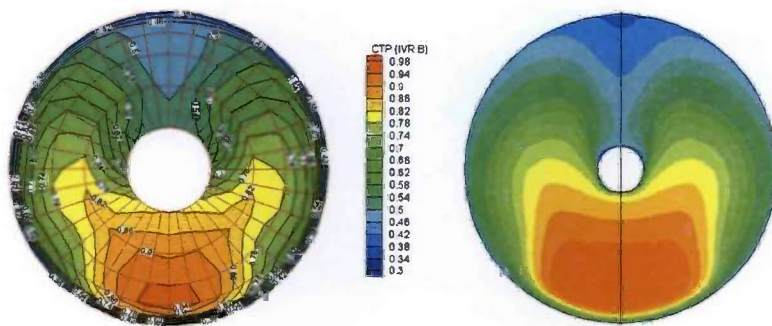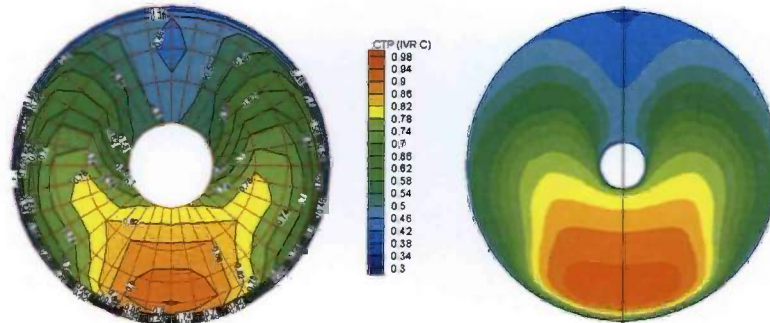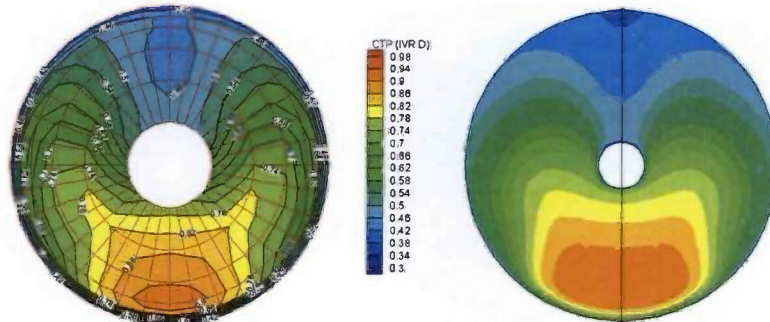*Figure 5.12a   Comparison of measured (left) and calculated total pressure distribution in impeller plane for IVR = 1.68*

Figure 5.12b   Comparison of measured (left) and calculated total pressure distribution in impeller plane for IVR = 1.87

Figure 5.12c   Comparison of measured (left) and calculated total pressure
distribution in impeller plane for IVR = 2.03

Figure 5.12d   Comparison of measured (left) and calculated total pressure
distribution in impeller plane for IVR = 2.19

For all four conditions the qualitative agreement between the measurements
and the calculations is good. The typical distribution and the effect of the shaft
is reproduced well within the CFD model. It appears that the computed
boundary layer is thinner than in the experiment. However, measuring with a
total pressure tube close to the wall will be troublesome.

Comparison of the four IVR conditions shows that in the region affected by
the presence of the shaft, a decrease of the total pressure level with
increasing IVR takes place. This means an increase of hydraulic losses with
increasing IVR. This increase is in accordance with the expectations and this
is partly due to the increased retardation of the flow as discussed in chapter
3.

5.4.4   Comparison of velocity field at impeller plane

Total pressure measurements of the previous subsection are used to derive an axial velocity field. In this derivation a constant static pressure over the cross-section is assumed. moreover, the influence of the in-plane velocity components is neglected. The axial velocity is derived from the experimental data according to:

$$v_{axial} = \sqrt{\frac{p_{tot} - p_{stat}}{\frac{1}{2}\rho}} \tag{5.5}$$

Integration of the axial velocity over the impeller plane showed that the flow rate was predicted within 2.5% compared to the measured flow rate. The comparison between the value of the axial velocity derived from the measured total pressure and the calculated axial velocity component is shown in figures 5.13a to 5.13d in a similar way as for the total pressure distribution. The axial velocity is normalised with the averaged axial velocity.
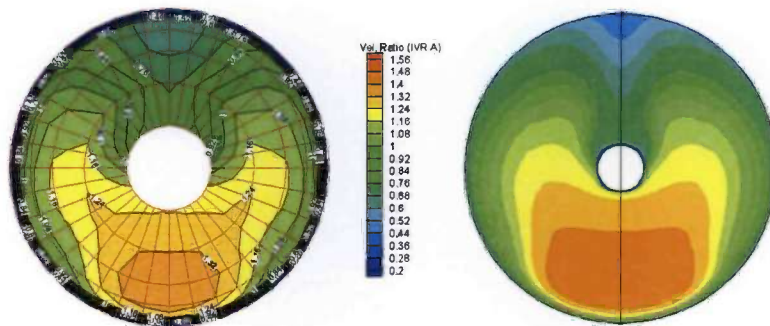

Figure 5.13a   Comparison of axial velocity derived from measured total pressure (left) and calculated axial velocity distribution in impeller plane for IVR = 1.68
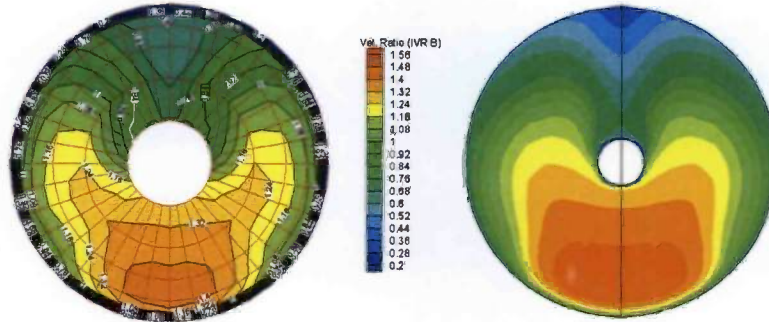
Figure 5.13b   Comparison of axial velocity derived from measured total pressure (left) and calculated axial velocity distribution in impeller plane for IVR = 1.87
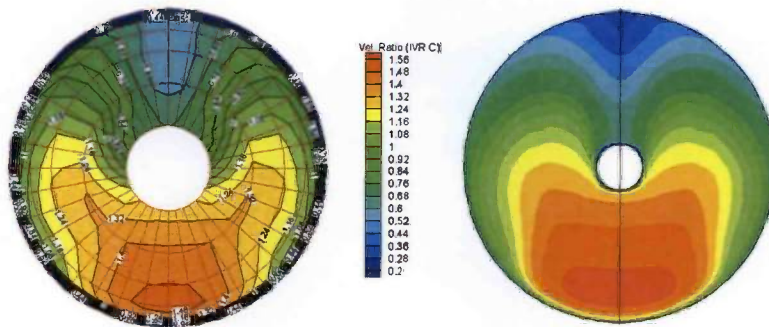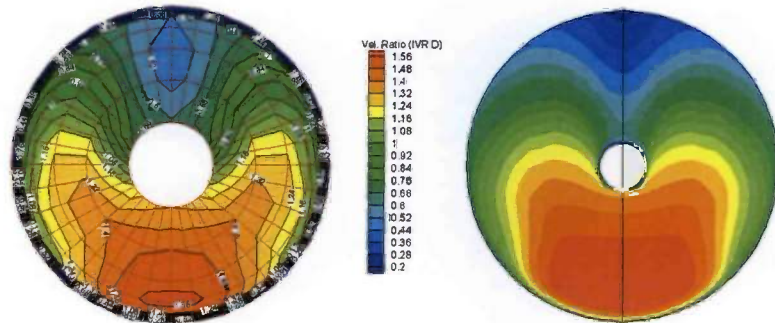

Figure 5.13c   Comparison of axial velocity derived from measured total pressure (left) and calculated axial velocity distribution in impeller plane for IVR = 2.03

Figure 5.13d   Comparison of axial velocity derived from measured total pressure (left) and calculated axial velocity distribution in impeller plane for IVR = 2.19

Qualitative agreement between experimental data and calculated velocity field is good for all four IVR conditions. The location and magnitude of minimum and maximum axial velocity is predicted well with the numerical method.

The numerical results of the velocity distribution are compared to the representation of the measured data by Fourier-series (see section 3.1). The deviation between the two is used to quantify the relative error of the calculated axial velocity. Figure 5.14 shows the relative difference for the both low IVR of 1.68 and the high IVR of 2.19.

The relative difference is defined as:

$$\Delta = \frac{v_{CFD} - v_{EXP}}{v_{aver}} \tag{5.6}$$

with v_{EXP} based on the two dimensional Fourier representation of the measured data.

The deviations are below 15% for a significant part of the cross-sectional area. It is concluded that the CFD analysis of the inlet flow reproduces the typical non-uniform velocity distribution well. Therefore, the CFD method employed in the present investigation seems suitable for the investigation of the effect of non-uniform inflow into the mixed-flow waterjet pump.
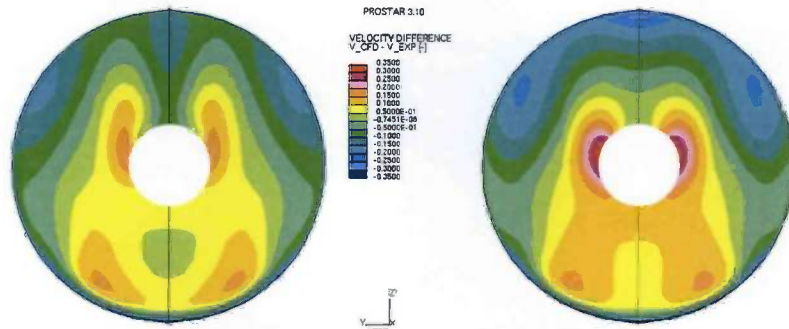
Figure 5.14   Relative difference between experimental data and calculated axial velocity distribution at impeller plane for IVR = 1.68 (left) and IVR = 2.19

The velocity distributions show a clear increase of non-uniformity with increasing IVR,i.e. decreasing v_{pump}. The non-uniformity can be represented in a single value, if calculated according to equation (3.1). Figure 5.15 shows the non-uniformity parameter ζ as a function of IVR. Both the results of calculations with wall and pressure boundary conditions have been used. The relation between the IVR and the non-uniformity is shown clearly for the two types of boundary conditions. The small deviations are negligible.
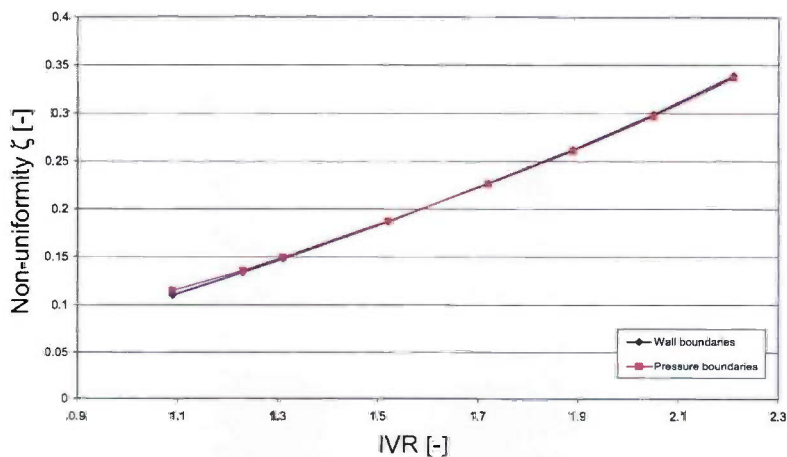

Figure 5.15   Non-uniformity parameter ζ in impeller plane as function of IVR

Figure 5.13d shows a region with very low axial velocity in the upper part of the cross-sectional area. For such conditions there may even be a region of flow recirculation upstream of the impeller plane.

The distribution of the magnitude of the velocity in the symmetry plane for two different values of IVR, is shown in figure 5.16. At low IVR conditions the effect of the bend on the velocity distribution can be recognised. At the inner corner of the inlet the velocity reaches a maximum value which reduces further downstream. This effect is less pronounced at high IVR conditions.

In the region in the bend above the shaft a very low velocity magnitude is observed. Here flow separation is likely to occur at sufficiently high IVR, i.e. low values of v_{pump}. The method to determine boundary layer separation will be discussed in section 5.6, where additional flow phenomena in a waterjet inlet are reviewed.
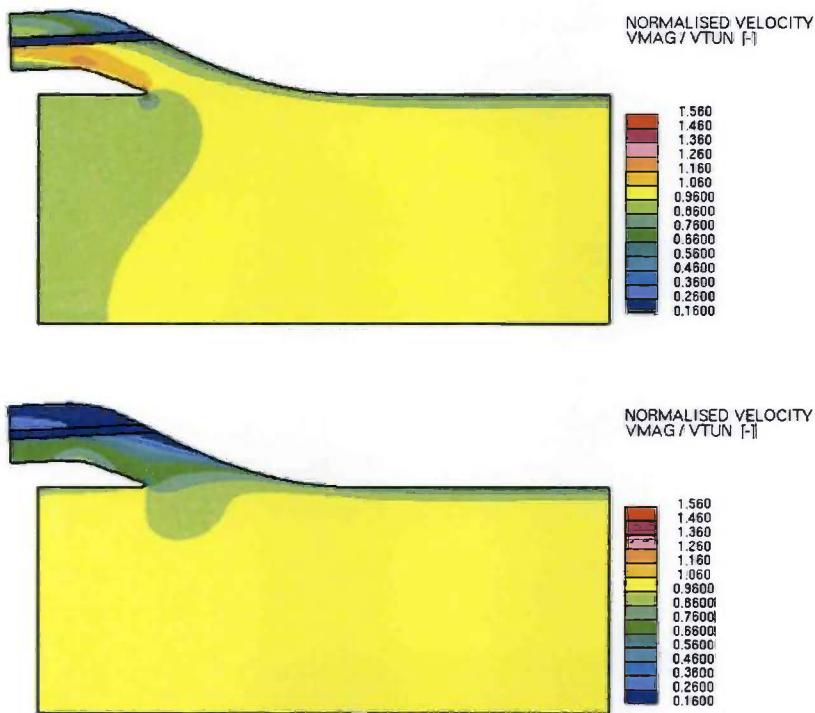
NORMALISED VELOCITY
VMAG / VTUN [-]

1.560
1.460
1.360
1.260
1.160
1.060
0.9600
0.8600
0.7600
0.6600
0.5600
0.4600
0.3600
0.2600
0.1600

NORMALISED VELOCITY
VMAG / VTUN [-]

1.560
1.460
1.360
1.260
1.160
1.060
0.9600
0.8600
0.7600
0.6600
0.5600
0.4600
0.3600
0.2600
0.1600

Figure 5.16   Distribution of magnitude of velocity in symmetry plane for IVR
1.07 (top) and 2.03 (bottom)

5.4.5   Results obtained with k-ω turbulence model

The use of turbulence models in CFD calculations always provides reason for discussion. Though an in-depth study of effects of turbulence models on the flow in waterjets does not fit within the scope of this thesis, results of calculations with the k-ω turbulence model will be shown for comparison with results of the k-ε turbulence model. The k-ω turbulence model is used widely just like the k-ε turbulence model. Often, the level of accuracy or the absence of accuracy of a CFD calculation is attributed to the turbulence model used. Comparison of the experimental data with the results of calculations employing the k-ω turbulence model can show whether the result is sensitive to the choice of a particular turbulence model.

Comparison of static pressure along ramp centre line

Figure 5.17 shows the static pressure distribution along the ramp as calculated with the k-ω turbulence model. Agreement between calculations and experimental data is good for all four presented conditions. Similar results have been found for intermediate IVR conditions. The accuracy of the calculations is comparable to the calculations with the k-ε turbulence model, as shown in figure 5.5. The main differences are in the region downstream of the shaft, where the pressure predicted by the method employing the k-ω model gives higher values than the ones predicted by the method using the k-ε model. This suggest that flow separation occurs later for the method employing the k-w model.
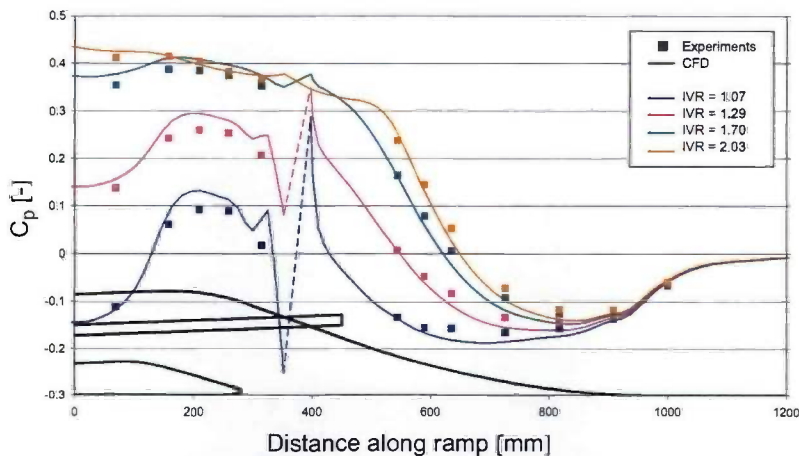

Figure 5.17   Comparison of measured and calculated static pressure along ramp centre line obtained with k-ω turbulence model

Comparison of velocity field at impeller plane

The assessment of the performance of the k-ω turbulence model is not only based on the prediction of static pressure, but also on the prediction of the velocity field. Figures 5.18a and b show the comparison of the velocity distribution at the impeller plane for two IVR conditions. Agreement is good for both conditions.

The relative difference between calculations and data derived from the measurements is shown in figure 5.19 for both conditions. The majority of the cross-sectional area has a difference below +/- 10%. Quantitative agreement seems to be slightly better with the k-ω turbulence model than with the k-ε model, see figure 5.14.
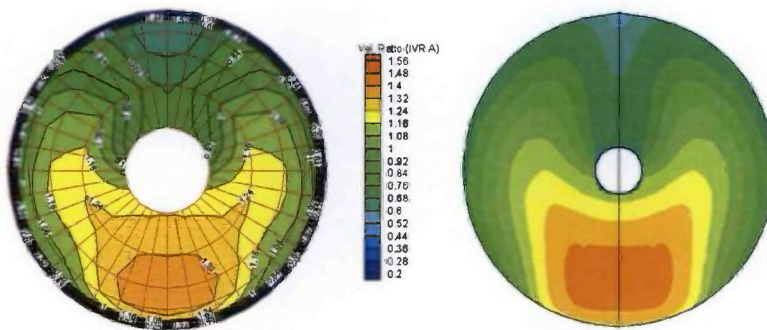

Figure 5.18a   Comparison of axial velocity derived from measurements (left) and calculated axial velocity distribution with k-ω turbulence model in impeller plane for IVR = 1.68

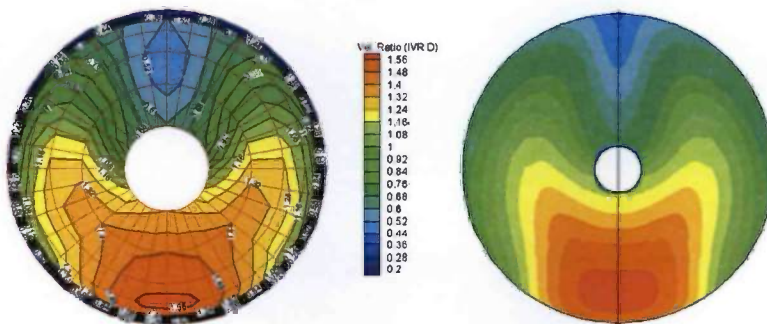*Figure 5.18b   Comparison of axial velocity derived from measurements (left) and calculated axial velocity distribution with k-ω turbulence model in impeller plane for IVR= 2.19*
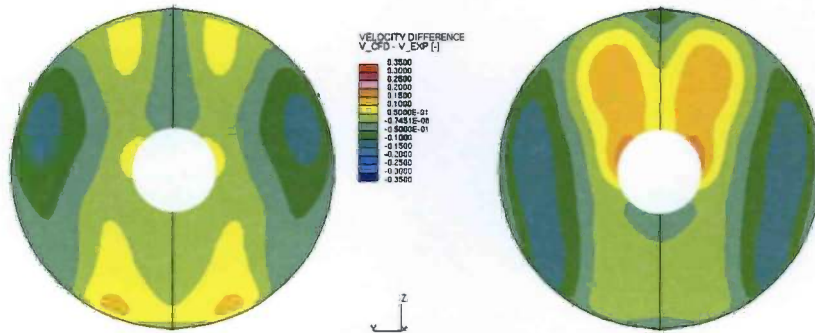
Figure 5.19   Relative difference between experimental data and calculated axial velocity distribution with k-ω turbulence model in impeller plane for IVR = 1.68 (left) and IVR = 2.19

5.4.6   Mesh convergence study

The mesh as used in this study has been made coarser and finer to evaluate to mesh convergence of the applied mesh. For the coarse mesh, the block divisions of the blocks near the symmetry plane of the original mesh are reduced by a factor of two in the direction perpendicular to the symmetry plane. In the direction along the cutwater the number of cells is reduced by a factor of two as well for the blocks near the cutwater. The reduction of cells from the original mesh to the coarse mesh is about 30.000, but it should be noted that this reduction is achieved mainly in the region of the cutwater.

The fine mesh is derived from the original mesh by doubling all block divisions in all three directions. The number of cells in the normal direction of the extrusion layer has been kept constant to remain at the same y^+ values.

It should be noted, that the original medium mesh size has been developed about 5 years ago. The number of cells of the original mesh, of about 200.000, were governed by the hardware constrains of that time. Currently, the tools for generation of inlet meshes are used in the design procedure for waterjet inlet geometries. In order to have calculation times, which are acceptable during the design phase, the default number of cells has not been increased. Nevertheless it is now possible to run the refined mesh, which has about 1.5 million cells.

The pressure distribution along the cutwater, as shown in figure 5.7 will be reviewed for the different meshes, because the largest gradient are present in this region. Figure 5.20 shows the pressure coefficient for IVR = 1.87 along the cutwater for the three different meshes.
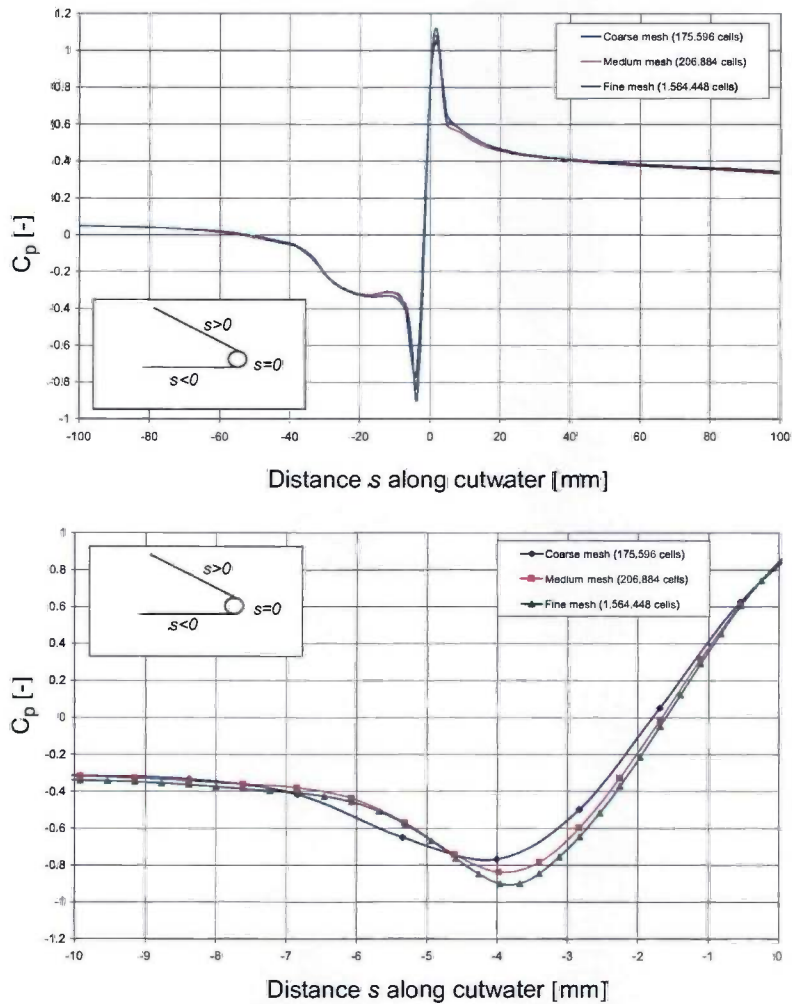
Figure 5.20   Calculated pressure coefficient Cp along the cutwater for different mesh sizes for IVR of 1.87. Top figure shows s range of -100 to 100 and bottom figure shows region with location of minimum pressure, located between s range of -10 and 0. Negative s coordinate represents lower side of cutwater and positive coordinate represents upper side.

The region with the location of the minimum pressure is shown in detail in the second diagram. The markers in this figure represent the corner points of the cells.

Increase of the number of cells with a factor of 8 results in a difference of the prediction of minimum pressure Δc_p=0.06 for this condition. The difference is found along a small part of the cutwater region of about 2 mm, which is 1.3% of the inlet diameter.

The difference in pressure distribution along the cutwater between the original mesh and the fine mesh is regarded to be representative for the complete mesh. Since the deviations between the two meshes are limited to a small region near the cutwater and the magnitude of the difference is small, is it concluded that the cell sizes of the original mesh are suitable for the presented study.

5.4.7   Closing remarks

Agreement between the experimental data and the results of the calculations is quite good, despite the mentioned deficits of the k-ε turbulence model. Performance of the k-ω turbulence is comparable. It is not an aim to benchmark turbulence models in this study, and therefore the k-ε model is used in the remainder of the analyses.

One aspect of the use of RANS methods has not been addressed yet. This is the capability to calculate the flow for geometries according to full scale dimensions with full scale boundary conditions. Calculations of full scale waterjet inlets only require a refinement of the cells near the solid walls in order to keep acceptable y^+ values. The thickness of the actual hull boundary layer can be applied at the inflow boundary condition. In this way, the effect of a thicker boundary layer, due to an increase in the length of a vessel, can be taken into account for example.

5.5   Analysis of the suction streamtube

The preceding section covers the comparison of measured and calculated results. Typical quantities which can be measured in experimental facilities are total and static pressure. Velocities can be derived from this data afterwards. The CFD results provide a wide range of additional post-processing capabilities to get more insight into the behaviour of the flow. Examples include the calculation of shear stresses along the inlet surface and the determination of the suction streamtube. The CFD results used in this section are the results obtained for the waterjet inlet without tunnel walls, this in order to avoid possible effects of the confinement on the flow of the presence of the cavitation tunnel walls.

5.5.1 Visualisation of suction streamtube

The CFD method provides a way to introduce a concentration scalar as a passive traces in the flow field. This concentration scalar can be implemented at inlet or pressure boundaries and it can be used as a weight function for further analysis.

The shape of the streamtube is not known in advance. In fact, only at the impeller plane the streamtube is known to coincide with the impeller plane boundary. Setting the concentration factor to 100% in the impeller plane allows for the determination of the complete streamtube with a upstream tracing method. In this approach the flow field is reversed and frozen, which is allowed in a steady flow problem. With the frozen velocity field, the solution of the scalar only takes a few iterations for the complete numerical domain.

The shape of the streamtube is derived from an iso-surface plot of the concentration. In this way a clear representation of the streamtube interface can be obtained. An example of the three-dimensional streamtube visualisation is shown in figure 5.21 from different view angles.
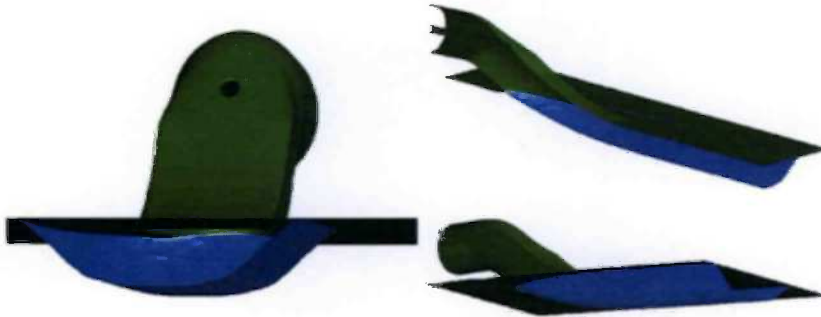

Figure 5.21   Visualisation of three-dimensional suction streamtube for IVR=1.29

5.5.2 Determination of suction streamtube shape

The shape of the suction streamtube at the inlet boundary of the domain can be used to calculate the average ingested velocity v_{in}. This velocity is used in the calculation of the wake fraction w and the thrust of the installation. Determination of the cross-sectional area of the streamtube at several locations upstream of the impeller plane provides information about the diffusor effect in the streamtube. The values of the cross-sectional areas can be used to calculate the equivalent diffusor angles. This will give an indication of the risk of the onset of boundary layer separation in the inlet duct.

Cross-sectional shape of streamtube at inlet boundary

The shape of the suction streamtube at the inlet boundary of the numerical domain can be approximated with a semi-elliptical shape. An example is given in figure 5.22 for a range of IVR values. The boundary of the streamtube can be approximated by the ellipse:

$$\left(\frac{y}{w_0}\right)^2 + \left(\frac{z}{h_0}\right)^2 = 1 \tag{5.7}$$

where $2w_0$ and h_0 are the maximum width and maximum height resp. These two parameters are determined by employing a least-square fit of the data determined from the computed streamtube surface cross-section at the inlet plane of the computational domain.

The elliptical curve fit can be used to determine the mass averaged inflow velocity of the ingested fluid out of the boundary layer. In the calculations a power-law exponent n=7 and a boundary layer thickness of 0.3D, with D the inlet diameter, is used.
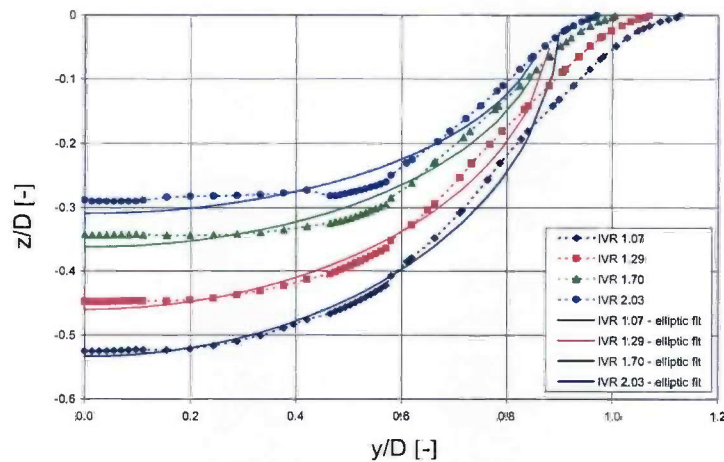

Figure 5.22   Computed semi-elliptical shape of suction streamtube at inlet of numerical domain for various IVR conditions

An efficient method to determine the inflow velocity is based on the integration of the streamtube velocity. Once the concentration scalar is

available, the mass averaged inflow velocity can be determined by simple integration:

$$v_{in} = \frac{\displaystyle\int_{A_{inflow}} \rho(c \cdot v_x^2)dA}{\displaystyle\int_{A_{inflow}} \rho(c \cdot v_x)dA} \tag{5.8}$$

In this equation the concentration scalar is denoted by c and x is the direction normal to the inflow area A_{inflow}.

Figure 5.23 shows the calculated wake fraction w (as defined in equation (2.2)) based on the elliptical streamtube shape and on direct integration of the CFD results. The rectangular box approach is also plotted for three different widths of the box.
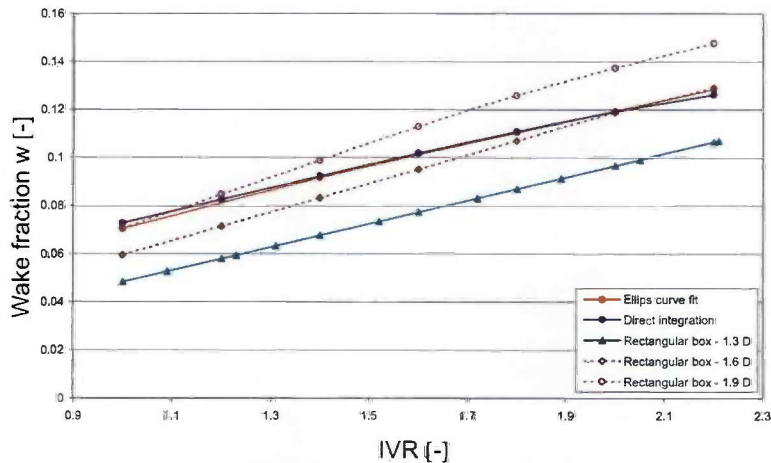

Figure 5.23   Calculated wake fraction w based on elliptical fit, rectangular box method and direct integration of CFD results.

The method of direct integration and the method of the elliptical curve fit give more or less comparable results for the wake prediction. The method, based on a rectangular streamtube with a width of 1.3D, gives an underestimation of the wake fraction of about 20%. The other two curves for the rectangular box, based on 1.6D and 1.9D, show that a width depending on IVR is required to obtain a good fit. It is acknowledged that the value of 1.3D is an empirical factor, which has been derived in the past to obtain good correlations with the actual sailing fleet.

Cross-sectional area of streamtube

In the preceding section the cross-sectional shape of the streamtube at the inflow boundary has been discussed. Here the development of the cross-sectional area of the streamtube will be analysed in more detail. The cross-sectional area has been determined at 9 different stations. The cross-sections are taken perpendicular to the ramp surface from the inlet boundary to the cutwater, as shown in figure 5.24. The area is determined by integration of the concentration factor over the whole plane:

$$A_{tube} = \int_{A_n} cdA \qquad (5.9)$$

where n is the integration plane index number, in the range 1 to 9.
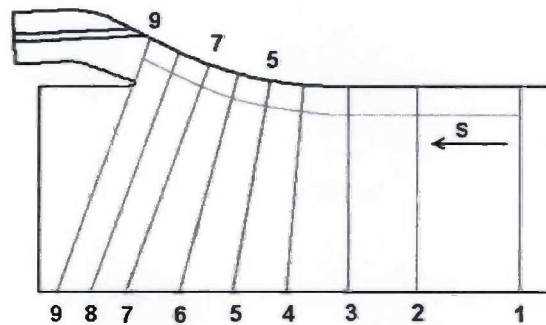

Figure 5.24   Location of streamtube cross-sections. The parameter s is the length along the waterjet inlet contour in the plane of symmetry.

Figure 5.25 shows the development of the cross-sectional area of the streamtube. The areas are normalised with the streamtube area at plane 9. This area is denoted as intake throat area [2]. The distances are calculated from the first plane to the throat area.
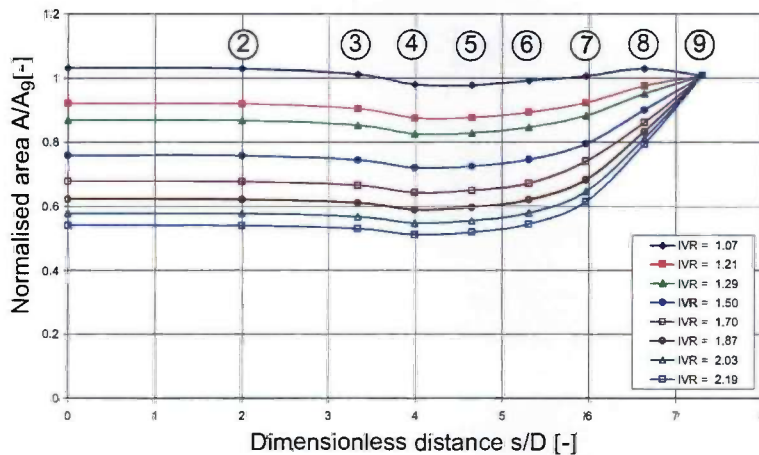
Figure 5.25   Streamtube cross-sectional area normalised by A_9. The numbers refer to the integration plane index numbers, as shown in figure 5.24.

Far upstream, near the inflow plane, a constant cross-sectional area is found for each IVR condition. The influence of the ramp curvature, at cross-section numbers 4 and 5, can be recognised as a small region of reduced area, which is due to an acceleration of the flow. The typical retardation of the flow at higher IVR (i.e. lower v_{pump}) conditions is reflected in a steep increase of the streamtube area when approaching the inlet lip.

The development of the streamtube in streamwise direction can also be expressed in an equivalent diffuser angle α_{diff}. This diffusor angle is based on the equivalent streamtube diameter and the distance dl between the different cross-sections:

$$\alpha_{diff} = \text{atan}\left(\frac{D_{n+1} - D_n}{dl}\right)$$
(5.10)

The equivalent diameter is based on a circular section with area identical to the area of the streamtube cross-section. The variation of the equivalent diameter along the streamtube in streamwise direction has been fitted with a fifth order polynomial. With this curve fit the diffuser angle α_{diff} can be derived in small steps of the length dl.

The development of the diffusor angle along the streamtube up to the cutwater is shown in figure 5.26 for various IVR values.
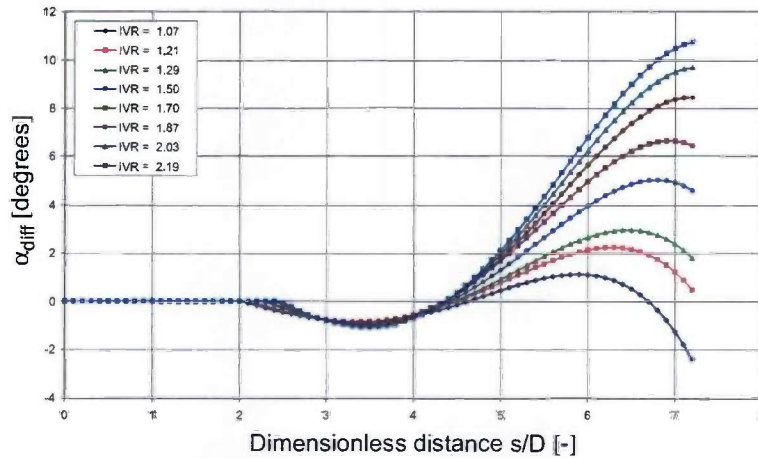
Figure 5.26   Equivalent diffuser angle α_{diff} of streamtube

At the ramp curvature (around s/D = 3.5), all conditions show a small negative value of α_{diff}, which represents the contraction of the streamtube. At IVR conditions of 1.87 and higher, the diffuser angle exceeds 8 degrees. At such high diffuser angles, flow separation is likely to occur in normal circular diffusers [15]. The occurrence of flow separation will be discussed in more detail in the following subsection.

5.6   Evaluation of wall shear stress

Evaluation of the wall shear stress in the inlet duct can provide information about the probability of flow separation in the inlet. Flow separation will lead to increased non-uniformity of the flow in the impeller plane and higher hydraulic losses. This is a deterioration of the performance of the whole propulsion system and should be avoided in the range of normal operating conditions. Boundary layer separation will occur inside the inlet duct at the ramp side, because of the strong adverse pressure gradient acting on the flow. Occurrence of this large pressure gradient at high IVR (i.e. low v_{pump}) has already been demonstrated in figure 5.5 in subsection 5.4.1.

Determination of a possible region of separated flow is based on the magnitude of the wall shear stress along the duct. It is assumed that the onset of separation occurs at the location where the wall shear stress

reduces to a zero value [16]. The dimensionless wall shear stress is denoted as the dimensionless friction velocity v_f:

$$v_f = \sqrt{\frac{\tau_w}{\rho v_{pump}^2}} \tag{5.11}$$

The non-dimensional representation can be used to get a more comprehensive comparison of calculations for varying pump velocity.

For the standard flush-type inlet geometries, possible flow separation is located inside the duct near station 9 (as shown in figure 5.24). The wall shear stress component in axial direction will change sign in case of boundary layer separation in this region. For the detection of flow separation, the friction velocity is multiplied with the sign of the axial wall shear stress.

Figure 5.27 shows the result of the evaluation of the minimum wall shear stress at the waterjet inlet duct part. Results of calculations with both wall as well as pressure boundaries are used in this evaluation. The difference between the results of both series of calculations is negligible.

According to the wall shear stress criterion, flow separation will occur for IVR values higher than 1.75. This is in accordance with the maximum allowable diffuser angle criterion of 8 degrees (as shown in figure 5.26).

For a practical inlet design, flow separation should not occur at normal operating conditions. With a dedicated inlet geometry design it is possible to avoid flow separation in the inlet for all operating conditions.
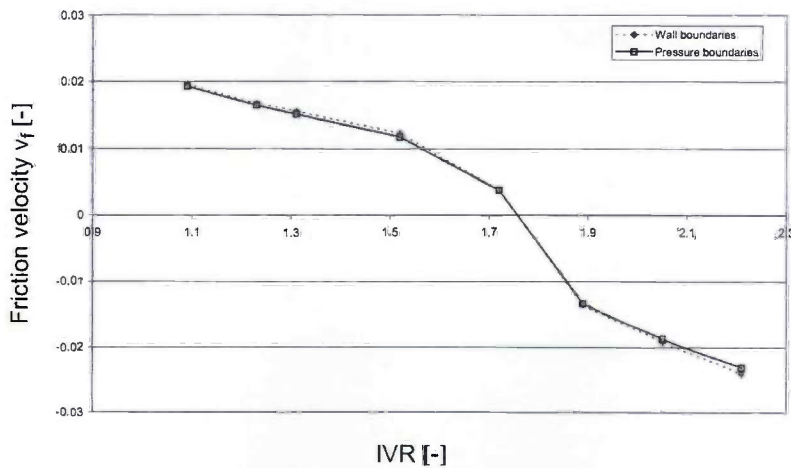

Figure 5.27   Dimensionless wall shear stress as function of IVR

5.7 Nomenclature

A	area	m^2
c	concentration	-
C_p	pressure coefficient	-
g	gravitational acceleration	m/s^2
h	height from tunnel centre line to cutwater	m
h_0	maximum suction depth	m
IVR	inlet velocity ratio (v_{ship}/v_{pump})	-
p	static pressure	N/m^2
p_0	static ambient pressure in tunnel	N/m^2
p_v	vapour pressure	N/m^2
v	velocity	m/s
v_f	friction velocity	-
w_0	maximum suction half width	m
y,z	coordinates	m

Greek symbols

ρ	fluid density	kg/m^3
σ	cavitation inception pressure	-
τ_w	wall shear stress	N/m^2

Subscripts

n	normal direction
pump	based on values just upstream of the impeller
tunnel	based on tunnel values
x	axial direction

5.8 References

[1] Førde, M., Ørbekk, E., Kubberud, N., 'Computational Fluid Dynamics applied to high speed craft with special attention to water intake for water jets', FAST'91 conference, pp. 69-89, Trondheim, 1991

[2] Terwisga, T.J.C. van,'Waterjet-hull interaction', PhD thesis, Technical University of Delft, 1996

[3] Pylkkänen, J.V.,'Test cases of application of CFD code to predict waterjet inlet flows', Technical report VTT VAL B-11, VTT Manufacturing Technology, Maritime Research, Espoo, 1994

[4] Pylkkänen, J.V.,'CFD analysis and iterative design of waterjet inlet', International conference on ship and marine research, Rome, 1994

[5] Vorst, H.J.A. van der, Verbeek, R., Hendriks, A.J.A.M., 'Design considerations of waterjet propulsion systems', 13th Fast Ferry International Conference, Singapore, 1997

[6] Seil, G.J., Fletcher, C.A.J., Doctors, L.J., 'The application of computational fluid dynamics to practical waterjet propulsion system design and analysis', Proceedings of the 3rd international conference on Fast Sea Transportation, pp 1379-1390, Lubeck-Travemunde, 1995

[7] Yang, C.K., Lee, Y.B., Choi, H.S., 'A numerical analysis of the flow around the waterjet inlet', Proceedings of the 3rd international conference on Fast Sea Transportation, pp 1391-1401, Lubeck-Travemunde, 1995

[8] Bulten, N.W.H.,'Influence of boundary layer ingestion on waterjet performance parameters at high ship speeds', Proceedings of the 5th international conference on Fast Sea Transportation, pp 883-892, Seattle, 1999

[9] Hu, P., Zangeneh, M., 'Investigations of 3D turbulent flow inside and around a water-jet intake duct under different operating conditions', ASME Journal of Fluids Engineering, Vol 121, pp. 396-404, 1999

[10] Hu, P., Zangeneh, M., 'A method for automatic optimisation of the intake duct geometry of marine water-jets', Proceedings of the 5th international conference on Fast Sea Transportation, pp 843-851, Seattle, 1999

[11] Brandner P., Walker, G.J.,'A waterjet test loop for the Tom Fink cavitation tunnel', Proceedings Waterjet Propulsion III conference, Gothenburg, 2001

[12] Versteeg, H.K., Malalasekera, W., 'An introduction to Computational Fluid Dynamics', Longman Scientific & Technical, Essex, 1995

[13] Computational Dynamics Limited, 'Star-CD methodology, version 3.150', 2001

[14] Patankar, S.V., Spalding, D.B., 'A calculation procedure for heat, mass and momentum transfer in three-dimensional parabolic flows', Int. J. Heat Mass Transfer, Vol 15, pp. 1787-1806

[15] Schlichting, H., 'Boundary layer theory', McGraw-Hill, New York, 1968.

[16] Fox, R.W., McDonald, A.T., 'Introduction to fluid mechanics', Third edition, John Wiley & Sons, New York, 1985

Chapter 6   Numerical analysis of waterjet pump flow

This chapter deals with the numerical analysis of the mixed-flow waterjet pump. The geometry and mesh generation procedure will be discussed in section 6.1. The numerical domain encloses the impeller, the stator bowl and a straight suction pipe. Subsequently, in section 6.2, the choice of boundary conditions and the options for implementation of impeller rotation are reviewed. In section 6.3, results of the CFD calculations with uniform inflow are compared with available experimental data to get an indication of the accuracy of the numerical method used. The experimental data is measured during the development of the waterjet pump and is only available at the authors' company. This data is used for the prediction of the performance of the full scale installations.

The influence of a non-uniform inflow on the performance is presented in section 6.4. Its effect on the radial loading of the impeller is treated as well. The axial velocity distributions as shown in the previous chapters, are used as input velocity distributions.

6.1   Geometry and mesh generation

The numerical domain for the analysis of the flow through the mixed-flow pump includes the complete impeller and the stator bowl with guide vanes. Preliminary calculations assuming periodic flow, i.e. reducing the calculation to computing the flow through a single impeller channel showed poor agreement with experimental data. This can be partly attributed to the applied boundary condition of constant pressure at the outlet part of the numerical

domain. The choice to model the complete impeller and stator enables the use of a constant pressure boundary condition at the outlet. Upstream of the pump a straight suction pipe is incorporated in the numerical domain. A sketch of the rotor-stator configuration is shown in figure 6.1. The two dotted lines indicate the locations of the sliding interfaces between the stationary and the rotating domains in the mesh.
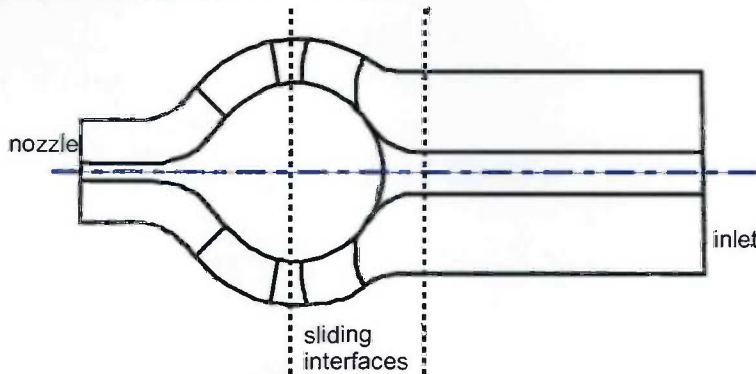

Figure 6.1   Sketch of rotor-stator pump configuration

The geometry of the impeller is based on seven blade profile sections equally spaced in radial direction and the blade root fillet geometry. The blade profiles provide detailed information of the shape of the blade sections near the leading and trailing edges. Figure 6.2 shows the blade geometry for two blades, based on the streamline profile sections.
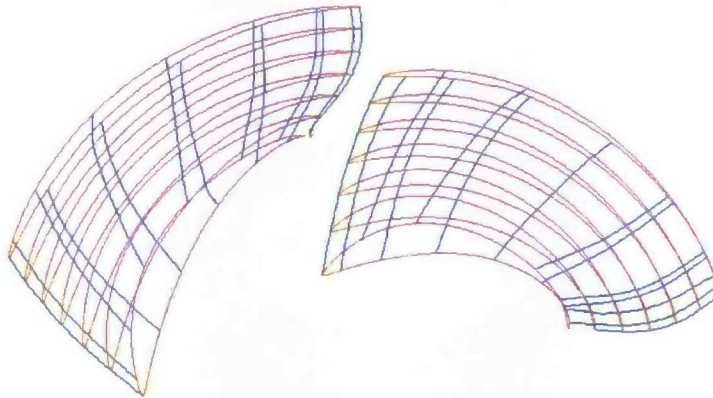

Figure 6.2   Blade geometry based on streamline profile sections

Around the cross-sections of the blades, an O-grid is used to ensure good orthogonality of the boundary layer cells along the impeller surface. These cells are also used in the region near the hub surface. The remainder of the volume between the impeller blades is filled with additional hexagonal cells.

The stator bowl is meshed with another group of hexagonal cells, which follow the guide vanes curvature. Thickness of the guide vanes is taken into account in the model. The shaft is included in the model at the suction side of the impeller, like in a real waterjet installation.

Figure 6.3 shows the topology of the mesh between two impeller blades in a plane at half-span and the block topology from hub to tip.

At the seatring, very fine cells are created from an extrusion layer. In this region high gradients occur due to the seatring being stationary with respect to the rotating unschrouded impeller. The layer of extruded cells fills the tip region between the impeller blades and the seatring. In this way, water can flow over the tip from pressure to the suction side of the blade. Treatment of the tip clearance is in agreement with the findings of several studies of turbo machinery addressing tip clearance flow phenomena [1-4].
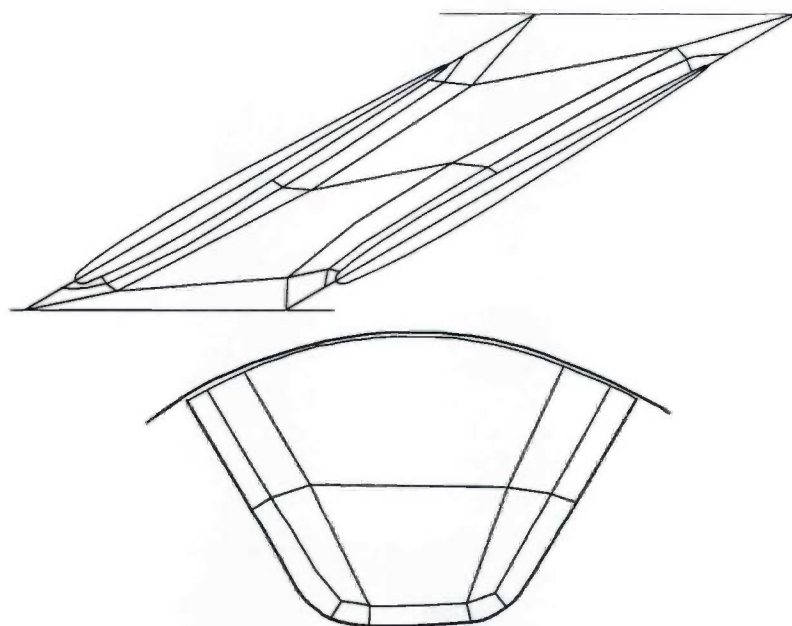

Figure 6.3   Mesh topology for the impeller of the mixed-flow pump in a plane at half-span (top) and in the direction from hub to tip

Figure 6.4 shows the surface plot of the impeller blades, the stator blades, the hub and the shaft. The final mesh of the complete mixed-flow pump is presented in figure 6.5. The total number of cells is about 950.000 for the complete mesh.

Figure 6.4   Surface plot of impeller blades, stator blades, hub and shaft

Figure 6.5   Complete mesh of the mixed-flow pump with about 950.000 cells (top) and surface mesh of the impeller

This mesh shows the straight suction pipe, the impeller and the stator with the nozzle. The surface mesh of the impeller is shown as well. The block topology of the mesh along the fillet can be recognized, to a certain extent in the detailed view of the impeller surface mesh.

6.2 Numerical approach

The description of the numerical approach is divided into three parts, first the applied boundary conditions are discussed, followed by the description of the fluid properties. Finally, the implementation of the impeller rotation is discussed.

6.2.1 Boundary conditions

The numerical domain of the mixed-flow pump is bounded by a number of surfaces at which different types of boundary conditions are imposed. In the inflow plane, an inlet type boundary condition is applied. This requires the prescription of the three velocity components and the properties of the turbulence model. The velocity distribution in the plane can be either constant or non-uniform. The two measured non-uniform velocity distributions as shown in figure 3.2 can be implemented using a Fourier-series approximation.

It was already mentioned in section 1.2 that the waterjet mixed-flow pump belongs to the group of internal flow machines. At the nozzle outlet plane two types of boundary conditions are available: normal outlet boundary condition or a prescribed static pressure condition. The normal outlet condition only prescribes the mass flow rate. The actual distribution of the axial velocity may be non-uniform over the exit plane.

The pressure condition is used with a prescribed constant value of the static pressure over the whole outlet plane in general. The actual behaviour of the waterjet pump can be modelled with a value of the static pressure equal to the ambient pressure at the nozzle exit. The computational method enforces conservation of mass and the resulting velocity distribution can be non-uniform.

A wall boundary condition can be applied to the remaining boundaries. The default wall boundary condition assumes zero velocity of the wall in normal and tangential direction (no-slip) in the computational frame of reference. Special attention is required in turbo machinery calculations for two types of wall boundary conditions: (i) stationary walls in a rotating frame of reference, as discussed in section 6.2.3 and (ii) rotating walls in the stationary frame of reference.

6.2.2   Fluid properties

The fluid properties are specified similar to the ones specified for the calculations of the flow through the waterjet inlet as discussed in section 5.3.2. The density and viscosity are taken constant for the fluid. Turbulence is modelled with the k-ε turbulence model.

6.2.3   Impeller rotation

The basic idea is to split the numerical domain into three different parts: stationary inlet part, a rotating impeller part and a stationary stator bowl part. Rotation of the impeller can be accounted for in two different ways: (i) a quasi-steady approach with a multiple-frames-of-reference (MFR) method, or (ii) a fully transient method with a mesh moving with the impeller and with sliding interfaces with the stationary part of the mesh.

The MFR method is a relatively fast method, which can be used with a steady-flow solution method. This method is identical to the method used for the waterjet inlet flow calculations. In a rotating frame of reference rotation of the impeller results in centrifugal and Coriolis forces on the fluid elements. These are implemented by additional source terms in the momentum equations.

In case of a moving mesh with a sliding interface, a fully transient flow solution method is required. The CFD method provides a routine, which automatically rotates the mesh after each timestep and connects the rotating and stationary domains. Fully transient flow calculations use the PISO (Pressure Implicit with Splitting of Operators) algorithm to couple the momentum and pressure terms. This algorithm was originally developed for the non-iterative computation of unsteady compressible flow [5]. It involves one predictor step and two or more corrector steps, which may be seen as an extension of the SIMPLE algorithm with additional corrector steps.

All calculations presented in this chapter have been made for an impeller rotational speed of 1920 RPM, (32 Hz). Reynolds numbers based on inlet pump diameter and rotational speed (according to equation (4.1)) are in excess of 10^7. Note that full scale waterjet installations normally operate at Reynolds numbers which are 3 to 5 times larger.

6.2.4   Calculation of global pump performance

Pump head

By definition, pump head is based on the difference in total pressure upstream and downstream of the pump (see (2.32)). These values can be derived from the CFD results by integration of the total pressure over a cross-

sectional area upstream and downstream of the impeller. It follows from the energy balance, that mass averaged quantities are to be used to determine the total pressure:

$$\overline{p_{tot}} = \frac{1}{\rho Q} \int_A \rho p_{tot} v_n dA \tag{6.1}$$

where A denoting the cross-sectional plane. The actual mass averaged head H_{ma} is calculated as:

$$H_{ma} = \frac{\overline{p_{tot,out}} - \overline{p_{tot,in}}}{\rho g} \tag{6.2}$$

In an experimental set-up it is common practice to divide the total pressure into a static and a dynamic pressure component. Static pressure is measured at the inlet and outlet pipe circumference through pressure taps. Estimation of the dynamic pressure contribution is based on the inlet and outlet pipe diameter and the volume flow through the pump. Within this approach it is assumed that the velocity and pressure distributions are uniform over the measurement planes, and that there are no significant velocity components in the tangential and radial direction (i.e. swirl).

The calculation of the head from the CFD calculations can also be based on the static pressure distribution and the flow rate. The area-averaged static pressure is calculated according to:

$$\overline{p_{stat}} = \frac{1}{A} \int_A p_{stat} dA \tag{6.3}$$

where A represents the cross-sectional area. It is acknowledged, that in actual experiments, the static pressure is only measured at the outer radius and subsequently averaged. This difference is neglected in the analysis. The area-averaged head becomes:

$$H_{aa} = \frac{\overline{p_{stat,out}} - \overline{p_{stat,in}}}{\rho g} + \frac{Q^2}{2g}\left(\frac{1}{A_{out}^2} - \frac{1}{A_{in}^2}\right) \tag{6.4}$$

There are therefore two expressions for the head of the pump: the correct value H_{ma}, based on a mass average, and an estimated value H_{aa}, based on area averages. The non-uniformity of the axial inflow velocity is taken into account with the mass averaged method correctly, but not with the area averaged method.

Shaft torque

In an experimental set-up, shaft torque can be measured with strain gauges on the shaft. The measured torque can be corrected for additional friction losses in seals and bearings. In the CFD calculations torque can be determined in two ways. The first method is based on a direct summation of wall forces acting on the impeller and shaft surface. The second method is based on a momentum balance in circumferential direction. The equation for the moment of momentum is given by (see for example [6]):

$$\underline{T}_{shaft} = \frac{\partial}{\partial t} \int_{CV} \underline{r} \times \underline{v} \rho dV + \int_{CS} \underline{r} \times \underline{v} \rho \underline{v} \cdot d\underline{A} - \int_{CS} \underline{r} \times \underline{\tau}_w \qquad (6.5)$$

where CV represents the control volume and CS all surfaces of the control volume, $\underline{r}$ is the distance from the axis of rotation, $\underline{v}$ is the velocity and $\underline{\tau}_w$ the viscous stress tensor. In general turbo machinery applications, the axial component of this vector equation has to be evaluated only. For steady flow conditions the equation for moment of momentum reduces to:

$$T_{shaft} = \int_{CS} \rho r v_t v_n dA - \int_{CS} r \tau_{w,t} \qquad (6.6)$$

where v_t is the circumferential velocity component, v_n the normal velocity at control surfaces and $\tau_{w,t}$ the tangential shear force at the surfaces of the stationary housing. This force will be a result of the shear forces acting on the surface of the so-called seatring. Evaluation of the first term on the right hand side of equation (6.6) can be limited to the surfaces through which the flow enters and leaves the control volume, since the normal velocity vanishes at wall surfaces. The actual equation for the determination of the torque within the numerical method becomes:

$$T_{shaft} = \int_{A_{out}} \rho r v_t v_n dA - \int_{A_{in}} \rho r v_t v_n dA - \int_{A_{seatring}} r \tau_{w,t} \qquad (6.7)$$

6.3 Validation with experimental data

The numerical method used to compute the flow in the waterjet mixed-flow pump is validated with the aid of experimental data of pump performance. Extensive series of measurements have been made on a model-scale pump at the authors' company. The experimental data include the head and torque curves as a function of flow rate. The pump performance data is used in the waterjet performance prediction software of Wärtsilä Propulsion Netherlands

BV. The performance prediction software has been used for the prediction of all full scale installations, which are currently in service.

Flow rate and head are expressed as non-dimensional quantities with equations (2.15) and (2.16) respectively. Torque is presented as a non-dimensional quantity as well. This is similar to the torque coefficient Kq used for propellers. The non-dimensional torque is defined as:

$$T^* = \frac{T}{\rho \Omega^2 D^5} \tag{6.8}$$

Pump efficiency is derived from the values for the flow rate, head and torque, based on equation (2.20).

6.3.1   Quasi-steady flow calculations with the MFR method

Results of CFD calculations with the method using the quasi-steady multiple frame of reference approach are presented in this section.

Head curve

First the head curve based on the CFD calculations will be compared with the experimental data. Figure 6.6 shows the dimensionless head curves from the measurements and the calculations. The calculated head is based on equations (6.2) and (6.4). The presented head curves are normalised with a constant given flow rate and pump head of the design condition. Agreement between the calculations and the experimental data is good over a large range of flow coefficients.

Differences between the two methods to determine the head from the CFD results are limited to the low flowrate conditions. Near the design point the deviations between the two approaches are negligible. The differences between the two methods at low flow rates can be attributed to a non-uniform velocity distribution at the outlet.

The numerical results are used to express the differences between mass averaged and area averaged determination of the head. These calculations are based on a pump configuration with a nozzle, which has ambient pressure at the exit area. The measurements are made in a closed-loop system however. The measured head will give the correct value, corresponding with the mass averaged numerical prediction, when the static measurement locations are located sufficiently far upstream and downstream of the pump to ensure uniform velocity distributions at those locations.
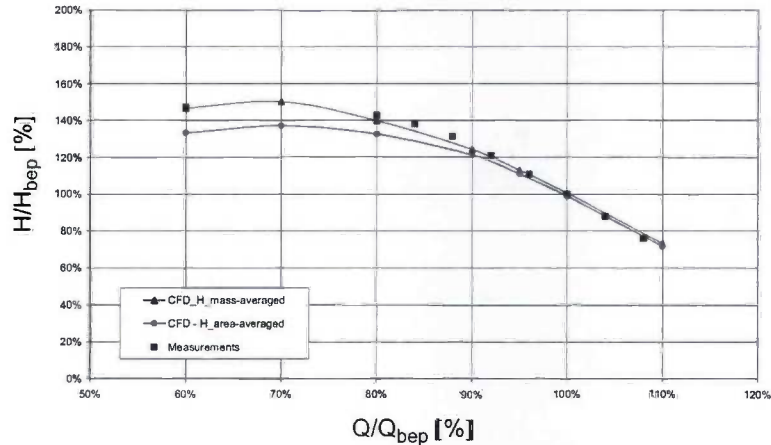
*Figure 6.6   Comparison of measured and calculated head curves, based
on equations (6.2) and (6.4).*

Gülich *et al* [7] show the obtained accuracy of calculated pump head for a
large number of different pumps with a RANS method. Comparisons with
measured data show deviations up to about 4% for mixed-flow type pumps.
Deviations of 5% in head prediction are also presented for a complete stage
of a boiler feed pump [8]. The currently found deviations between
measurements and calculations are of the same order or smaller. It can be
concluded that the prediction of head with the CFD method is sufficiently
accurate for further analysis of the complete waterjet installation in chapter 7.

Shaft torque

A comparison of the calculated and measured shaft torque is shown in figure
6.7. Calculation of torque is based on the integration of the wall forces and on
the moment of momentum balance (equation (6.7)). Differences between the
results of the two numerical methods are negligible for all conditions.
Agreement between the numerical results and the measured data is
acceptable over the whole range of analysed conditions.

The magnitude of the differences appears to be related to the flow rate,
where an under-estimation is observed at low flow rates and an over-
estimation at high flow rates. The differences are limited to a few percent at
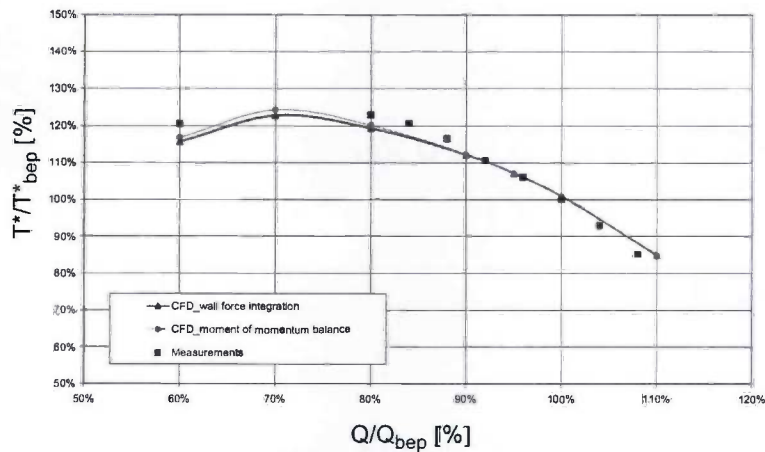most, however, in the range considered.

Figure 6.7   *Comparison of measured and calculated shaft torque based on integration of wall forces and moment of momentum balance*

Efficiency

The efficiency of a pump has been defined in equation (2.20) as the ratio of the hydraulic power and the shaft power. Hydraulic power is the product of volume flow rate and the produced pressure head. Shaft power is the product of torque and the impeller angular speed. Based on the graphs of head and torque, it is to be expected that the calculated pump efficiency will show some deviations compared to the experimental data.

Figure 6.8 shows the calculated and the measured normalised efficiency of the pump. The calculated efficiency is based on the head according to equation (6.2), and the torque based on integration of the wall forces. The pump efficiency is normalised with the efficiency at the design point.

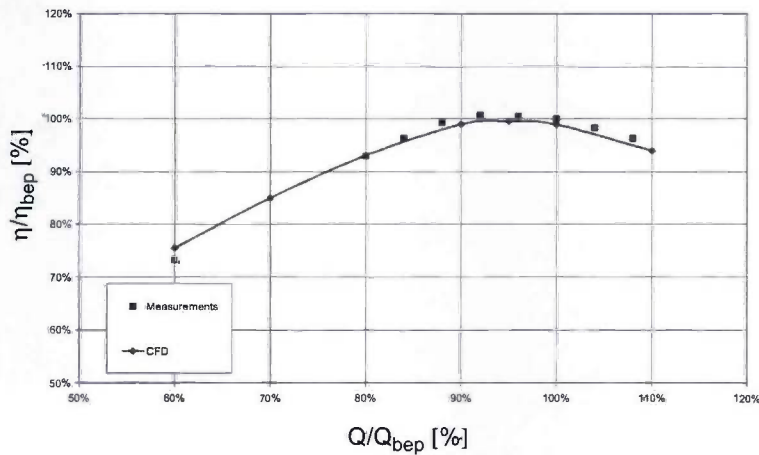The deviation between the calculated and the measured efficiency is about 1% near the design flow rate.

Figure 6.8   Comparison of measured and calculated pump efficiency.

6.3.2   Transient flow calculations with moving mesh

Apart from calculations with the MFR method for quasi-steady flow, calculations have been made with the method for fully transient flow, including the moving mesh option. With this method the actual movement of the rotor with respect to the stator blades is taken into account. This enables a detailed analysis of the interaction forces between the rotor and the stator.

Evaluation of convergence behaviour

In a fully transient flow calculation it takes a number of impeller revolutions before the solution becomes periodic. The level of periodicity of the flow field is monitored at some monitoring points in the numerical domain. Three points are located about half a diameter upstream of the impeller in the inlet pipe and three points are located in between the rotor and stator blades in the stationary part of the mesh. The locations of the three points are chosen arbitrarily.

The flow field variables at the monitoring points between the impeller and the stator blades should give a periodic solution with a frequency equal to the impeller blade passing frequency. Figure 6.9 shows the axial velocity at the monitoring points for the design flow condition during the fifth revolution of the impeller. The axial velocity has been normalised with the mean axial velocity.
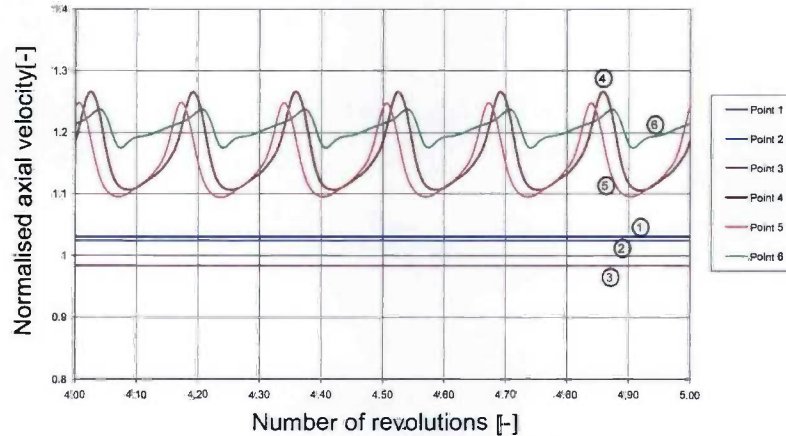
Figure 6.9   *Normalised axial velocity at monitoring points during fifth impeller revolution for design condition. Points 1,2 and 3 are located upstream of the impeller, points 4,5 and 6 are located in between the impeller and stator.*

For the monitoring points upstream of the impeller constant values can be observed, due to the prescribed axial inflow velocity. Downstream of the impeller a periodic solution is found for all three monitoring points. The average value and the amplitude depend on the location of the monitoring points. The signal shows that during the fifth revolution of the impeller the signal is periodic with frequency equal to the blade passing frequency (BPF).

The fluctuating pressure coefficients at the monitoring points is shown in figure 6.10. The pressure coefficient is defined as:

$$C_p = \frac{p_{stat} - p_0}{\frac{1}{2}\rho\Omega^2 D^2} \tag{6.9}$$

where p_0 is the reference pressure at the nozzle exit plane, ρ the density, Ω the shaft speed and D the diameter of the inlet.

The monitoring points downstream of the impeller show the expected periodic behaviour of the pressure. The monitoring points upstream of the impeller show fluctuations also containing higher frequencies. Pressure fluctuations at the inlet side are related to the choice of the boundary conditions at both the inlet and outlet boundary. The constant pressure boundary condition implies the pressure being steady at the nozzle exit surface. As a consequence, any fluctuation in the overall pressure head is experienced at the inlet. On the
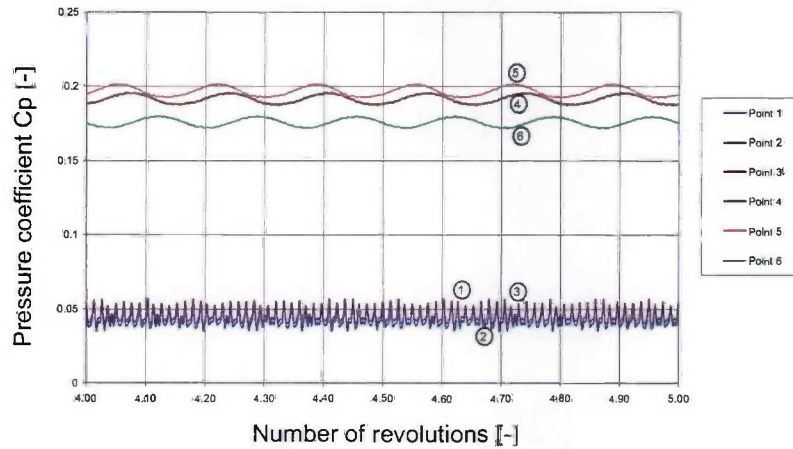
*Figure 6.10   Static pressure coefficient at monitoring points during fifth
impeller revolution for design condition. Points 1,2 and 3 are
located upstream of the impeller, points 4,5 and 6 are located
in between the impeller and stator.*

other hand, in an actual pump, small fluctuations in mass flow will be present,
which may limit the high frequency pressure fluctuations. In the calculations
the mass flow rate is a constant prescribed value due to the prescription of a
fixed velocity at the inlet side.

Evaluation of the periodic behaviour of the solution is based on a Fourier-
transformation of the fluctuations. Figures 6.11 and 6.12 show the Fourier
transforms for both the axial velocity and the pressure at the design flow rate
condition for the monitoring points, which are located downstream of the
impeller, i.e. in between the impeller and the stator.

The peaks at the impeller-blade passing frequency and its higher harmonics
can be recognised easily. The Fourier transformations show a clear harmonic
solution downstream of the impeller for both the axial velocity as well as the
static pressure. Results of the Fourier analyses for other flow rates are
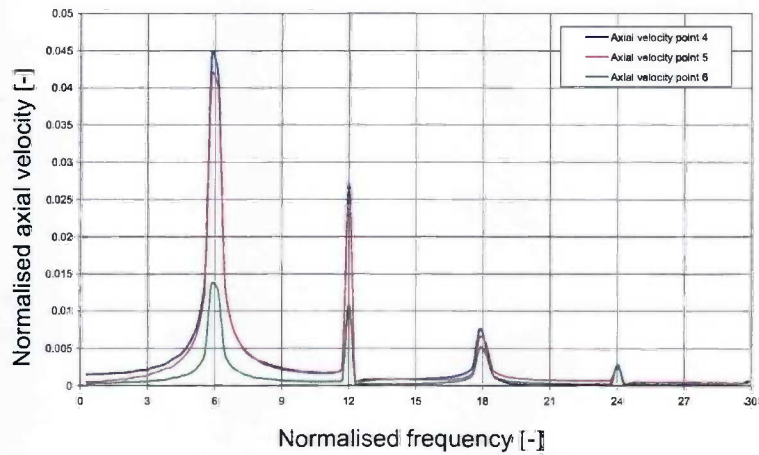presented in Appendix B.

Figure 6.11   *Fourier-transform of fluctuating normalised axial velocity at monitoring points at location in between the impeller and stator. Frequency is normalised by the shaft frequency*
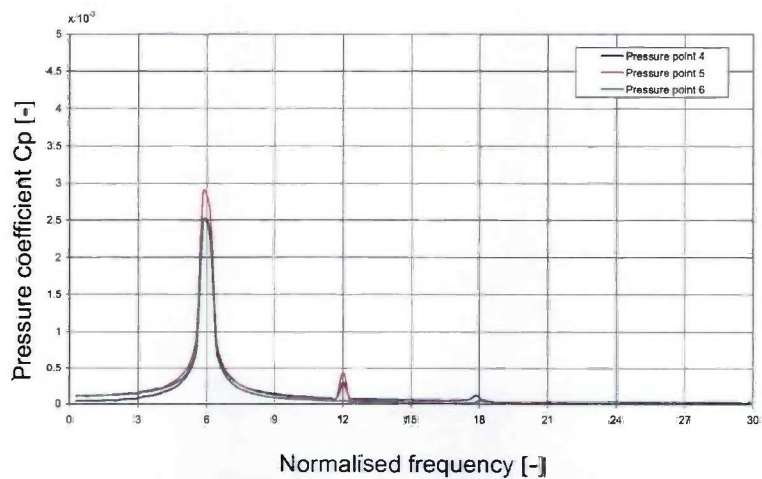

Figure 6.12   *Fourier-transform of fluctuating static pressure coefficient at monitoring points at location in between the impeller and the stator. Frequency is normalised by the shaft frequency.*

Performance diagrams

Transient flow calculations have been made for a number of flow rates. The pump performance parameters, like head and torque are averaged over a number of timesteps.

Figure 6.13 shows the mass averaged head curve based on equation (6.2) for both the quasi-steady and the transient flow calculations. The experimental data is plotted as reference.The results for the head curves based on the area averaged quantities, according to equation (6.4), is shown in figure 6.15.

Both methods show the tendency of a slight increase of the head for the transient flow calculations. This phenomenon is also observed in calculations based on a potential flow method by Van Esch [9]. Agreement with the experimental data is still acceptable for both the quasi-steady and the transient flow calculations.

The comparison for the impeller torque is shown in figure 6.14. Both numerical methods as well as the experimental data are shown in this figure. A similar trend is seen for the torque as for the head, where transient flow results show slightly higher values. The efficiency of the pump is shown in figure 6.16 for the quasi-steady and transient flow calculations. This efficiency is based on the mass averaged head. It is observed that the transient flow calculations predict a small increase of efficiency compared to the quasi-steady flow results.
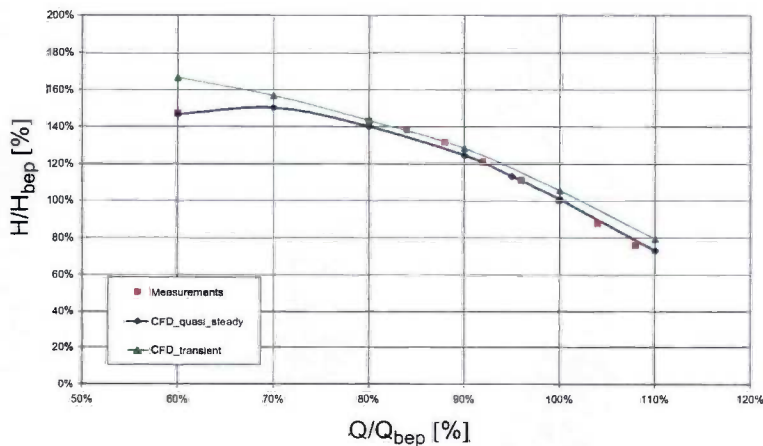

Figure 6.13   Comparison of results of quasi-steady and transient flow
calculations of mass averaged head based on equation (6.2)
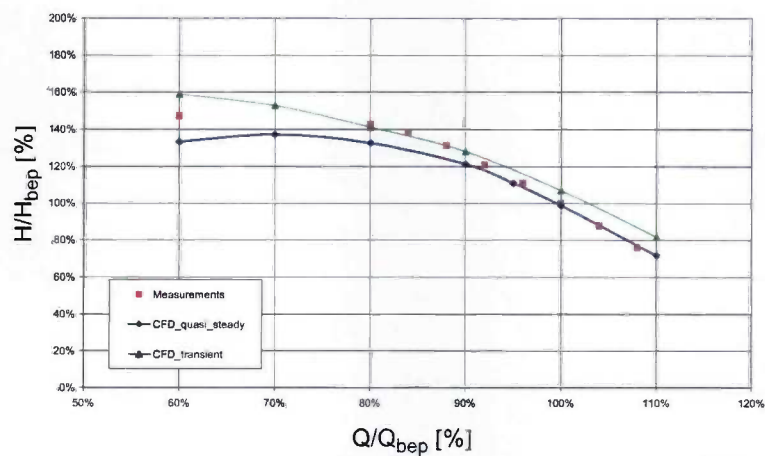
Figure 6.14   Comparison of results of quasi-steady and transient flow calculations of area averaged head based on equation (6.4)
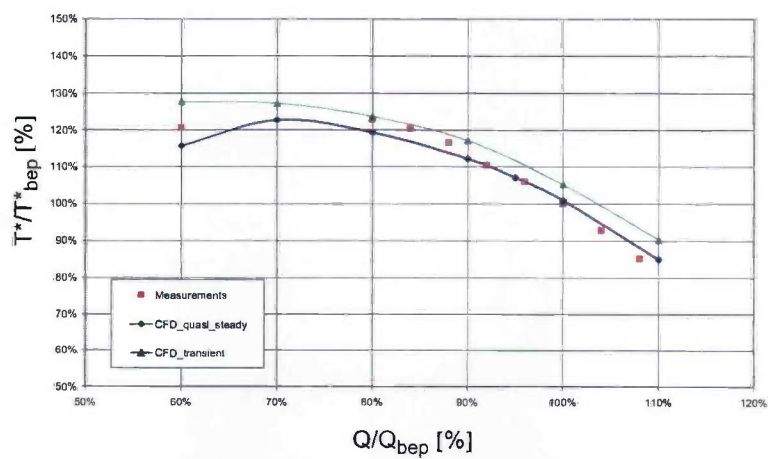

Figure 6.15   Comparison of results of quasi-steady and transient flow calculations of torque.
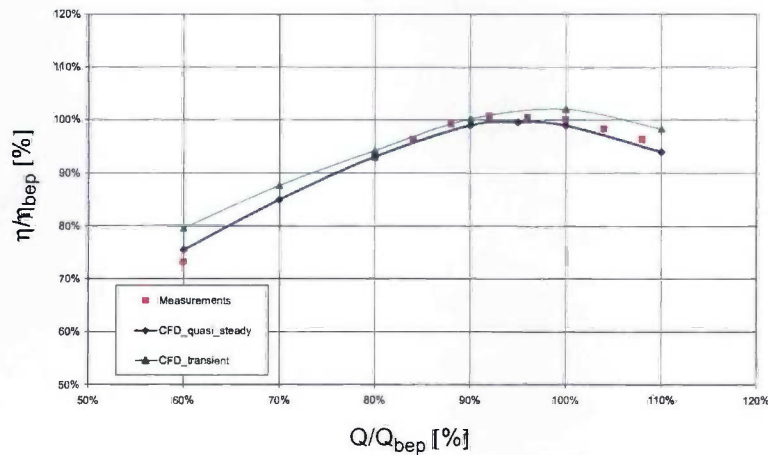
*Figure 6.16   Comparison of results of quasi-steady and transient
calculations flow calculations of efficiency*

6.3.3   Rotor-stator interaction forces

The fully transient flow calculations with the moving mesh can be used to
evaluate the radial force acting on the impeller due to rotor-stator interaction.
Given the number of rotor and stator blades, an estimation of the behaviour of
the interaction force can be made. The currently analysed configuration has
six rotor and seven stator blades. According to Brennen [10] and Dubas [11]
this should give a radial force counter rotating at the blade passing frequency.

The counter rotating force is derived from a model which is based on the
assumption of a variation in the pressure field when a rotating impeller blade
passes a stationary guide vane in the stator bowl. These fluctuations in
pressure distribution result in a fluctuating force on the impeller. Disturbances
in the symmetry of the blade pressure distribution will result in a radial force.
For this pump the angles between all the possible combinations of rotor and
stator blade pairs are determined and inserted in a 6x7 matrix. Such a matrix
can be used to determine the sequence in which stator blades encounter
passing rotor blades. The resulting matrix is shown in table 6.1.

Realizing that angular distances decrease during rotation of the impeller, the
sequence of stator blades with an impeller blade passing will be: 7 - 6 - 5 - 4 -
3 - 2 - 1. The resulting interaction force has thus a counter-rotating direction
compared to the impeller rotation and can possibly lead to backward whirling.

Table 6.1   Angular distance between rotor and stator blades for pump with 6 rotor blades and 7 stator blades

	Stator 1	Stator 2	Stator 3	Stator 4	Stator 5	Stator 6	Stator 7
Rotor1	**0.0**	**51.4**	102.9	154.3	205.7	257.1	308.6
Rotor2	300.0	351.4	**42.9**	94.3	145.7	197.1	248.6
Rotor3	240.0	291.4	342.9	**34.3**	85.7	137.1	188.6
Rotor4	180.0	231.4	282.9	334.3	**25.7**	77.1	128.6
Rotor5	120.0	171.4	222.9	274.3	325.7	**17.1**	68.6
Rotor6	60.0	111.4	162.9	214.3	265.7	317.1	**8.6**

Figure 6.17 shows the force map for different flowrates. The forces are made non-dimensional to obtain the force coefficients Cf_x and Cf_y defined as:

$$Cf_x = \frac{F_x}{\rho\Omega^2 D^4} \qquad Cf_y = \frac{F_y}{\rho\Omega^2 D^4} \tag{6.10}$$

The two force components are combined to get the radial force component Cf_{r1}:

$$Cf_{r1} = \sqrt{Cf_x^2 + Cf_y^2} \tag{6.11}$$

During the calculations, output is generated with a frequency of 960 Hz, which is equivalent to five times the blade passing frequency. The amount of scatter of the force signal at each of these five points in subsequent cycles gives an indication of the higher order fluctuations in the solution. The time-averaged magnitude of the radial force Cf_{r1} for each flow rate is plotted as a circle in the force map.

The forces show a periodic behaviour for all flow rates. The centre of the concentric circles, which represent the time-averaged magnitude of the force, is located at the impeller axis. This means that the time-average of both the horizontal component Cf_x as well as the vertical component Cf_y of the interaction force diminish. This is in accordance with the expectations, given a situation with uniform axi-symmetrical inflow and outflow.

The average of the blade interaction force has a minimum value at the design condition, denoted as 100% flow rate. This quantity increases with decreasing flow rate. However, at 60% of the design flow a significant reduction of the magnitude of the radial force is observed. This effect can be observed more clearly in figure 6.18, where the time averaged magnitude Cf_{r1} of the rotor-

stator interaction force and the corresponding standard deviation are plotted as function of the flow rate. The standard deviation shows a minimum near the design point, which is in agreement with the expectations.
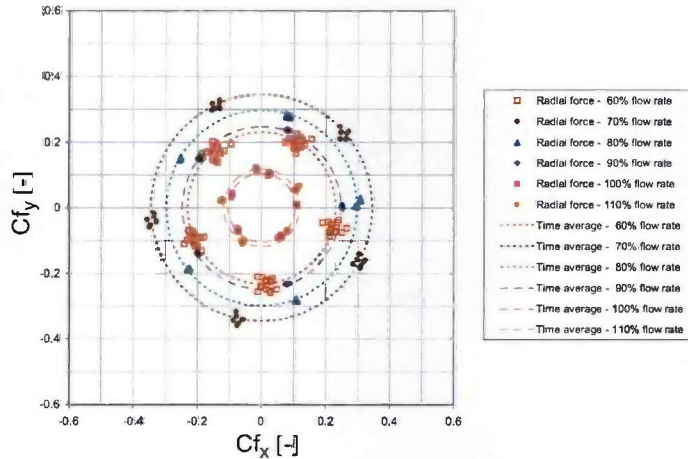

Figure 6.17   Plot of rotor-stator interaction force for different flow rates: instantaneous values (markers) and time-average of magnitude of force coefficient (dotted curves)
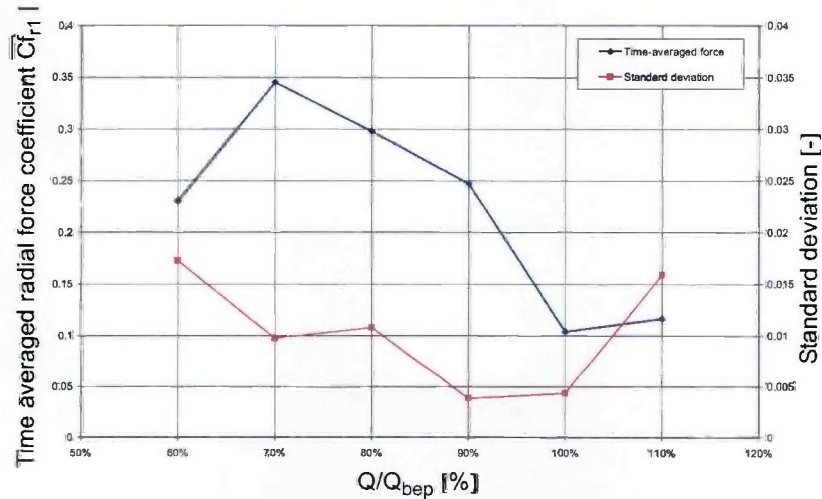

Figure 6.18   Time averaged rotor-stator interaction force coefficient Cf_{r1} and standard deviation as function of the flow rate

Model scale measurements on the same waterjet pump have confirmed the presence of multiple local minima and maxima of the radial force [12]. These results have not been published yet.

6.4 Influence of non-uniform axial inflow

The results discussed in the previous section are obtained for uniform inflow velocity distributions. Waterjets operate in a strongly non-uniform inflow distribution as described in chapter 3. The effect of a non-uniform velocity distribution on the pump performance and the impeller forces will be investigated in more detail in this section. Four distributions are used in the analysis, the measured distributions are shown in given in figures 5.13a to 5.13d. The non-uniform velocity distributions are imposed as boundary condition in the numerical analysis with the aid of a Fourier series approximation of the velocity distribution, according to equation (3.2).

All calculations performed with the non-uniform inflow distribution are carried out with the transient moving mesh option of the CFD method. Results of the transient flow calculations for uniform inflow show a radial force due to rotor-stator interaction. This force originates from the interaction between the impeller trailing edge and the statorblade leading edge. With a non-uniform inflow velocity distribution, an additional source for a radial force is introduced, since the velocity distribution is not axi-symmetric.

First the pump performance for the non-uniform inflow conditions will be reviewed. In the remainder of this section the effects of the inflow on the radial forces will be analysed.

6.4.1 Pump performance for non-uniform inflow

The calculations with uniform inflow velocity already showed an interesting difference between the two methods for the determination of the pump head based on either mass-averaged or area-averaged quantities. For the calculations for non-uniform inflow velocity distributions, the differences between the results of these two methods may increase even more. Tables 6.2 and 6.3 show the normalised pump performance for four different inflow conditions. The flow rate for all calculations is equal to the design flow rate. The values in the tables have been normalised with the result from the corresponding calculation with a uniform inflow distribution and design flow rate of 100%.

The results of the method based on the mass-averaged total pressure are shown in table 6.2. It can be observed that the variations in both head and torque are limited to less than two percent for all inflow conditions. The efficiency shows a small decrease for increasing non-uniformity.

On the other hand, the results as shown in table 6.3, are in disagreement with the general expectation. A clear increase of the pump head and consequently the efficiency is found with increasing non-uniformity. Although an efficiency increase has been reported by Kooiker *et al.* [13], who claim an increase of 5% due to non-uniform inflow, this is (at least partly) a result of the way in which the pump head is measured. From equation (6.4) it is clear that the averaging of a non-uniform inflow velocity distribution will underestimate the suction head, which results in a higher estimate of the produced head by the pump. Therefore, it is concluded that the method of area-averaged head determination is invalid for non-uniform velocity distributions.

The actual pump performance shows only a small decay due to the non-uniform inflow velocity distribution. This deviation can be neglected for practical non-uniform inflow distributions.

Table 6.2   Normalised pump performance based on mass averaged head (equation (6.2)) for various inflow distributions, related to IVR.

IVR [-]	$H_{ma}/H_{ma\_uniform}$ [%]	$T^*/T^*_{uniform}$ [%]	$\eta/\eta_{uniform}$ [%]
1.68	101.0	101.7	99.6
1.87	101.0	101.6	99.7
2.03	100.1	101.5	99.0
2.19	100.0	101.4	98.8

Table 6.3   Normalised pump performance based on area averaged head (equation (6.4)) for various inflow distributions, related to IVR.

IVR [-]	$H_{aa}/H_{aa\_uniform}$ [%]	$T^*/T^*_{uniform}$ [%]	$\eta/\eta_{uniform}$ [%]
1.68	103.0	101.7	101.2
1.87	103.5	101.6	101.9
2.03	104.3	101.5	102.7
2.19	105.3	101.4	103.8

6.4.2   Background of radial forces acting on the impeller

Steady fluid-induced radial forces can be generated by a non-uniform pressure distribution at the impeller periphery or by an imbalance in the blade torque. The first phenomenon is known to occur in centrifugal pumps with a spiral volute casing (see [14]-[16]). The tongue introduces a clear asymmetry
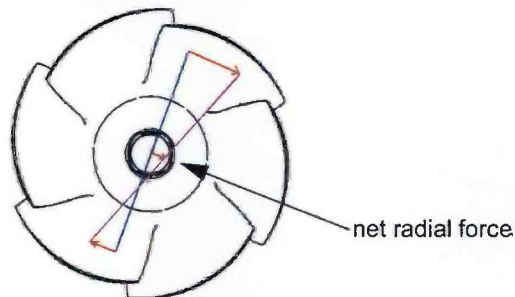
Figure 6.19   Concept of radial force due to unbalanced blade torque

in the geometry. Waterjet installations with a stator bowl do not suffer from such type of a-symmetry, however. This source for a radial force can therefore be excluded. The non-uniform inflow velocity may create a non-symmetrical pressure distribution on the hub surface. This may result in a net radial force.

Imbalance in blade torque may give a more significant contribution to the radial forces acting on the impeller. The concept of this imbalance is shown in figure 6.19.

Non-uniformity of the inflow velocity distribution will result during a revolution in variations of both the flow angle at the leading edge and the flow rate through an impeller channel. This will result in a torque contribution that is different for each blade. The difference in torque contributions between two opposite blades will result in a net radial force on the impeller axis.

6.4.3   Flow rate fluctuations in the impeller channel

The CFD results are used to determine the local flow rate Qbb through the impeller channel between two consecutive blades. The volume flow rate is determined at a cross-sectional plane at mid-chord of the impeller blades. Figure 6.20 shows the normalized local flow rate as a function of the rotor position for the four different inflow conditions.

Even for the case of maximum level of non-uniformity, i.e. for IVR=2.19, the maximum deviation is less than 7% of the average. The variations obtained from the CFD results are much smaller than the predictions based on the analytical approach used in section 3.2. It appears that the non-uniform inflow velocity distribution is smoothed in the first part of the pump. This will influence the local flow angles at the leading edge of the impeller blade. As a consequence, the blade loading and the blade torque will be influenced. This eliminates the possibility to derive a simple analytical model to estimate the radial and tangential forces on the impeller.
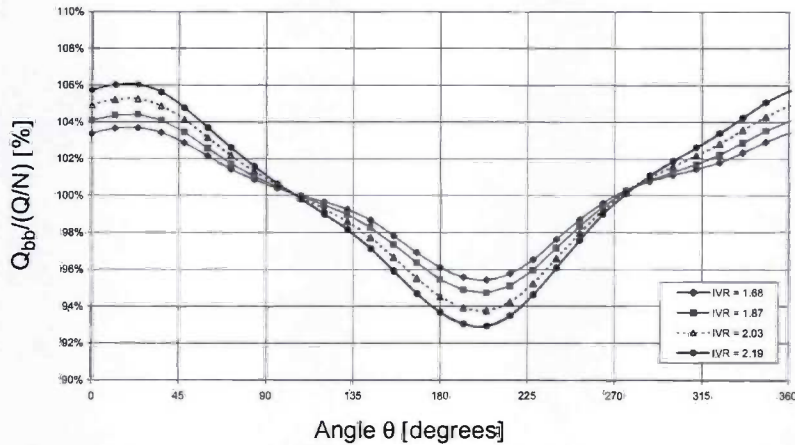
Figure 6.20   Normalised channel flow rate Qbb as a function of the rotor position for various inflow distributions, which are related to the IVR

6.4.4   Radial forces for non-uniform inflow

The non-uniform inflow velocity distribution has an effect on the radial forces acting on the impeller. For a uniform inflow distribution a periodic rotor-stator interaction force is found, as shown in subsection 6.3.3. In this section the forces are evaluated that are caused by the non-uniformity of the inflow.

Figure 6.22 shows a graph of the horizontal and vertical component of the force acting on the impeller for different IVR, each with a typical non-uniform inflow velocity distribution, at the design flow rate.

The forces acting on the impeller can be approximated by a mean component Cf_{r0} and harmonic components Cf_{r1} and Cf_{r2}:

$$Cf_r = Cf_{r0} + Cf_{r1} \cdot \omega t + Cf_{r2} \cdot 2\omega t \qquad (6.12)$$

This is shown in a sketch in figure 6.21 for the mean component Cf_{r0} and the first harmonic Cf_{r1}.
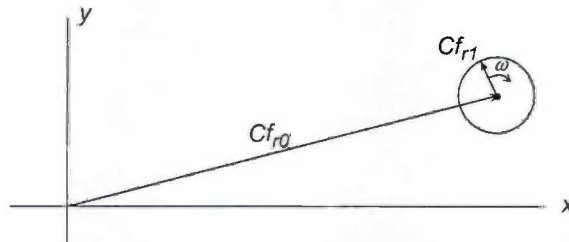
Figure 6.21   Sketch of radial forces acting on the impeller due to non-uniform inflow.

From the results as presented in figure 6.22 can be seen that the mean radial component Cf_{r0} shows a strong relation with the level of non-uniformity, which is in accordance with expectations. The direction of the mean force seems to be constant for all inflow conditions. This direction may be related to the flow rate through the pump, which is equal for all presented conditions in figure 6.22.

The condition with the most severe non-uniform velocity distribution (IVR = 2.19) shows quite some scatter of the time dependent force. This seems to be an indication of higher order harmonics (i.e. Cf_{r2} and Cf_{r3}) in the system at these inflow conditions.

Figure 6.22   Horizontal and vertical component of time-dependent impeller force coefficient for different inflow velocity distributions, which are related to IVR, at design flow rate

Figure 6.23 shows the plot of the forces for 80% of the design flow rate. The occurrence of increasing mean force Cf_{r0} with increasing non-uniformity is confirmed. The magnitude of both the mean force Cf_{r0} and the first harmonic Cf_{r1} are different compared to the results for 100% flow rate. Moreover, the direction of the steady force has changed for this flow rate.
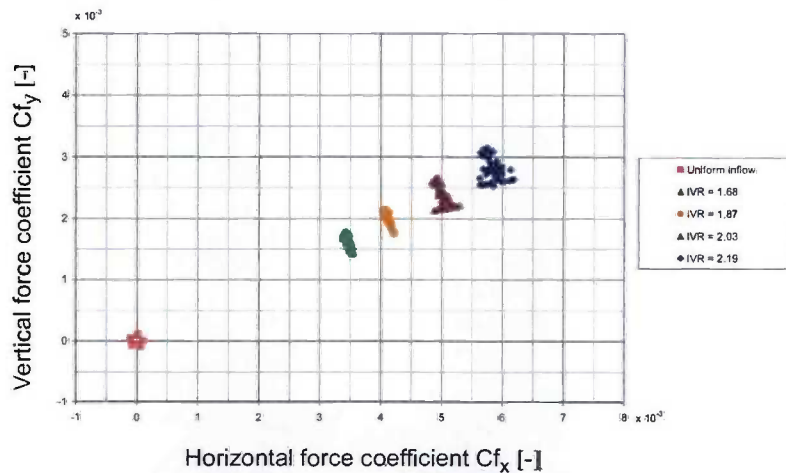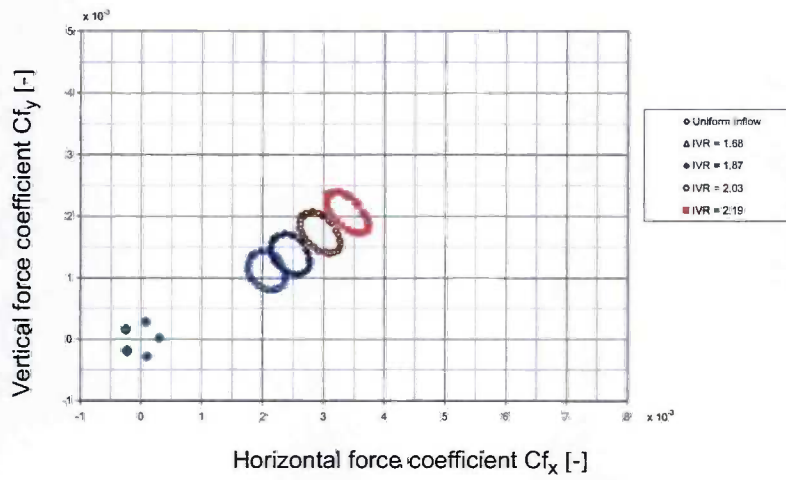

Figure 6.23   Horizontal and vertical component of time-dependent impeller force coefficient for different inflow velocity distributions, which are related to IVR, at 80% of the design flow rate

Analysis of mean radial force Cf_{r0}

The results of the calculations for different flow rates and levels of non-uniformities show that both parameters influence the mean radial force Cf_{r0}. A quantitative assessment is made in table 6.4, where the time averaged magnitude and the direction of the non-dimensional radial force are listed. The direction angle α is calculated according to:

$$\alpha = atan\left(\frac{\overline{Cf_y}}{\overline{Cf_x}}\right)$$

(6.13)

The direction of the radial force shows a small increase with increasing non-uniformity. Results at the design capacity show a variation of less than 1.5 degrees. On the other hand, the differences due to variation in flow rate are significant. At an IVR of 2.03 a deviation of 4.6 (= 30.5 - 25.9) degrees is found.

The variation in direction seems to be related to the flow rate. This may be due to an increase of the residence time of the fluid in the impeller, in which the impeller will rotate over a larger angle. The direction of the radial force will rotate accordingly.

Table 6.4   Time-averaged magnitude Cf_{r0} and direction α of radial force coefficient

Flow rate	IVR	$\overline{Cf_{r0}}$*1000	α
100%	1.68	3.819	24.9
100%	1.87	4.569	25.3
100%	2.03	5.550	25.9
100%	2.19	6.478	26.2
80%	1.68	2.368	28.9
80%	1.87	2.826	29.7
80%	2.03	3.423	30.5
80%	2.19	3.977	31.3

Analysis of unsteady forces

The unsteady radial force can be examined in more detail, if the mean force components Cf_{x0} and Cf_{y0} are subtracted from the results. The resultant of the vertical and horizontal component is plotted in figure 6.24 for the design flow rate and in figure 6.24 for 80% of design flow rate.

The results of the calculations with uniform inflow indicate a rotating radial force with a mean magnitude. The condition with the highest level of non-uniformity at design flow rate shows a chaotic behaviour of the unsteady forces. This is a result of higher order fluctuations of the forces.

At 80% of design flow rate, the behaviour of the fluctuating forces is more regular. Figure 6.24 shows that the shape of the locus of the force components becomes more and more elliptical, when the level of non-uniformity is increased. This means that the higher order harmonics of the radial force, i.e. Cf_{r2} and Cf_{r3}, become more important for these conditions.

This is confirmed by the Fourier transformation of the fluctuating component of the radial force, as shown in figure 6.26. The conditions at 80% of the design flow rate and at the design flow rate and moderate levels of non-uniformity show two clear peaks at one and two times the blade passing

frequency. The conditions at design flow rate and an IVR above 2 show numerous additional peaks at other frequencies. This is represented in the chaotic behaviour of the radial force.
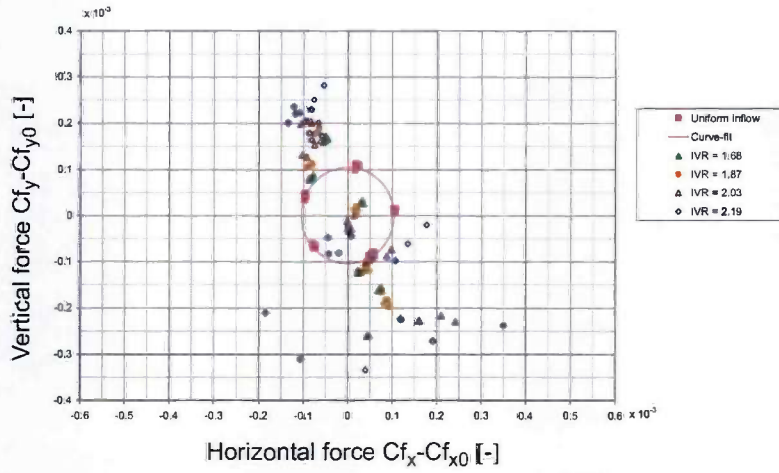

Figure 6.24   Unsteady impeller force components for different inflow velocity distributions at design flow rate.
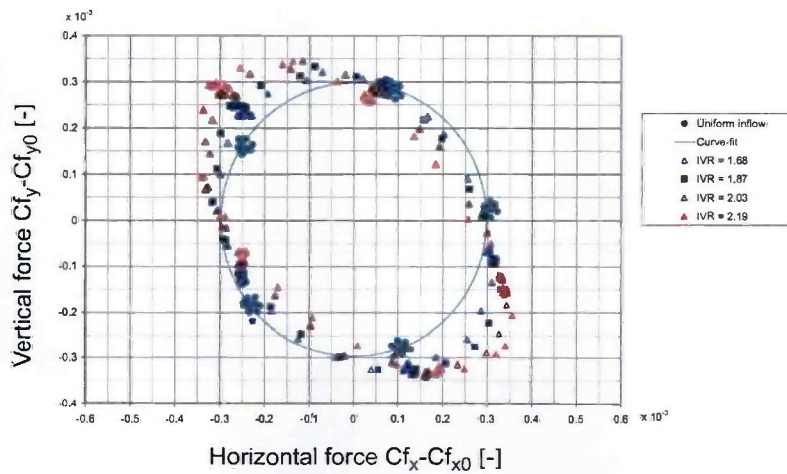

Figure 6.25   Unsteady impeller force components for different inflow velocity distributions at 80% of design flow rate.
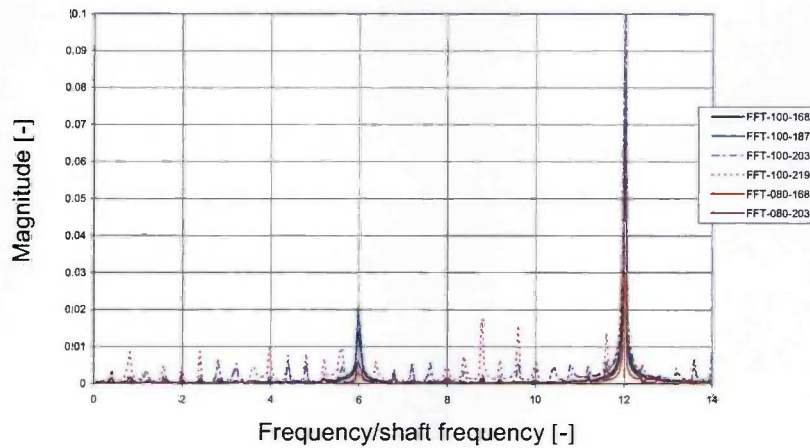
Figure 6.26   *Fourier transformation of the unsteady radial impeller force*
component (Cf_r - Cf_{r0}) for different inflow velocity distributions
and flow rates.

6.4.5   Concluding remark

The radial forces, which are presented in this chapter, are determined for an
impeller with a centred axis. This type of radial forces are also denoted as
excitation forces. In practice, the impeller will move away from its centred
position due to the radial forces. The off-centred motion of the rotating
impeller is called whirling [10]. This whirling motion of the impeller has not
been taken into account in the currently presented calculations, however. The
influence of the whirling motion on the occurrence of so-called reaction forces
has to be investigated further.

6.5   Nomenclature

A	area	m^2
Cf	force coefficient	-
Cp	pressure coefficient	-
D	diameter	m
F	force	N
F_s	surface shear force	N
g	gravitational acceleration	m/s^2

H	head	m
p_{stat}	static pressure	Pa
p_{tot}	total pressure	Pa
Q	flow rate	m^3/s
r	radial distance	m
T^*	torque coefficient	-
T	torque	Nm
v_n	normal velocity	m/s

Greek symbols

α	radial force direction	deg
ρ	density	kg/m^3
Ω	shaft speed	rad/s

Subscripts

in	inlet plane
n	normal direction
out	outlet plane
r0	mean component of radial force coefficient
r1, r2	harmonics of rotor-stator interaction force coefficient
t	tangential direction
x	horizontal direction
y	vertical direction

6.6 References

[1] Goto, A., 'Study of internal flows in a mixed-flow pump impeller at various tip clearances using three-dimensional viscous flow computations', Journal of Turbomachinery, Vol 114, pp. 373-382, 1992

[2] Nilson, H., Davidson, L., 'A numerical comparison of four operating conditions in a Kaplan water turbine, focusing on tip clearance flow', Proceedings 20th IAHR symposium, Charlotte, 2000

[3] Aschenbrenner, T., Göhringer, M., Moser, W., 'Numerical and experimental flow analysis in a Kaplan turbine', Proceedings 20th IAHR symposium, Charlotte, 2000

[4] Kunz, R.F., Lakshminarayana, B., Basson, A.H., 'Investigation of tip clearance phenomena in an axial compressor cascade using Euler and

Navier-Stokes procedures, Journal of Turbomachinery, Vol 115, pp. 453-467, 1993

[5] Versteeg, H.K. & Malalasekera, W., 'An introduction to Computational Fluid Dynamics', Longman Scientific & Technical, Essex, 1995

[6] Fox, R.W., & McDonald, A.T.,'Introduction to fluid mechanics', Third Edition, John Wiley & Sons, New York, 1985

[7] Gülich, J.F., Favre, J.N., Denus, K., 'An assessment of pump impeller performance predictions by 3D-Navier Stokes calculations', ASME Fluids Engineering Division summer meeting, 1997

[8] Cugal, M., Baché, G., 'Performance prediction from shutoff to runout flows for a complete stage of a boiler feed pump using computational fluid dynamics', ASME Fluids Engineering Division summer meeting, 1997

[9] Van Esch, B.P.M.,'Simulation of three-dimensional unsteady flow in hydraulic pumps', PhD thesis, University of Twente, 1997

[10] Brennen, C.E., 'Hydrodynamics of pumps', Oxford University Press, 1994

[11] Dubas, M., 'Über die Erregung infolge der Periodízität von Turbomachinen', Ingenieur-Archiv, vol. 54, pp. 413-426., 1984

[12] Esch, B.P.M. van, personal communication.

[13] Kooiker, K., Van Terwisga, T., Verbeek R., Van Terwisga, P., 'Performance and cavitation analysis of a waterjet system on a cavitation tunnel', proceedings FAST 2003 conference, session A1 pp 57-62, Ischia, Italy, 2003

[14] Stepanoff, A.J., "Centrifugal and axial flow pumps - Theory, design and application", 2nd edition, John Wiley, 1964

[15] Badie, R., "Analysis of unsteady potential flows in centrifugal pumps', PhD thesis, University of Twente, 1993

[16] Jonker, J.B. & Van Essen, T.G., 'A finite element pertubation method for computing fluid-induced forces on a centrifugal impeller rotating in a volute casing', International journal for numerical methods in engineering, Vol. 40, pp. 269-294, 1997

Chapter 7   Analysis of a complete waterjet installation

In the preceding two chapters the waterjet inlet and the mixed-flow pump were analysed separately. In this chapter the complete waterjet installation is considered. Results are presented of the numerical analysis of such a propulsion system on full scale. An analysis is made of the overall performance indicators, like volume flow rate, thrust and power. Comparisons are made with performance prediction and selection software of Wärtsilä Propulsion Netherlands (*WPNL-select*). This software is partially based on semi-empirical relations, which are tuned to the performance of the propulsion systems in the currently sailing fleet.

A detailed analysis of the streamtube will reveal some new insights into the forces acting on the installation in both vertical and axial direction.

7.1   Generation of the numerical model

The numerical domain of the complete waterjet installation is a combination of the two separate grids of the waterjet inlet and the mixed-flow pump. The interface between the two grids is located at the cross-section down-stream of the inlet bend (see figure 5.1 for the location of these parts). At this interface a coupling method is used to create a fully connected domain, based on arbitrary matching of the cells. It should be noted that this interface between the models of the inlet and the pump is different from the two sliding interfaces, which are required for the rotation of the impeller.

Care should be taken that the dimension of the nozzle exit area is equal to the exit area of the actual full-scale installation. The sensitivity of the flow rate
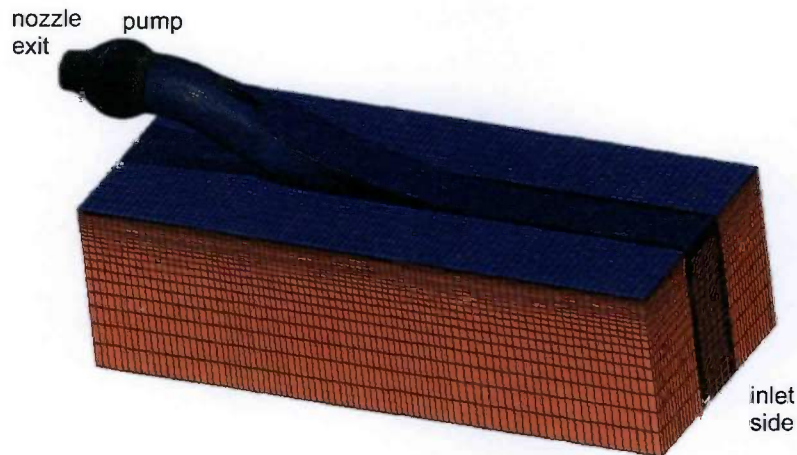
nozzle exit   pump

inlet side

Figure 7.1   Mesh of the complete waterjet installation, number of cells is about 1.2 million.

as function of the nozzle size has been illustrated in figure 2.8 on page 36. Figure 7.1 shows a plot of the final mesh of the full scale waterjet installation.

The boundary conditions and parameters of the numerical method are identical to the ones used for the calculations of the separate parts. At the inlet side of the domain a prescribed velocity distribution is applied, with a boundary layer velocity profile. At the other sides on the domain beneath the hull and at the nozzle exit plane constant pressure boundary conditions are applied. As a consequence, the actual flow rate through the waterjet becomes a part of the solution, whereas it was prescribed by the boundary conditions in the calculations for the isolated inlet and pump.

7.2   Evaluation of volume flow rate

The calculations are made with a constant rotational speed of the pump and a varying ship speed. In this way a relatively large range of IVR conditions is covered. The variation in volume flow rate will be much smaller, as indicated by the results presented in figure 2.9 on page 37.

The calculated volume flow rate through the waterjet is compared with the results of *WPNL-select*. To a large extent, this program is based on the theory as discussed in chapter 2. The loss coefficients in this method are empirical values taken from experimental data. Further fine-tuning is made with additional empirical data. The accuracy of the method is continuously increased by adding the measured performance of newly installed waterjet installations. Since the currently sailing fleet performs according to the

predictions, it is assumed that the accuracy of the performance prediction software is adequate.

It is shown in equation (2.52) that the thrust is related to the square of the volume flow rate. Consequently, a relatively small error in the prediction of the volume flow rate can lead to a large error in the thrust of the installation. It is believed that the prediction of thrust in *WPNL-select* is quite accurate, and consequently the prediction of the volume flow rate will be accurate as well.

Table 7.1   *Comparison of volume flow rate through waterjet based on prediction software and CFD calculations*

v_{ship} [kn]	Q_{select} [m³/s]	Q_{CFD} [m³/s]	Deviation [%]
31	13.0	12.93	< 1%
35	13.1	13.08	< 1%
39	13.3	13.19	< 1%
43	13.4	13.31	< 1%
47	13.6	13.49	< 1%

Differences between the results of *WPNL-select* and the CFD analyses are within 1%. According to the expectations, only a rather limited difference in volume flow rate is found between the low and high ship speed condition. This trend has been captured well by the numerical method.

Agreement is satisfactory and it appears that the numerical method is suitable for further use to investigate the flow phenomena in the waterjet installation.

7.3   Evaluation of waterjet thrust

The second quantity that can be compared with the results of *WPNL-select* is the thrust of the complete installation. The thrust can be determined from the CFD results by a summation of the forces acting on the solid walls or by the simplified momentum balance method given by equation (2.52) on page 33.

7.3.1   Integration of solid wall forces

The procedure for the selection of the cells at the solid walls requires some attention. It is possible to either select all solid wall cells of the numerical domain, or to select only the solid wall cells, that are part of the streamtube. The two options have been shown in figure 2.7 on page 31. With the selection of all wall cells of the numerical domain, a large part of the hull structure is also taken into account. The net thrust will be reduced due to the contribution of the drag of the hull.

Selection of the solid wall cells of the streamtube only, can not be done with a well-defined procedure, however. The wall cells near the streamtube surface will be partly included in the streamtube. The results show a significant influence of the choice whether these cells are included or excluded from the selection. The process of wall cell selection is avoided, when all solid wall cells of the numerical domain are taken into account in the force evaluation. The additional drag of the hull structure can be compensated for, given the dimensions of the numerical domain.

The method using drag compensation is also preferable from a ship builder's point of view. This is due to a subtle difference between a vessel with waterjet propulsion and a vessel with conventional propeller propulsion. For such a propeller ship, the hull and the propeller can be split into two subsystems. A waterjet propelled vessel can not be split into a bare hull and a propulsion unit, without leaving a hole in the hull structure. In a bare hull resistance test, additional hull drag, due to the development of the boundary layer, will be measured at the location of the inlet duct opening. The additional drag of the boundary layer will change once the waterjet installation with the inlet duct is installed.

It is concluded that the thrust of the installation has to be computed using all solid wall cells and that frictional resistance of the original hull area has to be compensated for. The total waterjet thrust is then:

$$T_{wj} = T_{wj,all} - D_{hull} \tag{7.1}$$

where $T_{wj,all}$ is the integrated force of the pressure and wall friction on all solid wall cells and D_{hull} the drag force of the equivalent rectangular hull area.

Calculation of the drag of the hull boundary layer is based on flat plate boundary layer theory for high Reynolds numbers. This formula is used, because it is also used to extrapolate model scale bare hull resistance data to full scale predictions. The friction coefficient is given by [1]:

$$C_f = \frac{0.455}{\log(Re_l)^{2.58}} \tag{7.2}$$

where the friction coefficient C_f is defined as:

$$C_f = \frac{D_{hull}}{\frac{1}{2}\rho v_{ship}^2 A_{hull}} \tag{7.3}$$

with D_{hull} the actual friction drag of the equivalent hull, v_{ship} the undisturbed velocity, and A_{hull} the area of the equivalent hull, which is length times width of the used mesh.

The Reynolds number for the flat plate is defined as:

$$Re_l = \frac{\rho v_{ship} L_{wetted}}{\mu} \tag{7.4}$$

where L_{wetted} is the wetted length of the hull upstream of the inlet. The actual drag of the hull area of the numerical domain depends on the dimensions of the area A and the wetted length of the hull upstream of the waterjet inlet.

7.3.2 Momentum balance

The thrust based on the momentum balance, can be calculated with the simplified equation (2.52). In this equation the contribution of the pressure distribution on the streamtube below the hull and the aft part of the hull is neglected. The introduced error can be compensated with the so-called thrust deduction factor t_j [2]. The mass averaged inflow velocity is determined using a concentration scalar as described in detail in section 5.5.

7.3.3 Results

Figure 7.2 shows the thrust of the full-scale installation based on *WPNL-select* and on the CFD calculations. In order to show the differences between results of the two methods that use the results of the CFD calculations, as described above, both results are presented in the graph. The results have been normalised with the design thrust at a ship speed of 39 knots.

The method of integration of the solid wall forces shows a very good agreement with the prediction software for the ship speeds up to 39 knots, which is the design speed for the investigated installation. At higher speeds a small difference is found between the results of the force integration method and the results of the prediction software.

The method based on the momentum balance gives a good agreement up to ship speeds of 35 knots. At higher speeds the momentum balance gives a lower thrust than the force integration and the prediction software.

The deviations between the results of the two numerical methods are quite significant at higher ship speeds. This phenomenon may be attributed to numerical inaccuracies.

However, it can also be an indication that the simplification of the momentum balance is the cause for this, as discussed in subsection 2.3.3 at page 30. It is known, that the low pressure region along the cutwater will have a positive contribution to the thrust. This may explain the deviations found between the results of the force integration method based on considering the pressure and shear stress on all solid wall cells and the ones of the momentum balance approach, which is applied to the streamtube.
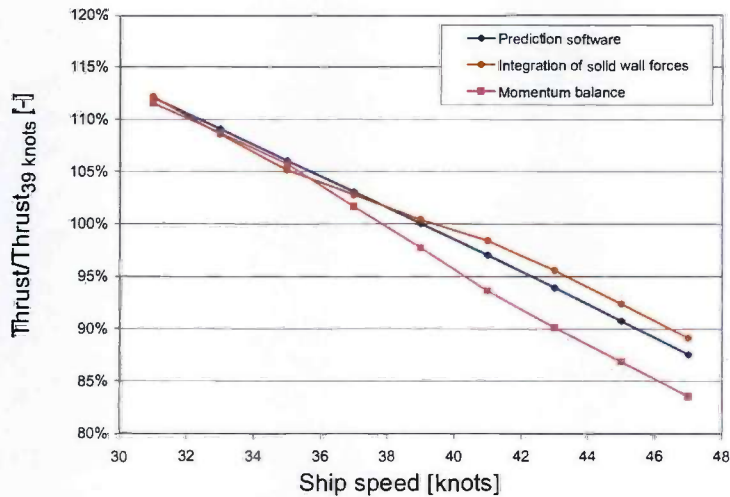
Figure 7.2   *Comparison of thrust of waterjet installation based on WPNL-select with numerical predictions based on force integration of solid wall forces (T_{wj}) and momentum balance applied to the streamtube (equation (2.52)).*

7.4   Evaluation of required power

Evaluation of the required power is equivalent to the evaluation of the required torque, since all calculations have been made at the same rotational speed. The torque is obtained from the summation of the torque of the solid wall cells of the impeller. The resulting torque is multiplied by the angular velocity of the impeller to obtain the required power.

Figure 7.3 shows the power based on the calculations and the one obtained from the prediction software. Results are normalised with the required power of the full scale installation at the design speed computed with the prediction software. Over the complete range of calculated conditions, a small over-prediction of the power can be observed. The deviation of about 2.5% is acceptable, however. The deviation is more or less constant for all conditions, due to the very small variation in flow rate. The increase in flow rate is only 4.5% for an increase of ship speed from 31 to 47 knots.
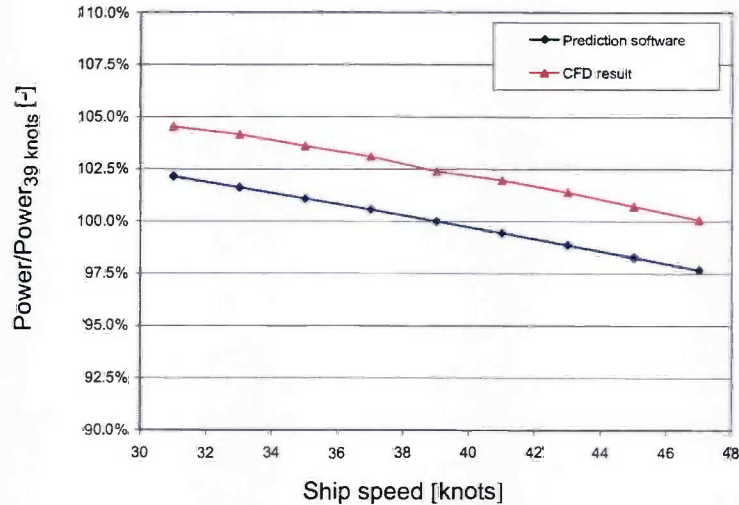
Figure 7.3   *Comparison of required power of waterjet installation obtained from prediction software and the one obtained from CFD calculations*

7.5   Analysis of vertical force on waterjet structure

In the preceding section, the prediction of the waterjet thrust is discussed. While calculating the thrust of the waterjet installation, based on the integration of the forces acting on the solid walls, it is found that there can be a net force in the vertical direction as well. This vertical force component is in fact a lift force acting on the waterjet structure.

This result of the numerical analysis is not in agreement with the results of Van Terwisga [2], who claims that there is no net lift contribution. On the other hand, Svensson [3] determined a lift force from pressure measurements in the intake and on the hull, which can be up to 5% of the displacement of the vessel.

Applying equation (2.35) for the vertical direction yields:

$$L_{wj,all} = - \int_{A_{tube}} p\underline{z} \cdot d\underline{A} + L_{wj,hull} \qquad (7.5)$$

where L_{wj} is a vertical force on either the waterjet or the hull. The vertical components of the momentum fluxes do not contribute, since it is assumed

that both the velocity distributions at the inlet and nozzle exit are aligned with the horizontal direction.

A more detailed analysis of the occurring lift force coefficient, reveals that the largest lift is found at high IVR conditions, and therefore high ship speed. The numerical results presented in this subsection are for a waterjet installation for very high speed vessels. The most important difference from hydrodynamic point of view between a conventional waterjet installation and a high-speed application is found in the geometry of the inlet duct [4].

Inlet lift coefficient

The actual lift force acting on the inlet structure is presented as a non-dimensional coefficient, according to:

$$C_L = \frac{L_{wj,all}}{\rho Q v_{pump}} \tag{7.6}$$

where $L_{wj,all}$ is the calculated vertical force, ρ the density, Q the volume flow and v_{pump} the averaged axial velocity upstream of the impeller. The lift coefficient is plotted as a function of IVR in figure 7.4.

Up to an IVR of about 1.5 the lift coefficient is indeed rather small. For high speed applications (>60 knots) the IVR will be about 2 to 2.2. This will result in a lift coefficient of about 0.08 to 0.10.

Equation (7.6) can be expressed in specific pump parameters Ω, D and φ as well with equation (2.15) as:

$$C_L = \frac{L_{wj,all}}{\rho \Omega^2 D^4} \cdot \frac{\pi}{4\varphi^2} \tag{7.7}$$

The second factor on the right hand side is of order 1 for common waterjet mixed-flow pumps. Thus, a direct comparison between the lift force coefficient on the inlet and the vertical force coefficient on the impeller, as a result of non-uniformity can be made. At an IVR of 2.19, the vertical force is about 2.85×10^{-3}, according to figure 6.22 on page 151. The vertical force coefficient in the inlet for that condition is 0.081, based on figure 7.4. It is concluded that the vertical force in the inlet is significantly larger (almost factor 30) than the vertical component of the impeller force due to non-uniform inflow velocity distributions.
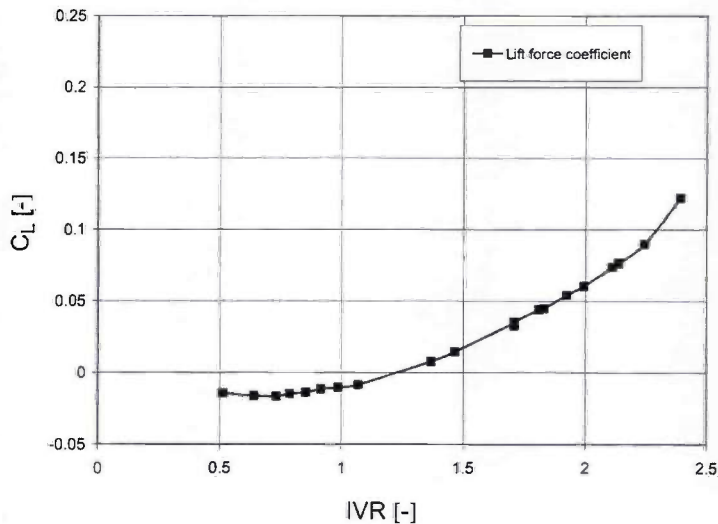
Figure 7.4   Lift coefficient C_L as a function of IVR

Inlet lift-thrust ratio

The lift force can also be compared to the thrust of the waterjet installation. The thrust of a waterjet can be rewritten from equation (2.52), with aid of equations (2.2), (2.11), (2.12) and (2.13) to:

$$T = \rho Q v_{pump}\left\{\left(\frac{D_{inlet}}{D_{nozzle}}\right)^2 - (1-w) \cdot IVR\right\} \tag{7.8}$$

where D_{inlet} and D_{nozzle} are two geometric parameter of the installation and w is the wake fraction, defined in equation (2.2).

The lift-thrust ratio becomes:

$$\frac{L}{T} = \frac{C_L}{\left\{\left(\frac{D_{inlet}}{D_{nozzle}}\right)^2 - (1-w) \cdot IVR\right\}} \tag{7.9}$$

This shows that the lift-thrust ratio is related to the lift coefficient, the wake fraction and the geometry of the waterjet installation. The data for the lift coefficient as shown in figure 7.4 is presented as lift-thrust ratio in figure 7.5.
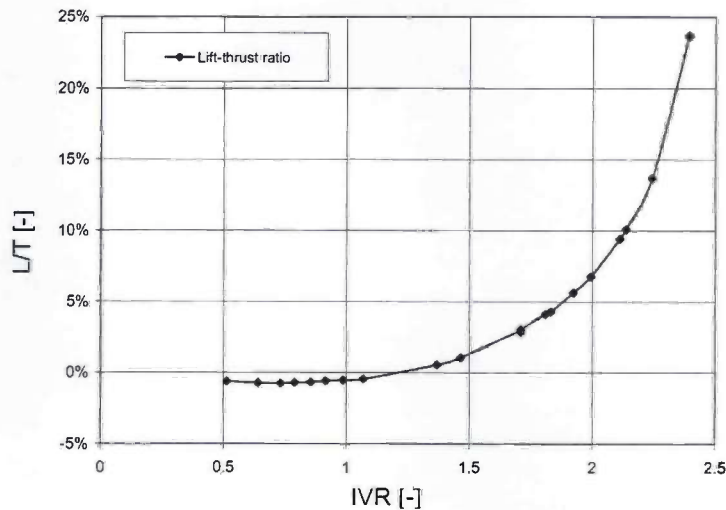
Figure 7.5   Lift-thrust ratio L/T as a function of IVR

Since the thrust decreases with increasing IVR, the lift-thrust ratio shows a steep increase at high values of IVR: a significant lift force of about 10-20% of the thrust is found. This amount of lift can not be neglected in general.

The lift force in the inlet creates a moment on the hull structure at high speeds, which can lead to a reduced or even negative trim angle of the vessel.

7.6   Pressure distribution on streamtube surface

7.6.1   Evaluation of momentum balance in vertical direction

The CFD analyses reveal the presence of a significant lift force in a waterjet installation at the higher IVR conditions. Based on equation (7.5), the lift can be the result of a net force acting on the hull surface or of a resultant force of the pressure distribution, which acts on the streamtube surface.

These two terms are neglected in the standard momentum theory, which is in accordance with the simplified thrust equation (2.52). As a result, the net lift force is equal to zero for all conditions.

The contribution of the vertical forces acting on the hull surface are limited to a region near the cutwater. It is known from CFD analyses that the pressure in this region is very low for high IVR conditions (see for example figure 5.6). It is expected that any possible contribution to the vertical force will be a negative lift for high IVR. It is concluded that the lift force on the complete

waterjet structure, should originate from a pressure distribution along the streamtube surface. A method to integrate the pressure distribution on the streamtube surface is required to confirm this.

Accurate determination of the lift force, acting on the hull structure, is not possible with the applied method. It is not possible to determine the contribution of the solid wall cells near the streamtube interface accurately, because the effect of partially included solid wall cells can not be taken into account.

The shape of the streamtube depends on the IVR at which the waterjet operates. The pressure distribution also depends on IVR. In order to determine the net force, an integration of the pressure over the surface has to be made. For this numerical integration, the surface of the streamtube is subdivided into triangles, based on the Delaunay triangularisation method. The net lift force can be determined, given the average pressure on each triangle and the normal direction.

7.6.2 Calculation of vertical force on streamtube

The streamtube shape is determined for various operating conditions of the high-speed waterjet installation, as discussed in the preceding section. An example of the triangular mesh of the streamtube surface is shown in figure 7.6. The triangular mesh represents the streamtube surface and the rectangular cells represent the solid wall cells of the waterjet inlet.

The resulting lift force of the streamtube pressure distribution is shown in figure 7.7. The force has been made non-dimensional according to equation (7.6).

The force of the integrated pressure distribution clearly depends on IVR. At values of an IVR above 1.8 the net lift force on the streamtube exceeds the total lift force on the inlet. At these IVR conditions, the net force on the hull (near the cutwater) will be negative. This confirms the hypothesis of the contribution of negative lift of the wall cells near the cut water at higher values of IVR. At an IVR of about 1.0 the net force on the cutwater region will be positive, which is in agreement with expectations as well.

Figure 7.6   Example of triangular surface mesh of streamtube surface (in green). Rectangular cells represent solid wall cells of waterjet inlet in blue.
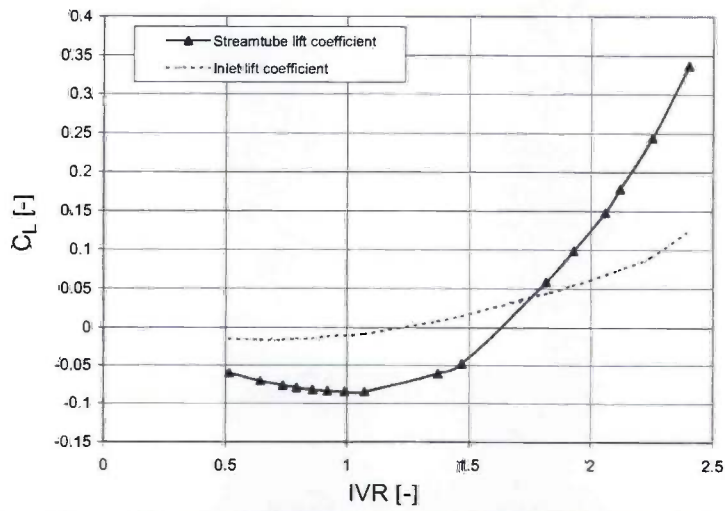

Figure 7.7   Lift force coefficient of streamtube pressure distribution as function of IVR compared to inlet lift coefficient

170

7.6.3 Concluding remark

A first attempt to quantify the forces, which result from the pressure distribution along the streamtube, has shown that there can be a significant force in vertical direction. This force depends on the value of the IVR of the waterjet installation. However, the actual geometry of the inlet geometry might have an important influence on the magnitude of the lift force as well. Further research of this is recommended before general conclusions can be drawn.

7.7 Nomenclature

A	area	m^2
C_f	friction coefficient	-
C_L	lift coefficient	-
D	diameter	m
D	drag force	N
IVR	inlet velocity ratio	-
L	length of flat plate	m
L	lift force	N
p	static pressure	Pa
Q	flow rate	m^3/s
T	thrust	N
v	velocity	m/s
w	wake fraction	-
z	vertical direction	

Greek symbols

μ	dynamic viscosity	kg/ms
ρ	density	kg/m^3
φ	flow coefficient	-
Ω	angular velocity	rad/s

Subscripts

inlet	inlet plane
nozzle	nozzle exit plane
pump	pump entrance plane
wj	waterjet

7.8   References

[1] Schlichting, H., 'Boundary layer theory', McGraw-Hill, New York, 1968

[2] Terwisga, T.J.C. van,'Waterjet hull interaction', PhD thesis, Delft University,1996

[3] Svensson, R., 'Experience with the KaMeWa waterjet propulsion system', AIAA conference, Paper No 89-1440-CP, Arlington, 1989

[4] Bulten, N. & Verbeek, R.,'Design of optimal inlet duct geometry based on operational profile', Proceedings FAST2003 conference Vol I, session A2, pp 35-40, Ischia, Italy, 2003

Chapter 8   Concluding remarks

8.1   Conclusions

The numerical analysis of a waterjet propulsion system has led to an increase of the knowledge of the flow phenomena occurring in the system. The basic theory which is used to describe the flow in the system has been evaluated as well, resulting in a reassessment of the widely applied methods. Results have been obtained for both the flow through the inlet as well the flow through the mixed-flow pump. Typical examples are the investigation of the streamtube shape and the time dependent forces acting on the impeller. With aid of the numerical results, it has been possible to evaluate some general used assumptions in waterjet propulsion theory as well.

8.1.1   Theory of thrust prediction for waterjet systems

The theory of thrust prediction is based on the method of momentum balance with a control volume involving the streamtube. It is shown that this approach is not completely correct. Partly because the streamtube approach does not take into account the complete waterjet geometry and partly due to the neglect of the contribution of the pressure on the streamtube surface.

The method of the momentum balance is derived from the theory for open propellers, for which the usefullness is generally accepted. Direct application of this theory to waterjet propulsion systems is not allowed because of an open propeller is an external flow machine and a waterjet is an internal flow machine. The thrust of an open propeller is almost entirely transferred to the

ship through the shaft. For a waterjet installation, the thrust can for a certain part also be transferred to the ship through the pressure and friction on the solid surface of the inlet and the pump housing.

However, it appears that the effect of the short-comings of the applied theory are in general within a few percent. In practice, this is compensated for by most waterjet manufacturers using the so-called thrust-deduction factor.

8.1.2   *Numerical aspects*

For waterjets with a flush inlet it is unavoidable to get a non-uniform velocity distribution into the pump at the design point. This necessitates the investigation of the effects on non-uniform inflow to the pump. One of the important topics of the thesis was to investigate the origin and the consequences of the non-uniform inflow velocity distribution to the pump of the waterjet installation. It is found that the velocity distribution is a result of accumulating vorticity in the flow. The vorticity is generated in the hull boundary layer and increased in the inlet, where the flow is retarded rapidly. For open propellers similar phenomena play a role in the creation of the so called wake field behind a ship.

Because of the dominance of viscous flow effects only a numerical method based on the Navier-Stokes equations is appropriate. Currently available commercial Reynolds-averaged Navier-Stokes (RANS) methods are well suited for the numerical analyses of both the flow in the waterjet inlet and the waterjet pump flow. It is demonstrated that standard two-equation turbulence models in combination with wall functions give results with acceptable accuracy, whilst keeping the overall calculation times and required hardware within acceptable limits. However, the used two-equation turbulence models do have a general short-coming in the prediction of the pressure at a stagnation point. This is reflected in an over-prediction of drag of profile sections.

8.1.3   *Waterjet inlet flow characteristics*

The calculations of the waterjet inlet flow revealed that most characteristics are strongly related to the inlet velocity ratio (IVR=v_{ship}/v_{pump}). Typical examples are:

- static pressure distribution inside the inlet
- cavitation inception at cutwater
- velocity distribution in the impeller plane
- margin against flow separation in the inlet
- shape of the inlet streamtube
- lift force on the inlet geometry

Due to variations in design ship speed and power density of the installations, the actual design IVR can vary per vessel. For optimum performance of the inlet, which means for example optimal cavitation inception margins and avoidance of flow separation in the inlet, a dedicated inlet design is recommended for each specific ship.

The shape of the streamtube upstream of the inlet can be approximated with a semi-elliptical shape. The development of the flow in streamwise direction can be characterised as a diffuser flow. The equivalent diffuser angle depends on IVR.

The pressure distribution on the solid part of the streamtube surface creates a net vertical force, specifically at high IVR. This lift force can be up to 20% of the thrust of the system.

8.1.4   Waterjet mixed-flow pump analyses

The numerical method is used to analyse the flow through the rotating pump impeller as well. Calculations are based on the quasi-steady multiple frames of reference method and the fully transient moving mesh method. Differences between the two approaches has shown to be small for performance indicators like head, torque and efficiency.

The performance of the pump is not significantly influenced by variation of the inflow velocity distribution. However, the pressure distribution on the rotating impeller blades is strongly related to the inflow velocity distributions. This results in a change of the behaviour of the in-plane forces. Calculations with uniform inflow show a radial force that is almost constant in magnitude, but which rotates about the impeller axis with the blade passing frequency. This is due to rotor-stator interaction. In case of non-uniformity of the inflow, an additional contribution to the mean radial force is found. The magnitude and direction of this additional radial force depend on the amount of non-uniformity and the flow rate through the pump.

8.2   Recommendations

8.2.1   Research topics for marine propulsion systems

The general applied theory for thrust prediction of waterjets has some shortcomings. Similar shortcomings might be present in the theory for the prediction of thrust for ducted propellers and thrusters. In this respect these type of propulsion units can be regarded as mini-waterjet installation as well.

The consequences of the net vertical force occurring in the inlet have to be investigated in more detail. For sufficiently large forces, the behaviour of the vessel may be influenced.

Improvement of the thrust prediction method might give an improved insight in the thrust deduction factor.

8.2.2   Application of RANS methods

With the currently available hardware, i.e. single linux PCs, the calculations presented in this thesis have been made within acceptable wall-clock turn-around times. This will even get better, given the fact that the performance of computers increases continuously. It is thus recommended to start building experience with RANS methods for marine propulsion systems, centrifugal pumps and even complete ship hulls.

Increase of the use of RANS methods in propeller and hull design may have an interesting consequence; the full-scale RANS calculation eliminate the use of Reynolds scaling laws, which are currently in use to scale model scale experimental results to full-scale.

The use of panel methods in the analysis of propellers should be evaluated. Compared to a RANS method the required wall-clock time for an analysis is small, but the obtained accuracy, certainly at off-design conditions, can be rather poor. Investigations should be made to determine which level of accuracy can be obtained with a RANS method.

A similar study can be made for ducted propellers, for which an additional Kutta-condition is required in a panel method at the nozzle trailing edge. Application of a RANS method for such configuration eliminates the requirement of Kutta-conditions.

Appendix A   Stability of non-uniform velocity distribution

In chapter 3 the velocity distribution just upstream of the impeller is discussed. It is shown that the velocity field is strongly non-uniform at normal waterjet operating conditions. This type of velocity distribution has to be reproduced with the numerical method in order to obtain a correct analysis of the complete waterjet installation.

Velocity gradients occur by definition in a non-uniform velocity distribution. If a potential flow method is to be used, then an irrotational velocity field is required. For a velocity field free of vorticity, velocity gradients in one direction are compensated by gradients in the other two directions. A typical example of a non-uniform velocity distribution in a potential flow is the flow through a 90 degree bend, where high velocity is found at the inner corner and low velocity at the outer corner. In the first half of the bend the influence of viscous forces on the flow will be relative small and therefore the flow can indeed be regarded as irrotational. However, in the second part of the bend the differences between irrotational flow and the actual, viscous flow become apparent. In a viscous flow the high momentum fluid will move outwards in the second part of the bend. Then it will take 30 to 50 pipe diameters, before the velocity distribution is uniform again. In a potential flow the high speed velocity region will vanish within a length of about 1 pipe diameter.

Ito [1] measured the pressure drop downstream of a 90 degree bend. It is shown that the pressure drop, in addition to the one that occurs in a straight pipe, after a bend occurs over a length of about 50 pipe diameters. This is in accordance with the length which is required to obtain a fully developed velocity distribution without swirl again. This phenomenon can be attributed to

the development and decay of vorticity in the flow. This vorticity is transported and redistributed in the flow, until it is dissipated into heat. In this type of flow velocity gradients contribute to the vorticity. On the other hand, reduction of the vorticity leads to smaller velocity gradients and thus a more uniform flow.

For an accurate description of the viscous flow through a 90 degree bend vorticity can not be neglected. It is questionable whether the typical non-uniform waterjet velocity distribution can be represented in an irrotational velocity field then. This velocity field is a result of boundary layer ingestion and retardation of the flow, as discussed in section 3.4. The boundary layer velocity profile has large velocity gradients in the direction normal to the wall. These velocity gradients are also present in the flow in a diffuser. It is to be expected that the axial component of the velocity gradient in the waterjet inlet contributes to a higher vorticity. This hypothesis can be verified, analysing the stability of the non-uniform velocity field in a potential flow method and a RANS method.

A.1   Test case with non-uniform pipe flow

For this test the non-uniform axial velocity distribution will be prescribed at the inlet of a circular pipe. In a potential flow method velocity components in radial and tangential direction will be introduced to create the velocity gradients (in these directions), necessary to ensure irrotational flow. These velocity components are constrained by the wall boundary conditions, which will imply constrains on the admissible inlet velocity distribution. In a viscous flow method only velocities in the axial direction will result. As a consequence the flow is rotational.

The length of the pipe was set to 2 pipe diameters. This will not be sufficient to get complete uniform flow in the RANS calculation, but that is not the object of this analysis. Several runs have been made to ensure mesh independent results.

Figure A.1 shows the non-uniformity parameter ζ, as defined in equation (3.1), as function of the non-dimensional pipe length for the potential flow method. Four different IVR conditions in the range from 1.68 to 2.19 have been analysed, the velocity distributions have been shown in figures 5.13a to 5.13d.

For all conditions a very strong decay of the non-uniformity is observed. After a pipe length of about 1 diameter the flow field is almost completely uniform.

The results of the calculations with a RANS method are presented in figure A.2. Here a very small decay of the non-uniformity can be seen. The viscosity causes a slow decay of the initial vorticity, what leads to smaller velocity gradients and thus more uniform flow. In case of a circular pipe geometry, vorticity stretching will not occur. Transformation into heat is thus the only remaining option.

It can be concluded that there are significant differences between both methods. Use of a potential flow method for the analysis of a waterjet installation is therefore not possible.
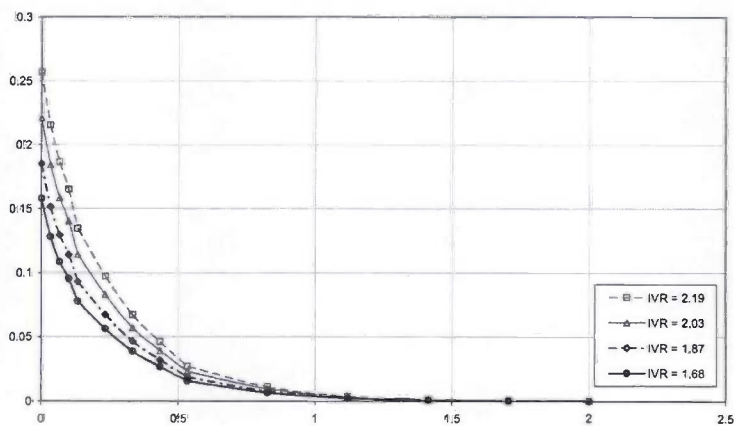

Figure A.1   Development of non-uniformity ζ in potential flow for circular tube
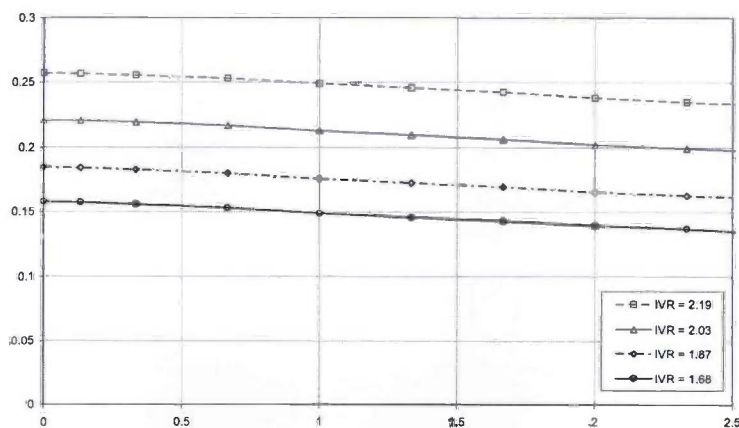

Figure A.2   Development of non-uniformity ζ in flow with vorticity for circular tube

A.2　　　**References**

[1]　Ito, H., 'Pressure losses in smooth pipe bends', ASME Journal Basis Engineering, Vol. 82, p.131, 1960

Appendix B   Fourier analyses of transient flow calculations

Results of the Fourier analyses of the axial velocity and pressure obtained for the transient calculations are presented in this appendix. The solution is monitored at six positions in the domain during the solution process. Three points are located upstream of the impeller and three in between the rotor and the stator. The Fourier analyses of the solution of these last three points can give a good indication whether the solution has become periodic.

The results of the axial velocity at the monitoring points upstream of the pump are governed by the inlet boundary condition. Fourier analyses of these results do not provide additional information. The results of the pressure level upstream of the pump show small fluctuations with a frequency of about 13 times the blade passing frequency. These pressure results are not used for the evaluation of periodicity of the flow field.

The results of the Fourier analyses for design flow rate Q are presented in figures 6.11 and 6.12 as well.

The Fourier analyses for the results of calculations with uniform inflow are presented in figures B.1 to B.6. The frequencies are normalised with the shaft frequency in all diagrams.

The results of the calculations with non-uniform velocity distributions are presented in figures B.7 to B.10 for design flow rate and in figures B.11 to B.14 for 80% of the design flow rate.

Review off all results confirms the periodic behaviour of both the axial velocity and the pressure at the three arbitrarily chosen monitoring points.
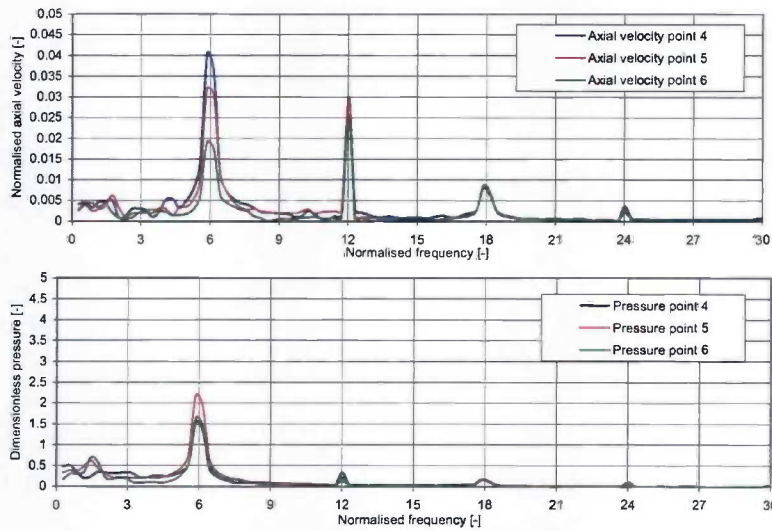
Figure B.1   Fourier transforms of axial velocity and pressure at monitoring points downstream of the impeller with uniform inflow for 60% of design flow rate
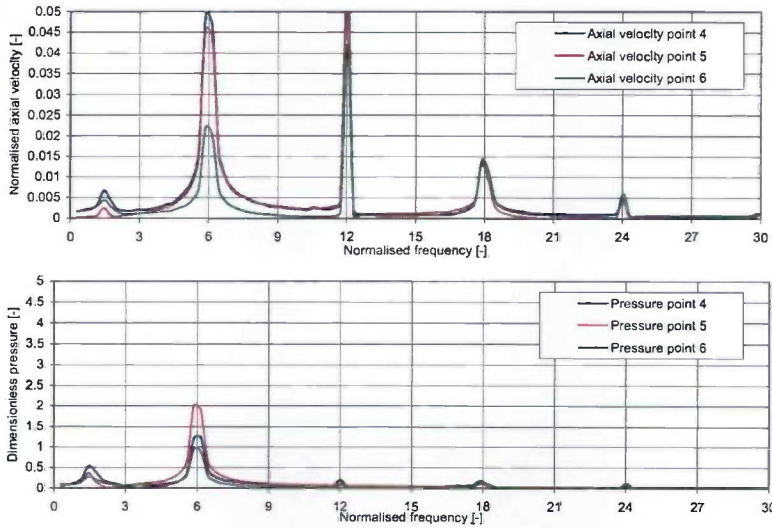

Figure B.2   Fourier transforms of axial velocity and pressure at monitoring points downstream of the impeller with uniform inflow for 70% of design flow rate
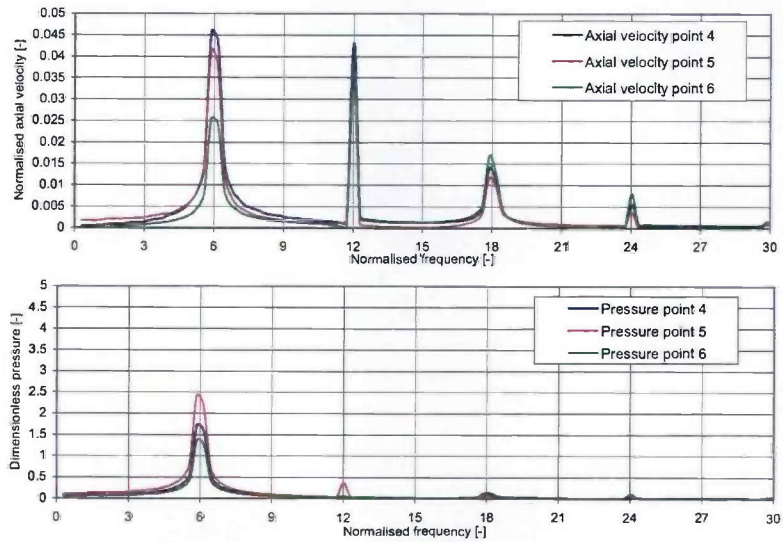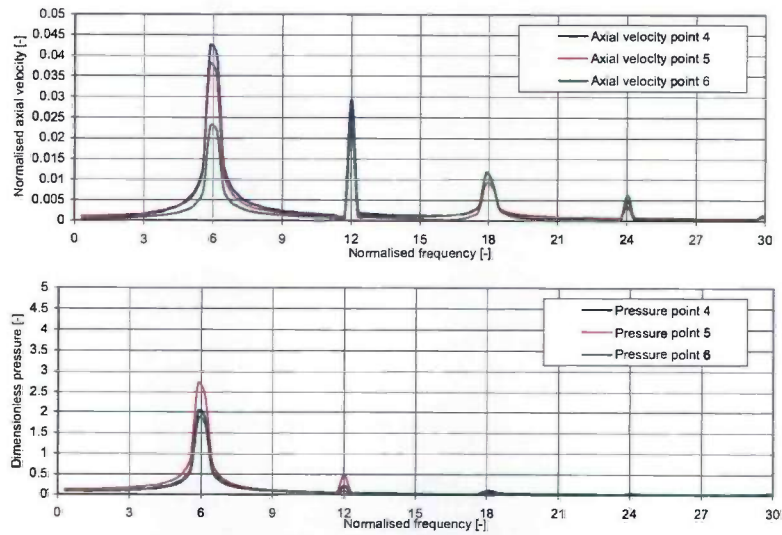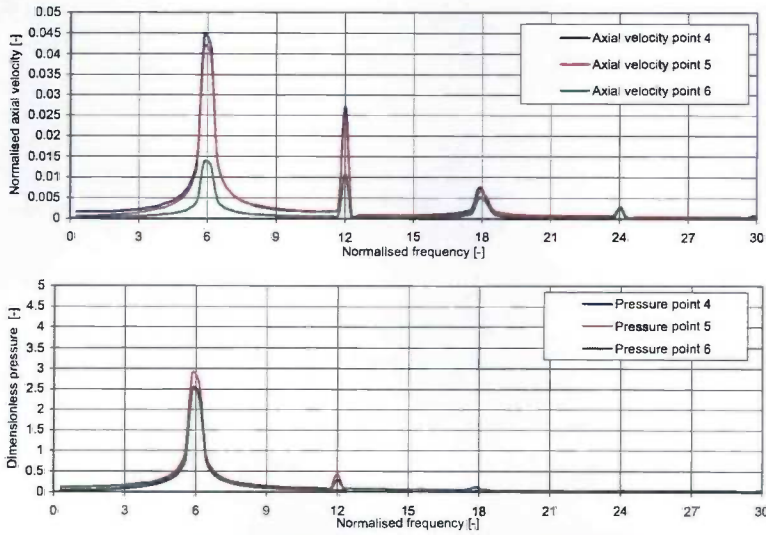
Figure B.3   *Fourier transforms of axial velocity and pressure at monitoring points downstream of the impeller with uniform inflow for 80% of design flow rate*

Figure B.4   *Fourier transforms of axial velocity and pressure at monitoring points downstream of the impeller with uniform inflow for 90% of design flow rate*

Figure B.5   Fourier transforms of axial velocity and pressure at monitoring points downstream of the impeller with uniform inflow for the design flow rate
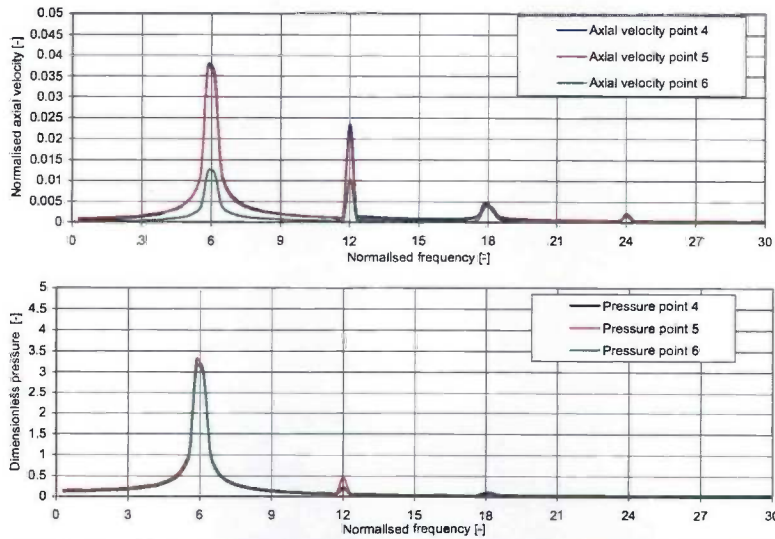

Figure B.6   Fourier transforms of axial velocity and pressure at monitoring points downstream of the impeller with uniform inflow for 110% of design flow rate
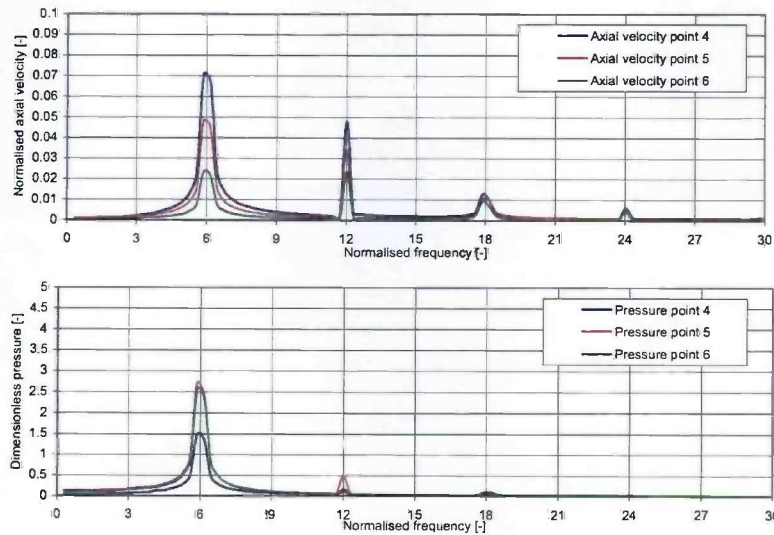
Figure B.7   Fourier transforms of axial velocity and pressure at monitoring
             points downstream of the impeller for IVR=1.68 at design flow
             rate
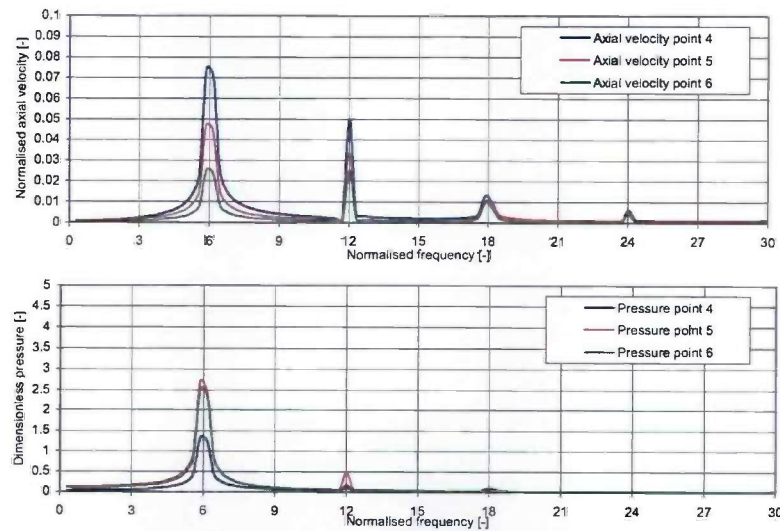

Figure B.8   Fourier transforms of axial velocity and pressure at monitoring
             points downstream of the impeller for IVR=1.87 at design flow
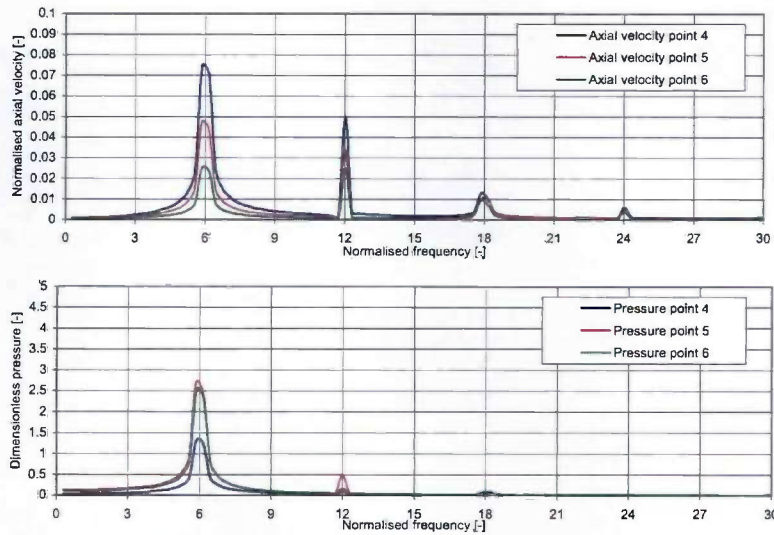   rate

Figure B.9   Fourier transforms of axial velocity and pressure at monitoring points downstream of the impeller for IVR=2.03 at design flow rate
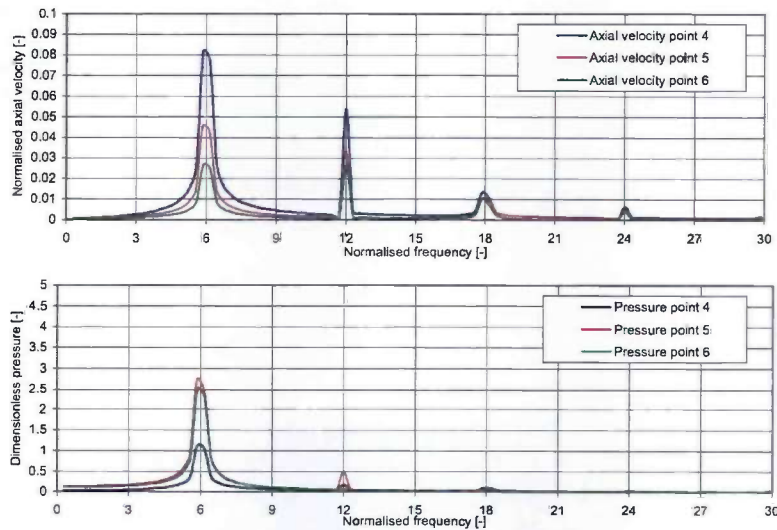

Figure B.10   Fourier transforms of axial velocity and pressure at monitoring points downstream of the impeller for IVR=2.19 at design flow rate

Figure B.11   Fourier transforms of axial velocity and pressure at monitoring points downstream of the impeller for IVR=1.68 at 80% of design flow rate

Figure B.12   Fourier transforms of axial velocity and pressure at monitoring points downstream of the impeller for IVR=1.87 at 80% of design flow rate

Figure B.13   Fourier transforms of axial velocity and pressure at monitoring points downstream of the impeller for IVR=2.03 at 80% of design flow rate
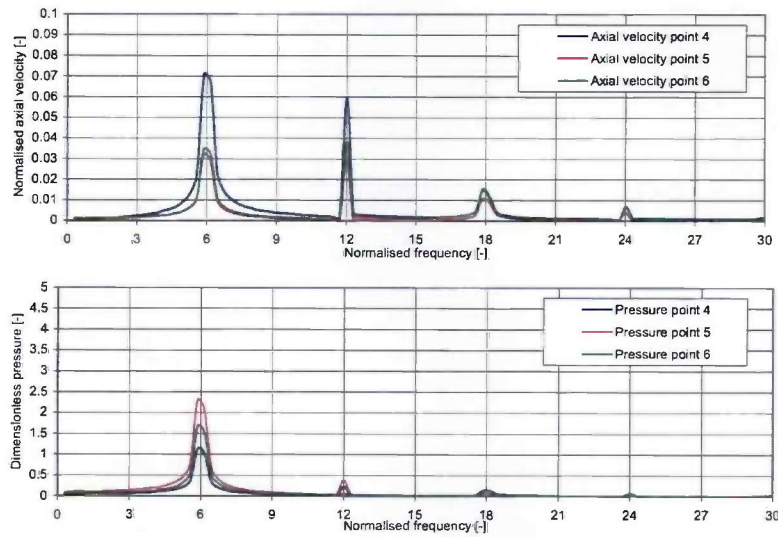

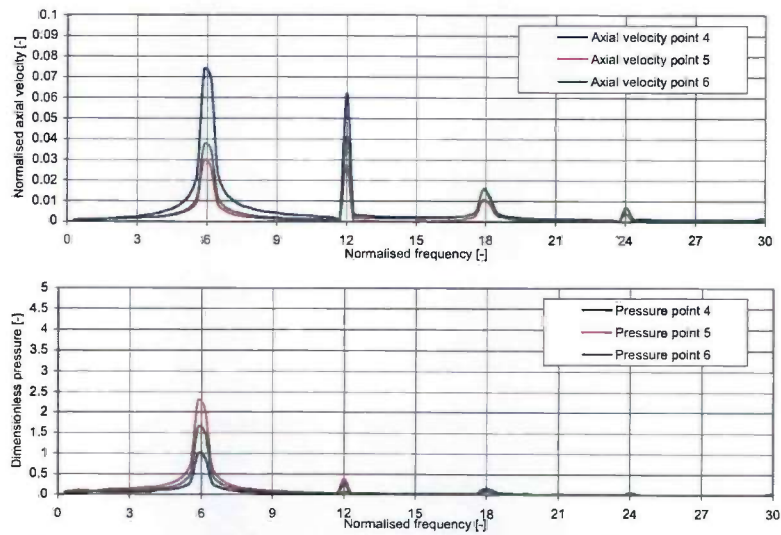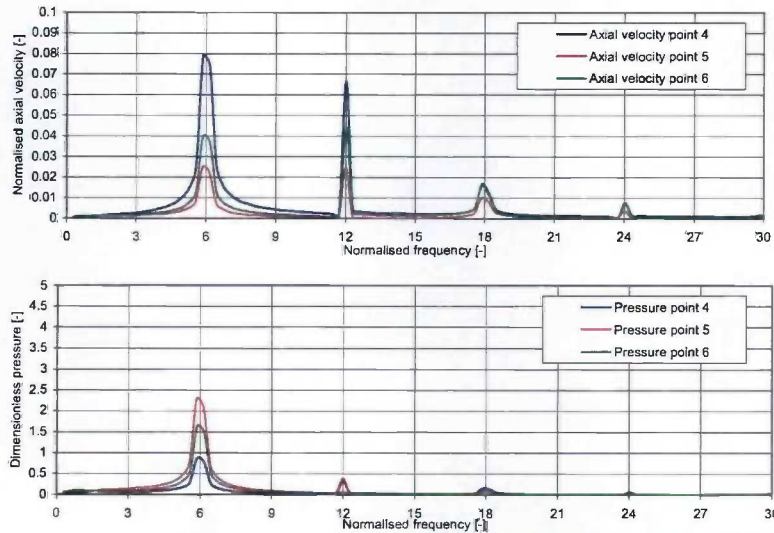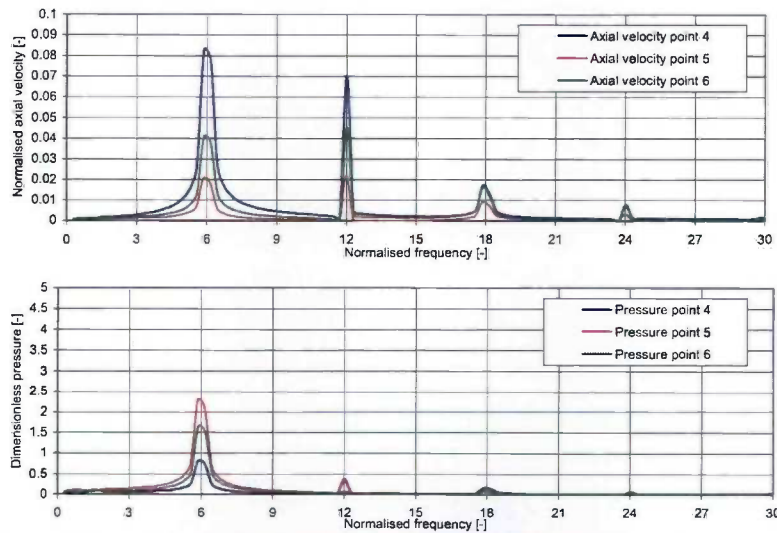*Figure B.14   Fourier transforms of axial velocity and pressure at monitoring points downstream of the impeller for IVR=2.19 at 80% of design flow rate*

Summary

A waterjet propulsion system is used to propel ships, using a pump which produces a high speed jet. A standard waterjet installation can be divided into an inlet, a pump and a nozzle. For manoeuvring and reversing purposes an additional steering device can be integrated into the installation. The development of waterjet propulsion systems has made significant progress over the last few decades. Nowadays, commercial fast-ferries reach velocities of 50 knots, which is about 90 km/h.

The theory to describe waterjet propulsion systems is derived from open propeller theory. The prediction of the thrust of a propeller is based on the momentum balance of a streamtube control volume. This thrust is then transferred though the shaft of the propeller to the hull of the ship. In contrast, for a waterjet propulsion system, forces are transferred to the hull not only through the shaft but also through the solid surface of the installation. A critical review learns that some assumptions made for open propellers are not valid for waterjets.

The inflow to the waterjet pump is non-uniform. This results in a blade loading that varies during an impeller revolution. The cause and the effects of this non-uniform inflow have been investigated. Four contributing factors are identified for the development of a non-uniform velocity distribution just upstream of the pump. As a first cause, the water is ingested from below the the hull of the ship, where a boundary layer with a non-uniform velocity distribution is present. Even at normal operating conditions, the water is subsequently retarded in the inlet, which results in an increase of the non-uniformity. Finally, the inflow passes the bend in the inlet and the protruding

shaft which add to the increase in non-uniformity. It is concluded that the non-uniformity is the result of the accumulated vorticity in the flow. Due to this vorticity, a stable velocity distribution is found, and the typical velocity distribution is more or less independent of the actual design of the inlet.

The investigations are based on numerical analyses of the flow through the complete waterjet installation. Selection of the numerical method is based on the capability to capture typical flow phenomena in a waterjet installation: high Reynolds number, time-dependency, and incompressible flow in a partially rotating frame of reference. Due to the high level of non-uniformity of the inflow, the ability to generate and transport vorticity in the flow is an important requirement, as well as the possibility to take into account the flow phenomena in the tip clearance region between the rotating blades and the stationary housing.

A Reynolds averaged Navier-Stokes (RANS) method is chosen to perform all numerical analyses. The Reynolds-stresses are obtained using the two-equation k-ε turbulence model. This turbulence model is known to produce an error near a stagnation point. An estimation of the influence of this error on the prediction of thrust and torque shows that the actual deviations are acceptable.

The numerical models of both the waterjet inlet and the mixed-flow pump are validated with available experimental data. Results of calculations of the waterjet inlet flow are compared with measurements of static pressure along the inlet and with the total pressure and velocity distribution at the impeller plane. Agreement between the CFD results and the experimental data is good for all calculated conditions. The flow phenomena in a waterjet inlet are characterised by the inlet velocity ratio (IVR), which is the ratio of the ship speed and the pump speed.

The shape and location of the streamtube of the ingested water is determined with aid of a concentration scalar. This enables the visualisation of the streamtube and the calculation of the mass averaged inflow velocity. In this way the wake fraction of the waterjet installation is determined accurately. It is shown that the actual shape of the streamtube depends on IVR.

The CFD calculations of the mixed-flow pump are validated with experimental data for the pump head and the shaft power. The calculations are performed with a quasi-steady multiple frame of reference (MFR) method and a fully transient moving mesh method. Differences between predicted head and power in both methods are small.

The fully transient moving mesh calculations with a uniform inflow velocity distribution provide the unsteady excitation forces on the impeller due to rotor-stator interaction. It is found that the magnitude of the radial interaction force depends on the flow rate though the pump.

The influence of the non-uniform velocity distribution to the pump is investigated as well. The deviation in pump performance is limited to a few

percent for the calculated conditions. The influence on radial forces is far greater, however. An additional mean component of the radial force is found, the magnitude and direction of which are related to the flow rate and the level of non-uniformity. The origin of this mean force is an unbalanced torque on the impeller blades, due to a variation of the angle of attack during a revolution.

Both validated numerical models of the inlet and the pump are combined to form the complete waterjet installation. Results of the calculations of the complete unit are compared with the results of the standard waterjet performance prediction and selection software of Wärtsilä Propulsion Netherlands BV. Good agreement is found for the prediction of flow rate, thrust and torque of the installation. Two methods to determine the thrust are used: (i) the integration of the axial force component on the solid wall and (ii) the application of a simplified version of the integral momentum balance equation. The latter method is generally applied by ship building companies. A clear deviation between the two methods is found for higher ship speeds.

Analysis of the net force in vertical direction reveals a significant lift force at high speeds. It is concluded that the method based on the momentum balance for the streamtube control volume, has some short-comings. The deviation increases for higher ship speeds.

The numerical results confirm the hypothesis that the simplified method to describe waterjet installations is not correct. This can be partly attributed to the neglect of the influence of the hull in the vicinity of the waterjet inlet and partly to the neglect of the contributions of the pressure distribution acting on the streamtube.

Samenvatting

Een waterjet voortstuwingssysteem wordt gebruikt om schepen voort te stuwen met behulp van een pomp, die een waterstraal met hoge snelheid produceert. Een standaard waterjet voortstuwingssysteem is opgebouwd uit een inlaat, een pomp en een nozzle. Een stuurdeel kan geïntegreerd worden in de installatie om manouvreren mogelijk te maken. De ontwikkeling van waterjet voortstuwingssystemen heeft de laatste decennia een enorme ontwikkeling doorgemaakt. Tegenwoordig worden met commerciële fast-ferries snelheden van rond de 50 knopen bereikt. Dat komt overeen met ongeveer 90 km/uur.

De theorie om het voortstuwingssysteem te beschrijven is afgeleid van de theorie voor open schroeven. De voorspelling van de stuwkracht van een schroef is gebaseerd op de impulsbalans van een stroombuis controle volume. Deze stuwkracht wordt door de as van de schroef op het schip overgebracht. Echter, de krachten die werken op een waterjet voortstuwingssysteem worden behalve via de as ook via de vaste wanden van de installatie naar het schip overgebracht. Een kritische analyse laat zien dat sommige aannames die gemaakt zijn voor open schroeven niet geldig zijn voor waterjets.

De instroming naar de waterjet is niet-uniform. Dit heeft tot gevolg dat de belasting van de waaierbladen varieert gedurende een omwenteling. De oorzaak en de gevolgen van deze niet-uniforme instroming zijn onderzocht. Er zijn vier factoren geïdentificeerd die bijdragen aan de ontwikkeling van de niet-uniformiteit van de instroming vlak voor de pomp. Allereerst wordt het water afgezogen uit het gebied onder het schip. Daar bevindt zich een

grenslaag met een niet-uniforme snelheidsverdeling. Vervolgens ondergaat deze instroming een vertraging in de inlaat van het systeem, wat resulteert in een toename van de niet-uniformiteit. Als laatste passeert de instroming een bocht in de inlaat en de as van de pomp, waardoor de niet-uniformiteit verder wordt vergroot. Er kan worden geconcludeerd dat de niet-uniformiteit het resultaat is van een accumulatie van vorticiteit in de instroming. Door deze vorticiteit wordt een stabiele snelheidsverdeling gevormd en daardoor is de typische snelheidsverdeling nagenoeg onafhankelijk van de vorm van de inlaat.

Het onderzoek is gebaseerd op een numerieke analyse van de stroming door de complete waterjet installatie. De eisen die worden gesteld aan de numerieke methode worden bepaald door de aard van de stroming door een waterjet installatie. Deze kan worden gekarakteriseerd als een tijdsafhankelijke, niet-samendrukbare stroming met een hoog Reynolds getal, in een systeem dat gedeeltelijk roteert. Vanwege de hoge mate van niet-uniformiteit zijn verder de productie en het transport van vorticiteit belangrijke aspecten, evenals de mogelijkheid om de stroming in de nauwe spleet tussen de roterende waaier en het stationaire pomphuis goed te kunnen modelleren.

Een Reynolds-gemiddelde Navier-Stokes (RANS) methode is gekozen voor alle numerieke analyses. De Reynolds-spanningen worden bepaald aan de hand van het k-ε turbulentie model. Het is bekend dat dit model een fout introduceert nabij een stagnatie punt. Uit een schatting van de invloed van deze fout op de voorspelling van stuwkracht en koppel blijkt dat de afwijkingen acceptabel zijn.

De numerieke modellen van zowel de waterjet inlaat als ook de mixed-flow pomp zijn gevalideerd met beschikbare experimentele data. Resultaten van berekeningen van de stroming door de waterjet inlaat zijn vergeleken met metingen van de statische druk langs de inlaat en met de totale druk en de snelheid in het waaiervlak. De overeenkomst tussen de CFD resultaten en de experimentele data is goed voor alle berekende condities. De stromingsfenomenen in een waterjet inlaat worden bepaald door de *inlet velocity ratio* (IVR), wat de verhouding geeft tussen de scheepssnelheid en de gemiddelde axiale snelheid vlak voor de pomp.

De vorm en de ligging van de stroombuis waardoor het water naar de inlaat van de waterjet stroomt, is bepaald met behulp van een concentratie-scalar. Dit geeft de mogelijkheid om de stroombuis te visualiseren en om de massa-gemiddelde instroomsnelheid te bepalen. Op deze manier kan het volgstroom getal (of wake-fractie) van de waterjet installatie nauwkeurig worden bepaald. Het is aangetoond dat de vorm van de stroombuis afhangt van de waarde van IVR.

De CFD berekeningen van de mixed-flow pomp zijn gevalideerd met experimenteel bepaalde waarden van opvoerhoogte en asvermogen. De berekeningen zijn uitgevoerd met een quasi-stationaire *multiple frame of reference (MFR)* methode en met een volledig tijds-afhankelijke roterende

mesh methode. Voor wat betreft de berekende waarden van opvoerhoogte en vermogen zijn de verschillen tussen beide methodes klein.

De volledig tijdsafhankelijke roterende mesh berekeningen met uniforme instroming geven de instationaire excitatiekrachten op de waaier als gevolg van rotor-stator interactie. De grootte van de radiale interactiekracht blijkt afhankelijk van het debiet door de pomp.

De invloed van de niet-uniforme snelheidverdeling vlak voor de pomp is ook onderzocht. De afwijking in de pompprestaties is beperkt tot een paar procenten voor de berekende condities. De invloed op de radiale krachten is echter veel groter. Een additionele tijdsgemiddelde component van de radiale kracht is aanwezig met een grootte en richting die afhangt van het debiet en de mate van niet-uniformiteit. De oorzaak van deze tijdsgemiddelde kracht is een onbalans in het koppel van de verschillende waaier bladen, als gevolg van de variatie in de aanstroomhoek van het blad tijdens een omwenteling.

De twee gevalideerde numerieke modellen van de inlaat en de pomp zijn gecombineerd om een complete waterjet installatie te vormen. Resultaten van de berekeningen van de complete unit zijn vergeleken met het standaard waterjet performance predictie programma van Wärtsilä Propulsion Netherlands BV. Goede overeenkomsten zijn gevonden voor de voorspelling van het debiet door de pomp, de stuwkracht en het koppel van de installatie. Twee methoden voor de bepaling van de stuwkracht zijn gebruikt: (i) integratie van de axiale component van de kracht op alle vaste wanden en (ii) de toepassing van een vereenvoudigde versie van de integrale impuls balans. De laatste methode wordt algemeen toegepast door producenten van schepen. Voor hoge scheepssnelheden is een duidelijke afwijking gevonden tussen de twee methoden.

Analyse van de netto kracht in verticale richting laat zien dat er een significante liftkracht aanwezig is bij hoge scheepssnelheden. Hieruit volgt de conclusie dat de vereenvoudigde methode, gebaseerd op de impuls balans voor het stroombuis controle volume, tekortkomingen heeft. De afwijking wordt groter naarmate de scheepssnelheid toeneemt.

De numerieke resultaten bevestigen de hypothese dat de vereenvoudigde methode voor de beschrijving van de waterjet installatie niet correct is. Dit kan deels worden toegeschreven aan de verwaarlozing van de invloed van de scheepswand in de buurt van de waterjet inlaat en deels aan de verwaarlozing van de bijdragen van de drukverdeling die werken op de stroombuis.

Samenvatting

Dankwoord

Tijdens mijn afstuderen kreeg ik van prof. Bert Brouwers het advies om 'eerst maar eens aan het werk te gaan en dan later een keer een promotie onderzoek te komen doen'. Dit advies heb ik opgevolgd en dit proefschrift is nu het resultaat van de combinatie van 9 jaar werken bij Wärtsilä Propulsion Netherlands BV en het promotie onderzoek aan de Technische Universiteit Eindhoven.

Naast prof. Bert Brouwers wil ik ook mijn tweede promotor prof. Harry Hoeijmakers en mijn directe begeleider, dr. Bart van Esch, bedanken voor hun bijdragen. Ik ben me ervan bewust dat het begeleiden van een externe promovendus niet altijd even gemakkelijk was, iets waar vooral Bart mee te maken had.

De combinatie van het onderzoek met mijn werkzaamheden bij Wärtsilä Propulsion Netherlands BV was niet mogelijk geweest zonder alle studiedagen. Zelfs in tijden van drukte was het mogelijk om tijd aan het onderzoek te be-steden. Hiervoor wil ik Bram Kruyt, Hanno Schoonman en Do Ligtelijn bedanken.

Het interessante van de combinatie van werken en promoveren is waarschijnlijk de directe feed-back van de varende waterjet installaties. Bij het zoeken naar verbeteringen van de waterjet installaties heb ik vele gesprekken en discussies gehad met Rob Verbeek, die waarschijnlijk de meest waardevolle bijdragen aan dit proefschrift hebben opgeleverd. In ieder geval hebben we de term 'voortschrijdend inzicht' bij het management geïntroduceerd.

Norbert Bulten,
Rosmalen, september 2006.

Dankwoord

Curriculum Vitae

29 april 1973 Born in Winterswijk, the Netherlands.

1985-1991 VWO at RSG Hamaland, Winterswijk

1991-1996 Study Mechanical Engineering at the University of Twente, The Netherlands

Specialisation: fluid dynamics and thermal engineering

Graduation thesis on numerical analysis of a centrifugal pump impeller with two different RANS methods

1996 Traineeship at Sulzer Innotec in Winterthur, Switzerland

1997 Researcher at University of Twente, The Netherlands. Project for IHC Parts & Services to optimise dredger pumps

1997- Wärtsilä Propulsion Netherlands (formerly Lips propellers) in Drunen.

1997 - 2002	Research engineer waterjets
2002 - 2006	CFD specialist at Propulsor Technology department.
from 2006	Team leader CFD at Propulsor Technology department

2001-2006 PhD study at Technische Universiteit Eindhoven, The Netherlands

---